PAGE(S) MISSING

pgs. 98-110/132-142

Computational Modeling of Expanding Plasma Plumes

in Vacuum and in a Tank

by

Bernard K. Asare

Submitted to the Department of Aeronautics and Astro-
nautics in partial fulfillment of the requirements for the
degree of

Master of Science

at the

MASSACHUSETTS INSTITUTE OF TECHNOLOGY

September 1999

Author .... ,
Department of Aeronautics and Astronautics
15th September, 1999

Certified by ....
Professor Manuel Martinez-Sanchez
Department of Aeronautics and Astronautics
Thesis Supervisor

Accepted by ....
Nesbitt Hagood
Chairman, Departmental Committee on Graduate Studies
Department of Aeronautics and Astronautics
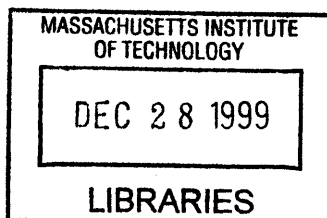
Computational Modeling of Expanding Plasma Plumes in Vacuum and in a Tank

by

Bernard K. Asare

Submitted to the Department of Aeronautical and Astronautical
Engineering on September 15th, 1999, in partial fulfillment of the
requirements for the degree of Master of Science in Engineering

Abstract

Electric propulsion devices have shown to offer substantial fuel savings for various space missions. Hall thrusters, specifically, have shown great promise over the years due to their near optimum specific impulse for a number of space missions. The Hall thruster, however, releases a partially ionized plasma plume which contaminates any surface it comes into contact with. Backflow contamination can lead to sputtering and effluent deposition on critical spacecraft components. A computational method for studying these interactions was developed by David Oh in 1997. He developed a Particle-in-Cell and Direct Simulation Monte Carlo (PIC-DSMC) algorithm to model the expansion of a plasma plume from a Hall thruster into a vacuum. In his work he implemented a plasma-surface interaction model which determined erosion rates on surfaces made of quartz, silicon and silver but he did not track the surface material removed.

In this work Oh's model is expanded to include the removal and tracking of material from generic spacecraft surfaces and the walls of a vacuum tank. Sputtering yields adopted in this model are based on sputtering theory developed by Matsunami and Yamamura. Since the plasma can have a negative impact on spacecraft subcomponents, a method for protecting the spacecraft (in the form of a protective shield) is proposed, studied, and recommendations are discussed.

Thesis Supervisor: Manuel Martinez-Sanchez
Title: Professor

Acknowledgments

Thank you, Prof. M. Martinez-Sanchez, for your continuous support and inspiration throughout my graduate career at MIT. I will forever be indebted to you for what you call your 'preaching' sessions. Your words will always serve as a beacon in life ahead.

I would also like to express my gratitude to Omprakash Gnawali, an undergraduate student in the Electrical Engineering and Computer Science department at MIT, who I have worked with on the extension of the simulation and implementation of my ideas. We spent many hours together during which he and I refined the technical details of sputtering parameters and carried out endless tests and observations. Om_p, thank you.

Life at MIT would not have been complete and so much fun were it not for the good friends I made while pursuing my dream of becoming an aerospace engineer. I thank all, for your support at all times and I am looking forward to the day that our paths cross again.

Finally, I would like to extend my deepest gratitude to SharonLeah Brown and Margaret "Peggy" Edwards for their, advice, encouragement, and support throughout my career at MIT. Your kind hearts and your smiles will always make my day bright and happy.

Kathleen, thank you for your love, kindness and the great times we have. I love you dearly.

Contents

List of Figures

Chapter 1

Introduction

1.1 Background

For satellite or deep-space missions utilizing chemical propulsion, a large percentage of the spacecraft wet mass is propellant. Due to vehicle mass and cost design constraints, this excessive amount of propellant decreases the mass available for payload. In some cases, this decrease in payload mass is so extreme that the mission is no longer feasible within the design space.

Studies have shown that for many missions, an engine which would be used as the primary source of propulsion for orbit transfer missions or for satellite station-keeping should produce exhaust velocities between 10-20 km/s. Cryogenic chemical rocket systems are capable of producing exhaust velocities approaching 5 km/s and storable chemical systems that are currently in use for spacecraft propulsion have significantly lower performance still. It is apparent that a propulsion system is required that does not rely on energy addition through chemical reactions.

Electric Propulsion (EP) thrusters are such a design enabling technology, producing exhaust velocities on the order of 10-20 km/s. This significantly decreases propellant mass and typically enables a higher payload mass. The drawbacks of EP are small values of thrust and a large power supply mass. In some cases, the mass of the power supply offsets the gains of choosing EP over chemical systems. However, recent advances in both EP and power supply technology are making these systems viable options for energetic deep-space missions (e.g. Deep Space 1), attitude control, and near-Earth orbit raising missions just to name a few.

1.2 Motivation

With renewed interest in electric propulsion for a number of planned missions, as well as station keeping applications for geostationary communications satellites, the important issues of spacecraft contamination are receiving increased attention. For example, in Hall thruster (HT) plumes, an energetic plasma is created by charge-exchange processes, and can expand around a spacecraft leading to a current drain on high voltage surfaces. The enhanced plasma density can also lead to attenuation and refraction of electromagnetic wave transmission and reception. In addition, many thrusters emit heavy metal species, both charged and uncharged, due to erosion which can easily adhere to spacecraft surfaces. It is vitally important to understand and predict the backflow transport of these species from the plume onto a spacecraft. Thus, a clear understanding of the plumes of EP thrusters and the transport of contaminating effluents in them is necessary. Backflow contamination can lead to sputtering and effluent deposition that can affect such aspects of the spacecraft as solar arrays, thermal control surfaces, optical sensors, communications, science instrumentation, general structural properties of materials, and spacecraft charging.

Of particular concern are the charge exchange (CEX) ions created when electrons are transferred from slow moving neutrals to fast moving ions during a collision. Slower moving ions and fast moving neutrals are created in the process. It is these CEX ions - energies of 0eV to 400eV - which interact with the surfaces of the spacecraft. This has resulted in an increase in the number of laboratory studies and modeling efforts which have successfully identified the dominant mechanisms for plume-spacecraft interactions, and have adequately quantified a number of them. Among the effects now known with adequate precision, or for which data can be confidently obtained in ground-based facilities include the:

- angular dependence and energy spectrum of the main plume
- distortion of microwave beams crossing the plume
- general features of the production of low-energy ions by CEX collisions in the near plume
- thermal radiation from plumes
- effects of imperfect vacuum on thrust and specific impulse and thus thruster per-

formance

Even though many of the above measurements have been performed, uncertainties still persist in a few areas, where the effects of test facilities are difficult to eliminate completely. These uncertainties include:

- re-deposition of sputtered material from tank walls, and its masking effect on the plume erosion or deposition of thruster-originated material

- possible effects of the 're-circulating' background plasma commonly found in vacuum tanks during thruster operation, which tends to be confused with CEX plasma

- potential effects of ingestion of residual neutral tank gas through the thruster exhaust. (even though the effect on thrust may be measurable, questions remain about effects on thruster wall erosion and plume structure by ions formed from the ingested gas)

- long-distance evolution of the plasma plume, under the influence of the ambient geomagnetic field

- refined and extended modeling of ion-wall interactions, covering most of the materials of interest to spacecraft

- alleviation measures, such as the use of plume shields

This work addressed the possible 're-circulation' of plasma as well as the re-deposition of tank wall material during thruster operation and the effects of a plume shield, as these are deemed to be the effects most seriously affecting projections on spacecraft and environmental quality.

Since it is believed that CEX ions are primarily responsible for damaging spacecraft subsystems exposed to the plasma, simulations involving a protective shield which surrounds the exit of the thruster were performed. The purpose of these tests was to verify if shields do protect spacecraft subcomponents from the damaging CEX ions, and whether redeposition of sputtered shield material may itself become an issue.

1.3 Issues with Vacuum Tank Experiments

Collimators have been used to prevent sputtering contamination of surfaces from test chamber walls. They are to some extent effective, but they also introduce measurement uncertainties by restricting the access of engine debris which would otherwise deposit from some angles and also by generating their own sputtering fluxes.

Knowledge of the structure, potential and composition of the plasma induced by the thrusters at angles far from the plume axis is important for assessment of current closure, optical contamination of sensitive science sensors, and possibly sputtering by low-energy plasma. Because of the possible return of some fraction of the beam ions, together with secondary, wall-generated ions, from the beam stopping surface, this information is difficult to obtain from tank experiments.

Techniques such as mass and emission spectroscopy and laser-induced fluorescence are used to obtain species-specific information. This information includes particle velocities, flux, temperature, density and angular distribution. These experiments are not only complicated to perform but are also expensive to set up. It is, however, important to understand the interactions of electric propulsion subsystems with the rest of the space craft.

1.4 Outline of Research

The broad goal of this work is to gain insight into the contamination process, and to accurately provide estimates of contaminating fluxes so that spacecraft designers can integrate EP devices on spacecraft with a much higher level of confidence. Since it is believed that CEX ions from EP devices are primarily responsible for damaging spacecraft subsystems exposed to the plasma, and Oh's algorithm did not include a detailed study of plasma-surface interactions, the goals of this work are as follows:

- To improve modeling and computation of sputtering yields material commonly used in spacecraft design
- To upgrade Oh's model to include tracking of material sputtered off of surfaces
- To compute plasma properties inside a tank, far from the thrust axis.
- To study the trade-offs involved in using plume shields to protect spacecraft subcomponents from the damaging effects of the plume.

In the following chapters, the background and history of Hall thruster as well as the theory underlying the sputtering process is explained. This is followed by a description of the algorithms, computer code and the assumptions made in the plume model employed for the simulations. The results of vacuum tank simulations are discussed and compared to experimental data. Next, the preliminary results for a generic spacecraft employing a protective shield mounted around the thruster exit are presented. The purpose of these tests is to verify if shields do protect spacecraft subcomponents from the damaging CEX ions, and verify if redeposition of sputtered shield material may itself become an issue. Finally the conclusions of this work are presented and recommendations for future work are suggested.

Chapter 2

Closed-Drift Thrusters

2.1 Hall Thruster History

Hall Effect Thrusters (HET) have an extensive flight history on-board Russian space-craft for stationkeeping, attitude control, orbit injection and repositioning applications. They have been used on at least 23 spacecraft since 1971. The SPT-100 (Stationary Plasma Thruster - 100) has flown on at least three Russian satellites and has completed qualification for Western commercial satellite applications. The SPT-100 HET was scheduled to provide NSSK on a French satellite in 1999 and is planned for use on future Space Systems/Loral satellites whereas the D-55 Thruster with Anode Layer (TAL) HET flew on an experimental BMDO mission in 1997.

SPTs have generated a lot of interest in recent years because of their high efficiency, ideal Isp values, reasonable thrust levels, and their excellent flight experience over the last 25 years. International Space Technology, Inc. (ISTI) is the joint venture formed by Space Systems/Loral, Fakel Enterprises (Russia), the Research Institute of Applied Mechanics and Electrodynamics of the Moscow Aviation Institute (MAI/Russia), and its other international partners to commercialize SPTs for use on Western spacecraft. The U.S. Ballistic Missile Defense Organization has aggressively pursued the development of SPTs for Brilliant Eyes-class missions through its multi-phased Russian Hall Effect Thruster Technology (RHETT) program.

With the increasing emphasis on lowering the mass of spacecraft propulsion systems, increasing spacecraft orbiting lifetimes, and reducing overall costs, together with greater

11

amounts of electric power now available on-board spacecraft, the applications for electric propulsion systems will certainly continue to grow.

Thus after a long period of laboratory maturation, both in the former Soviet Union and in the West, HET technology has matured to a point where its expanded use for select space missions is justified from both a technological and an economic standpoint. One remaining area, however, where some reluctance to its adoption needs to be overcome is the possibility of damaging interactions of the energetic plumes of these thrusters with solar arrays, optical sensors and other space craft surfaces / subsystems.

2.2 Plasmas

Plasma science is the study of the ionized states of matter. Plasmas occur quite naturally whenever ordinary matter is heated to a temperature greater than about $10,000^{\circ}$ C. The resulting plasmas are electrically charged gases or fluids. They are profoundly influenced by the long-range Coulomb interactions of the ions and electrons and by the presence of magnetic fields, either applied externally or generated by current flows within the plasma. The dynamics of such systems are complex, and understanding them requires new concepts and techniques.

Plasma science impacts daily life in many significant ways. Low-temperature plasmas, in which electric fields in the plasma can impart significant energy to the electrons and ions but the plasmas are still cool enough to support a multitude of chemical reactions, are critical to the processing of many modern materials. This method of "plasma processing" is an enabling technology in the fabrication of semiconductors. Important applications include the plasma etching of semiconductors and the surface modification and growth of new materials. Other important uses of low-temperature plasmas include the "cold" pasteurization of foods, the sterilization of medical products, environmental cleanup, gas discharges for lighting and lasers, isotope separation, switching and welding technology, and plasma-based space propulsion systems. As illustrated in the Figure 2.1below, plasmas occur in many contexts, spanning an incredible range of plasma densities and temperatures.

12
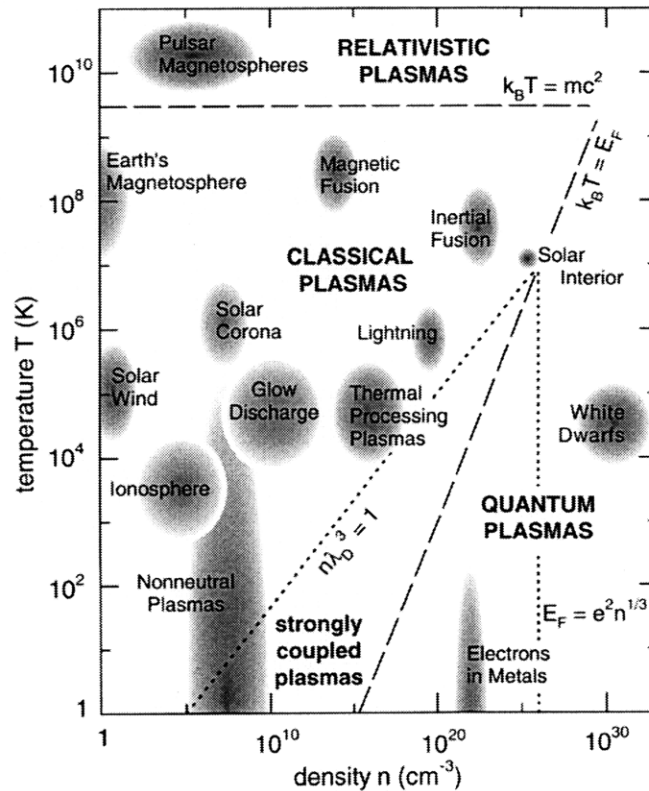
Figure 2.1 **Plasmas that occur naturally or can be created in the laboratory are shown as a function of density (in particles per cubic centimeter) and temperature (in kelvin).**

2.3 Hall Thruster Research at MIT

Extensive work, pertaining to Hall Thruster modeling, has been done at MIT to date. Lentz, in 1993, developed a quasi-one-dimensional model which predicted plasma quantities and thruster performance along the acceleration channel. It was shown that this model matched experimental data quite well by comparing it to research results from a Japanese Hall Thruster.

While Lentz concentrated on developing the one-dimensional model, Oh was developing a two dimensional and three-dimensional model which studied expanding plasma plumes in space. His work implemented a combined Particle-in-Cell (PIC) and Direct Simulation Monte Carlo (DSMC) method to create a quasi-neutral PIC-DSMC model

which not only described the expansion of the partially ionized plasma but also included a crude model of its interaction with (satellite) surfaces.

In 1998, Qarnain expanded on Oh's work by modifying the surface interaction model and looked at the issues associated with developing and end-to-end model of the Hall Thruster. The current work further modifies Oh's work to include the effect of material sputtered from surfaces (tank or spacecraft) back into the plasma and includes a study of the effects of shields on expanding plasmas.

In 1995, Fife developed a two-dimensional hybrid-PIC model based on Lentz's one dimensional by extending it radially in the accelerating channel. This model, unlike Lentz's model is designed to use a thruster's geometry as one of its inputs. Theoretically this model can be used to simulate an expanding plasma of any thruster, however, most tests were validated against an SPT-100 [*Bishaev and Kim,* 1978]. Fife's model was validated by an extensive set of electrostatic probe measurements in the plume. The model also studied low-frequency discharge oscillations, energy distribution of ions ejected from the thruster, the interaction of the thruster walls with the plasma, and the effect of facility background pressure on efficiency.

Ahedo and Martinez-Sanchez developed a one-dimensional model of the SPT providing a well defined set of governing equations for the plasma dynamics. This model, however, was focussed on the steady state plasma characteristics and did not include the discharge oscillation observed in many SPTs. Noguchi, in 1999, developed a model based on linear perturbation of the steady state variable derived by Ahedo and Martinez-Sanchez, in order to study the transient, oscillatory characteristics of an operating SPT. Noguchi's model predicted two families of modes, one basically acoustic, the other due to ionization dynamics. The modes, however, were of a higher frequency than those observed in real thruster operation.

Experimental work at MIT has been centered around developing, testing and characterizing a 50 Watt Hall Thruster. More about this work can be read in Khayms' Masters thesis [*Khayms,* 1997].

2.4 Hall Thruster Plume Research Outside MIT

2.4.1 Computational

Although it is often not readily apparent, plasma science affects our society in a myriad of ways and as a result computational modeling of plasma-based phenomena has been extensive. Techniques currently used in modeling and simulating plasma flows by the scientific community include the following methods:

- Molecular Dynamics method

- Particle-in-Cell method

- Particle-in-Cell with Monte Carlo Collisions method

- Direct Simulation Monte Carlo method

These methods have been fully developed and thus will not be reviewed here. For their detailed description, their merits and disadvantages, refer to *Birdsall and Langdon* [1991] and *Lubachevsky* [1991]. It should be noted that Oh used a combination of the PIC and DSMC methods in developing his model [*Oh*, 1997].

With respect to modeling Hall Thruster plumes in academia, Randolph and Pencil constructed an empirical plume model in order to predict contamination on surfaces exposed to the plume of an SPT-100 [*Randolph et al.*, 1994 and *Pencil et al.*, 1996]. In this model they assumed a Gaussian distribution for the current density at the thruster exit plane and they developed a sputtering model which included the energy and angular dependence of sputtering.

Bishaev et al. [1993] developed a kinetic model of the plume but the formulation is quite complex (based on a solution of a set of Boltzmann equations) and limited to simple geometries.

In 1995, *Rhee and Lewis* developed a hybrid PIC model of the SPT plume which was similar to that developed by *Samanta Roy* [1995] to model plumes from ion thrusters. It combined a PIC algorithm for the CEX ions and an analytical model for the ion beam. This model, however, is deemed to be flawed [*Oh*, 1997] as Rhee and Lewis use particles to model the difference between ion and electron charge densities.

A substantial amount of work has been done by VanGilder and Keidar in modeling EP devices. In their latest paper [*VanGilder, Keidar, and Boyd,* 1999] a very similar algorithm to Oh's is described. The difference is that Oh's model assumed a constant electron temperature whereas VanGilder *et al.* developed two cases - one assuming isothermal electrons, and one assuming a variable electron temperature. They observed that the model including a variable electron temperature showed better agreement with experimental results.

In summary, even though numerous models have been developed to describe expanding plasma plumes of EP devices, with the increased interest in employing HT devices in space missions, it is becoming apparent that fully understanding the impact of the plume in the on spacecraft subsystems is critical in the design process.

2.4.2 Experimental

Numerous research efforts in the former Soviet Union have focused on studying Hall Thruster physics since their development in the 1960s. Recognizing the numerous advantages of HTs, more and more research is being conducted in the U.S., with the hope of commercializing HT systems. Soviet researchers have done extensive developmental work on hall thrusters but it was not until the early 1990s that results began appearing in the West. Absalamov *et al.* were the first to publish results on far field plume data. These included ion distribution and witness plate measurements of erosion rates on solar cell cover glass 1 meter away from the thruster exit plane.

In the U.S., *Myers and Manzella* [1993] performed a set of experiments to validate and extend the Russian work. They mapped out the electron density, electron temperature and ion current density in the plume up to 4 meters away from the exit plane. In 1993 Manzella measured the neutral/ion distribution and the emission spectrum at the exit plane of an SPT-100. It was found that the plume consisted of 1-5% xenon neutrals (Xe), 76% - 89% singly charged ions (Xe^+), and 11.9% - 19% doubly charged ions (Xe^{++}). He also showed that the facility background pressure had an effect on the ion density in the backflow region of the plume. In a more recent study, *King* [1998] found a comparable distribution of particles ($Xe^+ = 88.8\%$, $Xe^{++} = 11\%$, $Xe^{+++} = 0.2\%$). King's study was also the first

ever documentation of the existence of triply charged xenon ions in the Hall Thruster plume.

Since the impact of HT plumes on other spacecraft sub-systems has always been a primary concern, several experiments have been conducted by Absalamov et al. and Pencil where samples of cover glasses and interconnect material are exposed to the plume at various angles and distances. In some of these experiments collimators were used to protect the samples from the material sputtered from the wall of the vacuum tank. In experiments without collimators it was seen that samples near the center-line of the beam had a net erosion whereas samples farther than 60° off the thrust line showed a net deposition of material. The source of this material, however, was the tank walls and not the thruster channel. *Randolph et al. and Pencil et al.* [1994] also performed experiments without collimators and these showed no net deposition on the samples.

Researchers at the University of Michigan have also provided comprehensive data. This data includes:

- ion fluxes, neutral fluxes, heat flux, and ion energy distribution [*King,* 1996]

- near field measurements of charge and ion density [*Kim,* 1996]

- plasma density in the plume [*Ohler et al.,* 1995]

- phase shift measurements and L-Band attenuation [*Ohler et al.,* 1996]

Since Hall thrusters are efficient, have a high Isp, and are relatively easy to operate, many companies are interested in implementing these devices in their space missions. This interest has sparked the large number of ground tests described above. It must be noted, however, that no space-based data is currently available though efforts are being made to design and carry out such experiments.

2.5 Thruster Basics

A closed-drift thruster is defined as a thruster in which ions are electrostatically accelerated in the primary thrust direction, with the accelerating electric field established by an electron current interacting with a transverse magnetic field. Figure 2.2 shows a schematic of a cylindrically symmetric design. A radial magnetic field is developed between two axially symmetric magnet pole pieces as shown. The interior volume surrounded by the mag-

net is continually filled with a low pressure propellant gas that supports an electric discharge between two electrodes. Xenon is the preferred fluid for this operation, because it has high atomic mass combined with a low ionization potential.

The anode electrode is located upstream, while the cathode electrode is located in the region directly downstream of the magnet pole pieces. The axial electrostatic field created between the anode and cathode steers some of the electrons toward the annular channel where they collide with and ionize the xenon atoms. Under the effect of the electrostatic field the ions are pushed toward the engine outlet (exit plane) at a high-speed, thus generating the thrust. In order to ensure that the ions are accelerated in a single direction, the ion cyclotron radius must be far greater than the acceleration channel length. The effect of a magnetic field generated by the peripheral coils is used to increase the probability of an electron and atom collision in the annular channel and to focus the ion beam at engine outlet. The unused electrons can neutralize the ions after they have been ejected from the engine, thereby preventing the entire propulsion system from accumulating electrical charge.

The axial electric field also interacts with the radial magnetic field to generate the Hall current in the azimuthal direction. The unique feature, however, of this device is that the major current flow is the Hall current perpendicular to the electric field, hence the name Hall accelerator or Hall thruster.

This device is particularly suited for missions requiring a specific impulses in the range of 1000 to 2000 sec. Thrust levels in the $3mN$ to $2N$ range have been obtained. The overall thrust is determined by the size and power level of the device, but no obvious upper limit has been found. At the low power end, the plasma tends to become too dense and aggressive, limiting thruster life.
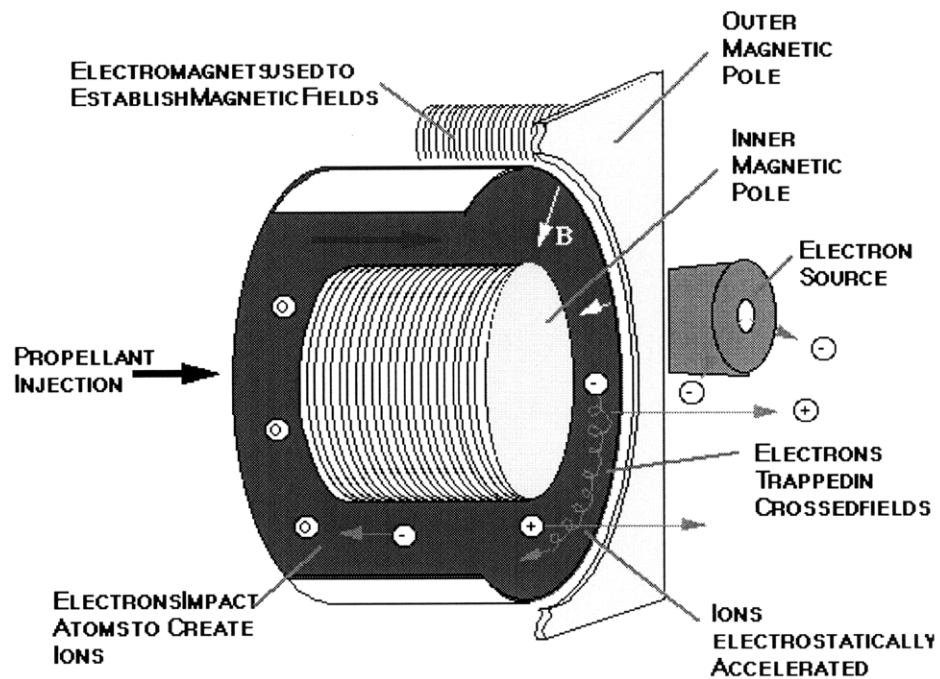
Figure 2.2 Cross-section of a typical Hall Thruster

A variety of different configurations of these thrusters have been developed in the former Soviet Union and flown on several different spacecraft but there are primarily two types of designs. One device is constructed such that the channel walls are made of a dielectric material (e.g. Boron Nitride) and is referred to as a Stationary Plasma Thruster (SPT) or closed-drift extended acceleration thruster. The other device is called the 'thruster with anode layer' (TAL). This differs from the SPT in that its acceleration channel is relatively shorter and the side walls are made of a conductive material instead.

The Stationary Plasma Thruster, developed in the former Soviet Union by Morozov and manufactured by Fakel, is often used as a baseline for analyzing physical properties and performance. Many experimental and numerical tests have been performed in an attempt to better understand the physics of the accelerating process within the thruster, the expansion of the plasma in a vacuum as well as the effect of the plasma on various spacecraft surface samples. The characteristics of the thruster used for purposes of this research are listed in Table 2.1 below

19

One issue associated with HT devices is that complete ionization cannot be achieved with reasonable levels of power, and hence, neutral gas is emitted at thermal speeds. These slow neutrals are of interest because they charge-exchange with the fast beam ions producing fast neutrals and slow ions which can be influenced by local electric fields in the plume. The electric field structure in the plume, as seen in experiments and in computational models, is radial, and hence the slow ions are pushed out of the beam and move back towards the spacecraft.

Parameter	Numerical Value
Specific Impulse	1610 sec.
Specific Impulse (w/o cathode)	1735 sec.
Thrust	84.9 mN
Discharge Voltage	300 V
Discharge Current	4.5 A
Power	1350 Watts
Efficiency	49.7%
Efficiency (w/o cathode)	53.5%
Inner Insulator Diameter	56 mm
Outer Insulator Diameter	100 mm
Propellant	Xenon
Propellant Flow Rate	5.37 mg. / sec.
Fraction of Propellant Directed to Cathode	5% - 10% 7.1% is assumed in model
Electron Temperature in Plume	2 - 4 eV
Axial Ion Velocity	~17,000 m/s
Fraction of Propellant Ionized in Discharge Chamber	> 95%

Table 2.1: SPT-100 Characteristics
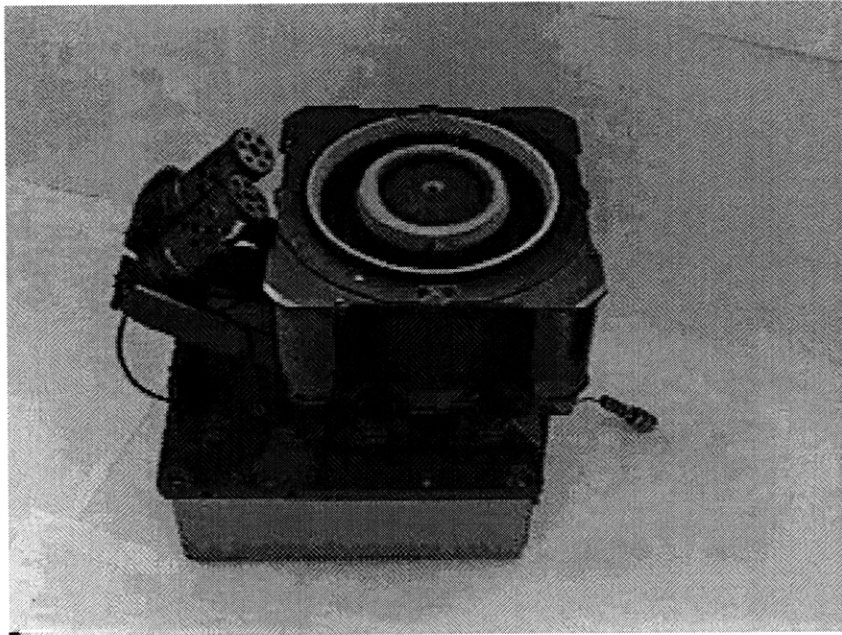
Figure 2.3   The SPT-100
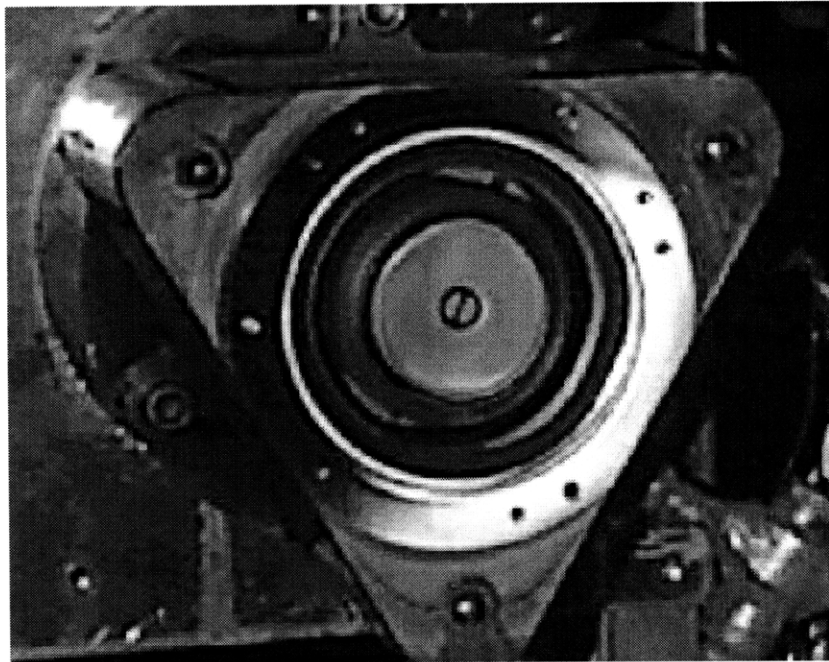
Figure 2.4   The TAL-55
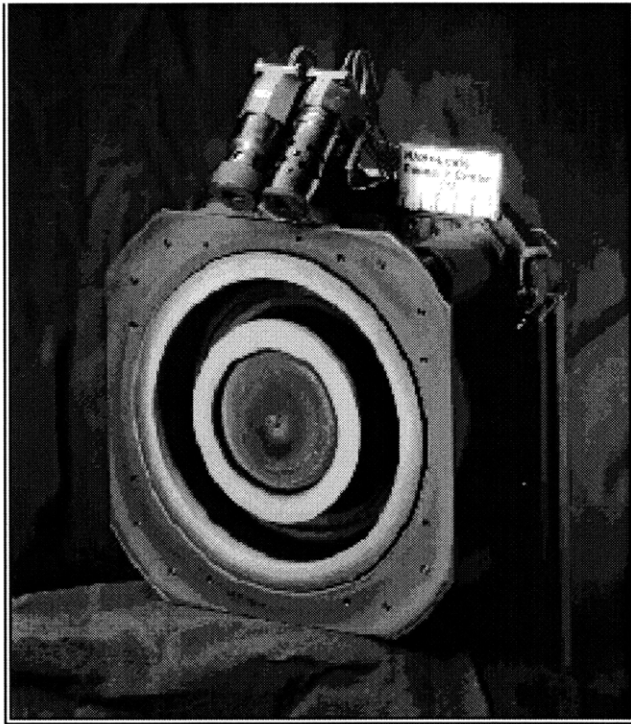
Figure 2.5   Hall Thruster - SPT-100
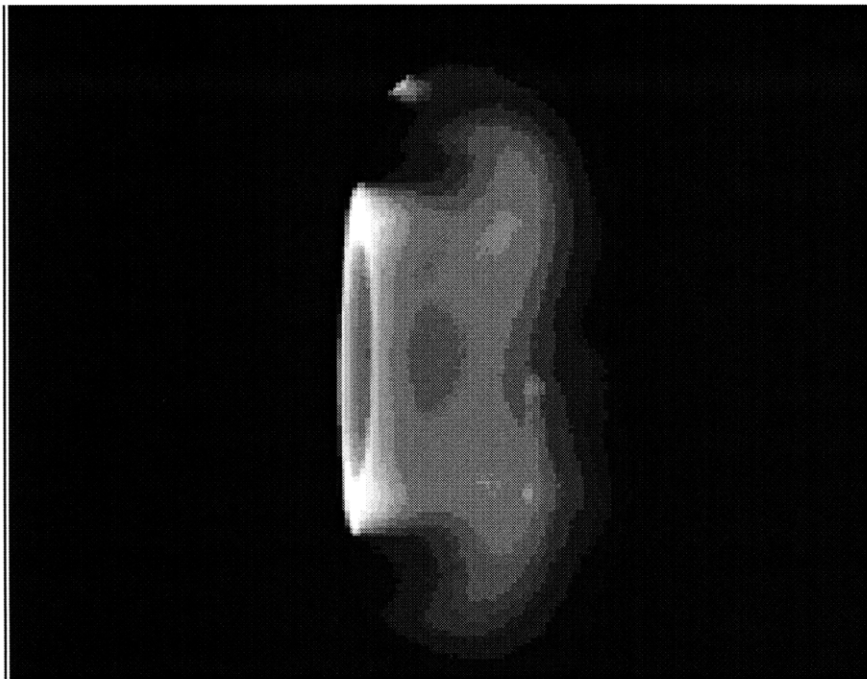
Figure 2.6   Hall Thruster Plume Cross-Section

Chapter 3

The Sputtering Process

3.1 Introduction

Sputtering is the removal of surface atoms from a target material by bombarding the latter with energetic particles. It is commonly measured by the sputtering yield, which is the average number of atoms removed from the surface of the target per incident particle. Aside from sputtering other effects also take place when particles bombard surfaces. These include backscattering as well as trapping and reemission of incident particles, desorption of surface layers, the emission of electrons, the emission of photons and a change in surface structure and topography of the target material. To date, many experiments involving sputtering of monoatomic targets (metals) with noble gases have been conducted, though more and more experiments including compounds and alloys are being performed. An excellent review of sputtering phenomena is provided by *Behrisch et al.* in *Topics in Applied Physics* series published by Springer-Verlag. A more recent review, focused on the low-energy end, was reported by *Duchemin et al.* [1997].

Sputtering used to be considered as the undesired effect taking place when cathodes were eroded and plasmas were contaminated but today, sputtering is widely applied to surface cleaning and etching, for thin film deposition, for surface layer analysis and for sputter ion sources. However, sputtering as pertaining to satellite design and integration, is still considered an undesired effect.

3.2 The Sputtering Yield

Sputtering, the removal of atoms from a target material by impinging ions, is usually

defined as the average number of atoms removed from the surface of a target material (solid) by each impinging ion. The incident particles can be ions, neutrals, electrons or energetic protons. In the case of an EP device where the impinging particles are usually monoatomic (e.g. xenon) ions each of the incident ions is counted separately. When counting the number of particles that have been removed from the surface of a material only those of the solid (target) are counted, while the incident particles which have been reflected or reemitted are not counted.

Sputtering yields for energetic particles (keV - MeV energy range) are usually in the range of $10^{-5} < Y < 10^3$ atoms per incident particle but they depend on the following factors:

- incident particle energy
- incident particle mass
- incidence angle (the angle between the particle direction and the surface normal)
- mass of the target atoms
- crystallinity and crystal orientation and surface topography of the target material
- surface binding energy of the target material

It has been found that the yield is almost independent of the temperature and that there is a (material dependent) threshold energy (20eV - 100eV) below which no sputtering occurs. The sputtering yield usually increases with incident particle energy but peaks with a broad maximum of 5 - 50 keV. At higher incident energies, the sputtering yield decreases since the impinging ions burrow deeper into the target material and are forced to shed their energy deep within the target material and further away from the surface layers.

It has been observed that when ions impinge on a target at oblique angles the sputtering yield tends to increase monotonically with incidence angle until a peak between 60 and 85 degrees. This peak is a function of the incident particle mass and energy as well as the surface structure of the target material. If the target material is a single crystal, sputtering is affected by the target crystal orientation with respect to the impinging angle. For example, the yields for particles impinging near the three major close-packed crystal axes are 2 to 5 times lower than for other angles of incidence. Also for the close-packed direc-

tions the maxima in the energy dependence of sputtering tends to be in a lower energy range.

There are three mechanisms by which particles are emitted form the surface of a bombarded material. In the single-knockon regime the bombarding ion transfers energy to target atoms which, after having undergone a number of collisions, are ejected through the target surface provided they have energy in excess of the binding energy of the target. It must be noted that the atoms from the ion-target collisions gain enough energy to get sputtered, but not enough to generate recoil cascades - target atoms dislocated from their original lattice positions and undergoing more collisions. In the linear cascade regime the atoms resulting from the ion-target collisions gain sufficient energy to generate recoil cascades of which some may reach the surface of the target. The density of the recoil atoms, however, is low enough to ensure that knock-on collisions are dominant and collisions between moving atoms is infrequent. In the spike regime, on the other hand, the density of the recoil atoms is so high that most of the atoms within a given volume are in motion.

According to Behrisch *et al.* the charge states of the emitted particles is also important, though for sputtered metals a large fraction of the sputtered atoms emerge as neutrals in their ground states. Within the target material, however, dislocated atoms move towards the surface layer in an ionized or excited state. This indicates that the fundamental event in the excitation process involves the interaction of one emerging atom with the target surface. The probability of an atom being neutralized or ionized determines the state of the sputtered atom, though the initial state of the target atom is not significant as the probability of maintaining its charge state as it traverses the target material to the surface is very small at typical energies of sputtered atoms (~10eV). Since a large fraction of the sputtered atoms emerge as neutrals in the ground state, for purposes of this research it is assumed that particles (both reflected xenon neutrals and sputtered atoms) emitted from any surface (tank or spacecraft) will be in the neutral state

3.3 Empirical Formulas for Sputtering

3.3.1 Matsunami's Empirical Formulation

Light-ion sputtering is mainly due to collision cascades created by ions backscattered

from the interior of a solid target, whereas heavy-ion sputtering is due to collision cascades directly generated by incoming ions. This difference is particularly important when studying the angular dependence of the yield sputtering in the low energy range. For example, the angular dependence of the threshold energy has a minimum at 60° for heavy ion-sputtering whereas for light-ion sputtering there is no distinctive minimum [*Behrisch, 1983*])

Analytical expressions for sputtering data have been derived by many authors. These have ranged from theories, empirical formulas and computer simulations of sputtering processes. Sigmund successfully developed a theory describing the effects of different ion-target material combinations by solving the linearized Boltzmann Equation and by relating sputtering to other ion-bombardment phenomena. One of Sigmund's most important conclusions is the fact that backward sputtering yield is proportional to the energy deposited at the surface. He derived a sputtering yield formula for ions impinging normally on a target material:

$$Yield = \frac{0.042\alpha(m_2/m_1)S_n(E)}{U_s} \tag{3.1}$$

where E is the incident particle energy and U_s is the surface binding energy (usually equal to the sublimation energy of the target material). $S_n(E)$ is the Lindhard nuclear stopping cross section - Equation (3.6) - and $\alpha(m_2/m_1)$ is the energy-independent function of the mass ratio between the target atom mass, m_2 and the incident ion mass, m_1
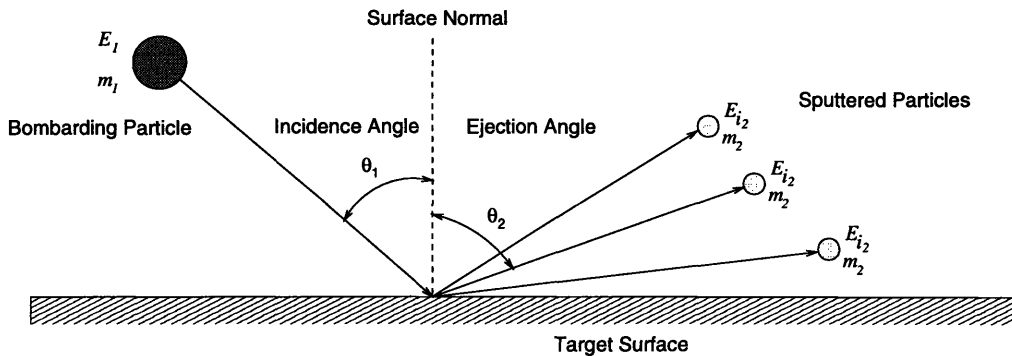
Figure 3.2   Schematic of Sputtering Geometry

28

Experiments have proven that Sigmund's formula has its limitations. It does not predict yields for light-ion sputtering and low-energy sputtering accurately. Experimental results do not agree very well with calculated values of sputtering for the low-energy sputtering case and this discrepancy seems to indicate that there has to be a lower limit below which sputtering does not occur - the sputtering threshold. This threshold, however, depends on the impinging ion incidence angle.

Yamamura *et al.* [1983] modeled the angular dependence of the threshold energy for heavy-ion sputtering and showed that it has a minimum near 60°. The threshold energy of heavy-ion sputtering is a decreasing function of the angle of incidence because of the anisotropic velocity distribution of recoil atoms near the surface, but for grazing angles it increases with angle of incidence as a result of surface channelling. Thus even if the ion energy is less than the threshold energy at normal incidence, a finite number of target atoms will be sputtered at oblique incidence in the case of heavy-ion sputtering.

Bohdansky *et al.* and Matsunami *et al.* have proposed empirical formulae which take into account this threshold energy. These formulae are valid for sputtering yields at normal angles of incidence only. *Bohdansky et al.* [1980] divided the sputtering process into the near threshold regime and the linear cascade regime.

For the near threshold regime the following empirical formula was found to predict the sputtering yield:

$$Yield = Q_B(m_2, m_2, U_s) Y_N\left(\frac{E}{E_{th}}\right)$$ (3.3)

$$Y_N\left(\frac{E_{th}}{E}\right) = 0.0085\left(\frac{E}{E_{th}}\right)^{1/4}\left[1 - \left(\frac{E_{th}}{E}\right)\right]^{7/2}$$ (3.4)

where Q_B is a fitting parameter and E_{th} is the threshold energy. For the linear cascade regime Sigmund's formula was adopted and it was found that the analytical expression for the high energy regime could be extended to the near threshold regime.

Matsunami *et al.* proposed an even simpler formula applicable to all ion-target combinations. In their work they took Sigmund's original formula as well as the threshold energy into account and arrived at:

$$Yield = \frac{0.042\alpha(m_2/m_1)S_n(E)}{U_s}\left[1 - \left(\frac{E_{th}}{E}\right)^{\frac{1}{2}}\right] \qquad (3.5)$$

which is the Matsunami first formula where Lindhard's nuclear stopping cross section is:

$$S_n(\varepsilon) = \frac{3.441\log(\varepsilon + 2.718)\sqrt{\varepsilon}}{1 + 6.355\sqrt{\varepsilon} + \varepsilon(-1.708 + 6.882\sqrt{\varepsilon})} \qquad (3.6)$$

and

$$\varepsilon = \frac{E}{E_{th}} \qquad (3.7)$$

In addition, Matsunami *et al.* showed that the average values of α nd ζ_1, when using the first Matsunami formula, had the following mass dependence:

$$\alpha = 0.1019 + 0.0842(m_2/m_1)^{0.9805} \text{ for } m_2/m_1 < 2.163 \qquad (3.8)$$

$$\alpha = -0.4137 + 0.6092(m_2/m_1)^{0.1708} \text{ for } m_2/m_1 > 2.163 \qquad (3.9)$$

$$\varsigma_1 = 4.143 + 11.46(m_2/m_1)^{-0.5004} \text{ for } m_2/m_1 < 3.115 \qquad (3.10)$$

$$\varsigma_1 = 5.809 + 2.791(m_2/m_1)^{0.4816} \text{ for } m_2/m_1 > 3.115 \qquad (3.11)$$

and

$$\varsigma_1 = \frac{E_{th}}{U_s} \qquad (3.12)$$

Matsunami *et al.* showed that the first empirical formula includes implicitly the effect of inelastic stopping on sputtering yield and it takes into account the threshold effect in the original Sigmund formula. The validity of this formula has been successfully examined by Matsunami *et al.* for monoatomic targets, and best fit values for α and E_{th} are summarized in [*Yamamura, Matsunami and Itoh*, 1982].

30

Even though the first Matsunami formula predicts well the energy-dependence of the sputtering yield for perpendicular incidence of ions, improved second and third Matsunami formulae were subsequently derived. This included factorizing α into two terms (the inelastic part and the elastic part). The second formula Matsunami *et al.* proposed is an interpolation between an analytical formula for low-energy heavy-ion sputtering and the one for high-energy light-ion sputtering. The third formula is discussed in the next section.

The group also showed that the third formula useful for the preliminary estimation of the sputtering yield over a wide range of ion-target combinations (*Yamamura*, 1983). It was also shown that the threshold energy for heavy-ion sputtering is determined primarily by the anisotropic velocity distribution of recoil atoms. This is directly related to the under-cosine angular distribution of sputtered atoms though a rough estimation of the threshold shows that this angular distribution becomes a cosine distribution with an increase of the mass ratio. In the case of light-ion sputtering, however, the anisotropic velocity distribution of recoil atoms contribute positively to the sputtering yield. Thus sputtering in this case obeys the over-cosine rule. An exhaustive derivation of these formula is presented in [*Yamamura, Matsunami and Itoh*, 1982].

3.3.2 Yamamura's Empirical Formulation for Angular Dependence of Yield

Yamamura *et al.* derived a normalized empirical formula of the form:

$$\frac{Y(\theta)}{Y(0)} = t^f e^{(-\Sigma(t-1))} \tag{3.4}$$

where θ is the angle of incidence measured from the surface normal, $Y(\theta)$ is the sputtering yield at an angle of incidence, θ, $Y(0)$ is the sputtering yield at the normal angle of incidence,

$$t = \frac{1}{\cos(\theta)} \tag{3.5}$$

$$\Sigma = f\cos(\theta_{optimum}) \tag{3.6}$$

where f and Σ are adjustable parameters which are determined by the least-square method so as to fit the empirical formula to available experimental data. θ_{opt} is the angle of

incidence at the maximum yield. Yamamura showed that when the best fit-values of $90^0 - \theta_{opt}$ were plotted as a function of ψ the following equation represented the relationship:

$$\theta_{opt} = 90^0 - 286\psi^{0.45} \tag{3.7}$$

where ψ is defined as:

$$\psi = \left(\frac{a}{R_0}\right)^{3/2}\left(\frac{Z_1Z_2}{\sqrt{(Z_1^{2/3} + Z_2^{2/3})}}\frac{1}{E}\right)^{1/2} \tag{3.8}$$

where E is in eV, where $R_0 = N^{-1/3}$ is the average lattice constant of the target, N is the number density of the target material and the Thomas-Fermi screening radius of the interatomic potential is,

$$a = \left(\frac{0.4685}{\sqrt{(Z_1^{2/3} + Z_2^{2/3})}}\right) \text{ in Angstroms} \tag{3.9}$$

It must be noted here that when Yamamura *et al.* were determining the best-fit values of f and Σ experimental data which did not have maximum values or which did not have data at normal incidence were excluded. The factor f depends on the energy through

$$f = f_s\left(1 + \frac{2.5(1 - \zeta_2)}{\zeta_2}\right) \tag{3.10}$$

where ζ is:

$$\zeta_2 = 1 - \left(\frac{E_{th}}{E}\right)^{1/2} \tag{3.11}$$

The threshold energy E_{th} for the third Matsunami formula has the following empirical form:

$$E_{th} = U_s[1.9 + 3.8(m_1/m_2) + 0.314(m_2/m_1)^{1.24}] \tag{3.12}$$

The best-fit parameters and their average values are compiled in [*Yamamura*, 1983] by Yamamura *et al.* for various ion-target combinations. Yamamura *et al.* found that agree-

ment is satisfactory over a wide range of incidence angles as well as a variety of ion-target combinations.

Yamamura's formula gives the normalized sputtering yield. In order to obtain the absolute yield $Y(\theta)$, the sputtering yield at normal incidence needs to be calculated. The empirical formulae for the sputtering at normal incidence have been proposed by Bohdansky et al., Matsunami et al. and Yamamura et al.. Yamamura et al. recommend to use the third Matsunami formula which has the form:

$$Yield(E) = \frac{PS_n(\varepsilon)[1 - \sqrt{(E_{th}/E)}]^{2.8}}{(1 + 0.35U_sS_e(\varepsilon))} \tag{3.13}$$

where,

$$P = \frac{0.042E_LN\alpha(m_2/m_1)Q(Z_2)}{R_LU_s} \tag{3.14}$$

and

$$R_L = \frac{1}{(\pi a^2 N\gamma)} \tag{3.15}$$

$$S_e(\varepsilon) = k\sqrt{\varepsilon} \tag{3.16}$$

$$\gamma = \frac{4m_1m_2}{(m_1 + m_2)^2} \tag{3.17}$$

$$E_L = \left(\frac{m_1 + m_2}{m_2}\right)\left(\frac{Z_1Z_2e^2}{a}\right) \tag{3.18}$$

where Z_1 and Z_2 are the atomic numbers of the projectile and target atoms respectively and m_1 and m_2 are their respective masses. Also the inelastic coefficient k of $S_e(\varepsilon)$ is given as:

$$k = \frac{0.0793(Z_1)^{1/6}(Z_1Z_2)^{1/2}(m_1 + m_2)^{3/2}}{[(Z_1^{2/3} + Z_2^{2/3})^{3/4}]m_1(m_1m_2)^{1/2}} \tag{3.19}$$

The parameter $\alpha(m_2/m_1)$ for Matsunami's third formula is represented as:

$$\alpha(m_2/m_1) = 0.08 + 0.164(m_2/m_1)^{0.45} + 0.0145(m_2/m_1)^{1.29} \qquad (3.20)$$

and $Q(Z_2)$ is listed for each element by Yamamura *et al.* [1983]. $[Q(Z_2)_{aluminum} = 1.1;$ $Q(Z_2)_{silicon} = 0.75;$ $Q(Z_2)_{iron} = 1.12;$ $Q(Z_2)_{silver} = 1.13;$ $Q(Z_2)_{gold} = 0.98]$

3.4 Angular Distribution of Sputtered Material

Yamamura *et al.* derived a formula for the angular distribution of the sputtered atoms as a function of the impinging ion's energy, E, the azimuthal angle, ϕ, and the angle, θ_1, that the ejected particle makes with the surface normal upon ejections - Equation (3.23) - this formula takes into account the threshold effect, and it coincides with Matsunami's first empirical formula [*Yamamura*, 1981].

$$S(E, \theta, \phi, \theta_1) = \frac{0.042}{\pi}\left(\frac{\alpha(m_2/m_1)S_n(E)\cos\theta_1}{U_s}\right)\left[1 - \frac{1}{2}\sqrt{\left(\frac{E_{th}}{E}\right)}\left\{\cos\theta\gamma(\theta_1) + 3\frac{\pi}{4}\cos\phi\sin\theta\sin\theta_1\right\}\right] \qquad (3.21)$$

where, $S(E, \theta, \phi, \theta_1)$ is the differential yield (yield per unit exit solid angle, $d\Omega_1 = sin(\theta_1)d\theta_1 d\phi)$, for an incident ion with energy E and angle θ, and

$$2\gamma(\theta_1) = \frac{(3(\sin\theta_1)^2 - 1)}{(\sin\theta_1)^2} + \frac{(\cos\theta_1)^2(3(\sin\theta_1)^2 + 1)}{(\sin\theta_1)^3} \times \ln\frac{1 + \sin\theta_1}{1 - \sin\theta_1} \qquad (3.22)$$

For small θ_1, the above formula can be reduced to

$$S(E, 0, \theta_1) = \frac{0.042}{\pi}\left(\frac{\alpha(m_2/m_1)\cos\theta_1}{U_s}\right)\left[1 - \sqrt{\left(\frac{E_{th}}{E}\right)}\left\{1 + \frac{5}{3}(\cos\theta_1)^2\right\}\right] \qquad (3.23)$$

for perpendicular incidence. By integration, the total yield (Matsunami's first formula) results as follows

$$Yield(E, \theta) = \int_0^{2\pi}\int_0^{\frac{\pi}{2}} S(E, \theta, \phi, \theta_1)\sin\theta_1(d\theta_1)d\phi \qquad (3.24)$$

For a derivation of these formulas refer to Yamamura [1981]. **Note:** The published formulae [*Yamamura*, 1981] lack some of the factors which this work has found to be neces-

34

sary: (a) the $1/\pi$ fraction in Equation (3.21) and (b) the factor of 2 on the left side of Equation (3.22) .

The agreement with Wehner's experimental results [*Wehner*, 1960] is very good and Equation (3.23) predicts well the heart-shaped distributions of sputtered atoms for normally incident ions and preferential forward ejection of sputtered atoms. The relation, however, is valid only for heavy-ion sputtering. For light-ion sputtering, *Weissman and Behrisch* showed that the angular distribution of sputtered material obeys the over-cosine law instead of the under-cosine form implied by Equation 3.2.

3.4.1 The Sputtering Process - Computational Modeling

Numerous computational models addressing the sputtering process have been developed to date. They are either Monte Carlo based or lattice based programs. The main difference between these methods are the search methods for collision partners, the handling of simultaneous collisions, the inclusion of time dependence, the treatment of inelastic kinematics, the possible handling of collisions between moving atoms and the variety of calculable data. Because of its ready availability, one of the codes used in this work is the SRIM (Stopping Ranges of Ion in Matter) package. A list of available simulation packages was compiled by *Eckstein* [1991] and is reproduced in the tables below.

Name	Origin	Authors
ACAT	Atomic Collisions in Amorphous Targets	Takeuchi, Yamamura
BABOUM		Abel et al.
BEST	Boltzmann Equation Solving Tool	Vicanek, Urbassek
CASCADE		Pugacheva
COLLIDE		Beeler
DYACAT	Bynamical ACAT	Yamamura
ERPEX		Tatarkiewicz
EVOLVE		Roush et al
HERAD	Heterogenous Radiation Damage	Attaya, Kulcinski
HIDOS		Schonborn et al.
IMPLNT		Davisson

Table 3.2: Monte Carlo Based programs [*Eckstein*, 1991]

Name	Origin	Authors
ITMC	Ion Transport in Materials and Compounds	Hassanein, Smith
PERST	Pervaya Stenka	Nikiforov et al.
PIBER		Adesida, Karapiperis
RITA	Recoil Implantation Through Amorphous	Desalvo, Rosa
ROMEO		Melker, Romanov
SASAMAL	Simulation of Atomic Scattering in Amorphous Material based on Liquid Model	Miyagawa, Miyagawa
SAVOY		Jackson
TCIS		Cui, Li
TRIDYN	TRIM.SP Dynamical	Moller, Eckstein
TRIM	Transport of Ions in Matter	Biersack, Haggmark
TRIM.SP	TRIM Sputtering	Biersack, Eckstein
TRIM85		Ziegler et al
TRIPOS	Transport of Ions in Polyatomic Matter	Chou, Ghoniem

Table 3.2: Monte Carlo Based programs [*Eckstein*, 1991]

Name	Authors
ACOCT	Yamamura, Takeuchi
ARGUS	Jackson et al.
BACKS	Hutchence, Honzeas
CASCADE	Beeler
CENTAUR	Jackson et al.
COSIPO	Hautala
EDI	Preuss
FLUX	Smulders, Boerma
MARLOWE	Robinson, Torrens
MORLAY	Beitat (Taglauer et al.)
OKSANA	Shul'ga
RECOIL	Teplov et al.

Table 3.3: Lattice Based Programs [*Eckstein*, 1991]

36

Name	Authors
RETTUPS	Fustoss et al.
TAVERN	Jackson

Table 3.3: Lattice Based Programs [*Eckstein*, 1991]

SRIM

SRIM is a DOS-based package, initially developed by *Ziegler, Biersack* and *Littmark*, used to calculate the stopping and range of ions (10 eV - 2 GeV/amu) in matter using a quantum mechanical treatment of ion-atom collisions. A full description of the algorithms used in this program can be found in *"The Stopping and Range of Ions in Solids"*, by J. F. Ziegler, J. P. Biersack and U. Littmark, Pergamon Press, New York, 1985 (new edition in late 1996). This book also provides the source code for the SRIM programs including a full explanation of its physics. Applications of SRIM as well as the accuracy of the simulation are also highlighted. TRIM is the most comprehensive program included in the SRIM package. It will accept complex targets made of compound materials up to eight layers, each of different materials - this is how molecular substrates are modeled. It calculates the final three-dimensional distribution of the ions and also the kinetic phenomena associated with the ion's energy loss: target damage, sputtering, ionization and phonon production. TRIM results were compared with the sputtering yields obtained by the theory developed by Matsunami *et al.* [1980] and Yamamura *et al.*[1983]. For extensive comparisons refer to [*Yamamura, Itikawa, Itoh,* 1983].

3.5 The Sputtering Process - Experimental Work

A synopsis of sputtering work related to the aerospace domain is outlined in this section. Since xenon is the primary fuel type used in EP devices only work covering xenon ion sputtering was reviewed.

In the 1960's, *Rosenberg and Wehner* [1962], *Stuart and Wehner* published data on xenon ions with energies down to 100eV while more recently *Bhattacharjee et al.* published data for xenon ions on molybdenum in the 150 eV to 600 eV energy range. In 1999, *Duchemin and Polk* [1999], published results [for xenon ions on molybdenum] in the 100 eV to 1 keV range. Duchemin and Polk compared their data to results published in the

1960's and found satisfactory agreement. It was shown that Matsunami's third formula was in relatively good agreement with experimental data and the TRIM simulation. In their paper, they also mentioned extending their work to the sub-100 eV range and increasing the variety of target materials - results of which have not been published yet [*Duchemin and Polk*, 1999].

3.6 Xenon Ion Sputtering of Metals

Since xenon is the dominant species in the plume region, only xenon induced sputtering is considered in this model. A good understanding of the ion-erosion processes and knowledge of the sputtering yield as a function of plume ion energy and incidence angle, for various materials making up the space craft is absolutely necessary. These parts are, primarily, the solar arrays, sensitive optical instruments, thermal (insulation) blankets and radiative shield, while the materials of interest are quartz, aluminum, silver and gold. These materials were chosen not only because there is a large data set on the effects of xenon ion impingement on them, but also because they constitute a large fraction of a general spacecraft's components.

3.7 Sputtering Yield for Aluminum, Silicon, Iron, Silver and Gold

This section presents the theoretical sputtering yields for xenon ions impinging on aluminum, silicon, iron (stainless steel), silver, and gold. These yields have been calculated using the theories developed by Matsunami *et al.* (third formula) and Yamamura *et al.* in Section 3.3 and Section 3.3.2 . For a detailed comparison between sputtering theory and experimental results refer to [*Yamamura, Itikawa, and Itoh*, 1983] wherein a large fraction of the published data on sputtering yields at perpendicular incidence can be found. These references show good agreement between theory and experiment over a large range of energies and ion-target combinations (with few exceptions - see below).

There is a discrepancy between theoretical and experimental results for heavy ion sputtering in some cases for a number of reasons. These have been interpreted by Behrisch as being caused by energy dependent nonlinear effects in the collision cascade. Until now

it has been assumed (but questioned extensively in the literature) that collisions are binary and elastic and that the target is assumed to be structureless and characterized by a density N of randomly distributed atom which are assumed to be point particles with characteristic collision cross sections. Detailed theoretical discussions of the mechanisms behind the nonlinear effects can be found in "Sputtering by Particle Bombardment I: Introduction and Overview." *Topics in Applied Physics,* Vol 47, 1981 by R. Behrisch.

3.7.1 Sputtering Yield vs. Incident Energy

When studying the dependence of sputtering yield on incident particle energy it must be noted that for noble gas projectiles, the chemical effects of implanted projectile species are negligible and thus allow a better basis for comparisons with experiments than in most other cases. As shown in Equation (3.1) the sputtering yield is proportional to the nuclear stopping power and this is the only dependence in energy. In his book [*Behrisch,* Vol. 1, 1981] Behrisch shows that for neon and argon the sputtering data (in the keV range) are in agreement with sputtering theory but for krypton and xenon the experimental yields are higher than theoretical results by as much as 40%. The most prominent difference is seen in experiments on gold targets.

At the time of Oh's work it was fairly difficult to obtain data for solar cell coverglass and for the silver interconnects. Thus experimental data for silver, quartz and silicon were used by Oh in his model. Oh fitted a curve to the data obtained by *Rosenberg* [1994] for xenon ions normally incident on a silver target and for xenon on silicon to characterize the sputtering yield. He also used a curve fit to data obtained by *Randolph* [1994] for argon sputtering on quartz glass as data involving xenon was not readily available. It is assumed that quartz is tougher than most glasses, thus the curve fit used might underestimate the real sputtering yield. In all cases, the sputtering yield curves used are for xenon striking normal to the target surface.

$$Yield_{silver} = 7.334 \times 10^{-3} E - 0.29511 \text{ for xenon on silver} \tag{3.25}$$

$$Yield_{quartz} = 7.105 \times 10^{-4} E - 0.01815 \text{ for argon on quartz glass} \tag{3.26}$$

$$Yield_{silicon} = 1.0577 \times 10^{-3} E - 0.12115 \text{ for xenon on silicon} \tag{3.27}$$

More recently Roussel et al. [*Roussel, 1997*] measured the sputtering yield of standard coverglass (cerium-doped borosilicate) as a function of incidence angle and he fitted a polynomial to his data (see Equation (3.5))

$$Yield_{coverglass}(\theta) = 0.42 - 0.0053\theta + 0.0015\theta^2 - (7 \cdot 10^{-6})\theta^3 - 10^{-7}\theta^4 \qquad (3.28)$$

where θ is the incidence angle of the impinging xenon atoms measured in degrees and the incidence energy was 300eV. **Note:** The experiment was done for only one incident energy - 300eV.
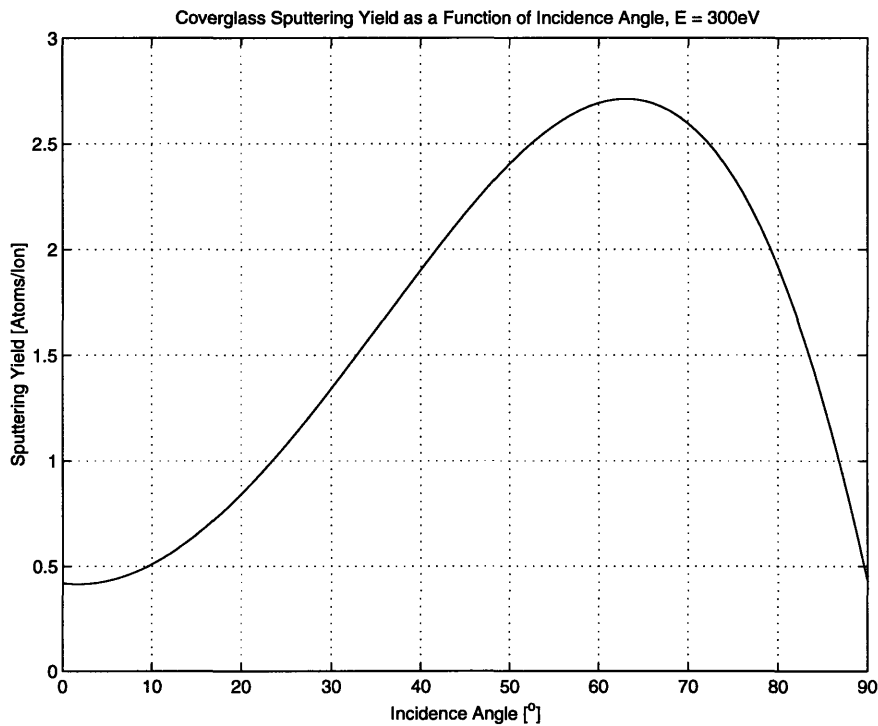
Figure 3.29 **Coverglass sputtering yield vs. Incidence Angle for Xenon Ions at 300eV**

In Figure 3.30 Randolph's experimental results for argon on quartz are seen to be comparable to the theoretical results (Matsunami's and Yamamura's) for argon on silicon. Rosenberg's results for xenon on silicon, however, were comparable up to 500 eV. Above this energy range the sputtering yields predicted by Matsunami (third formula) and Yamamura were lower than the experimental values. (see Figure 3.31)

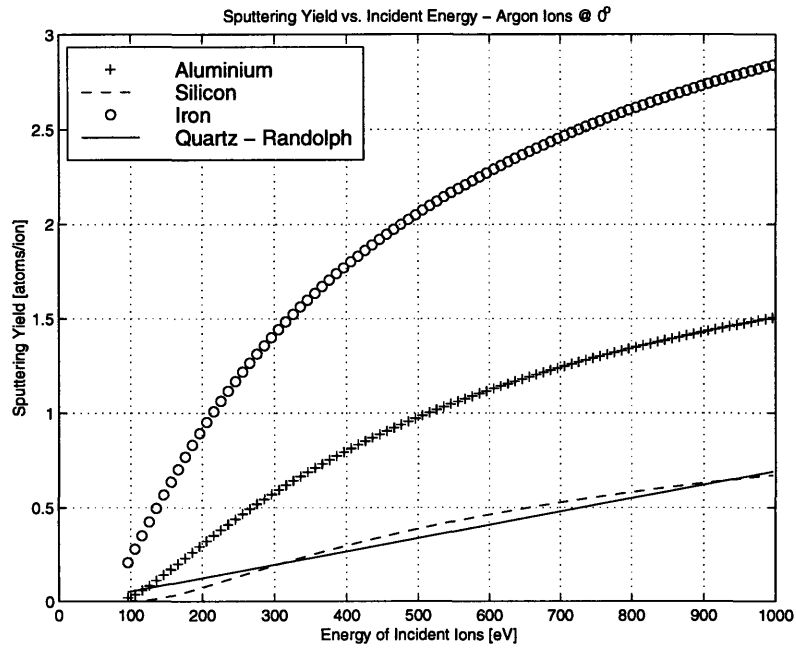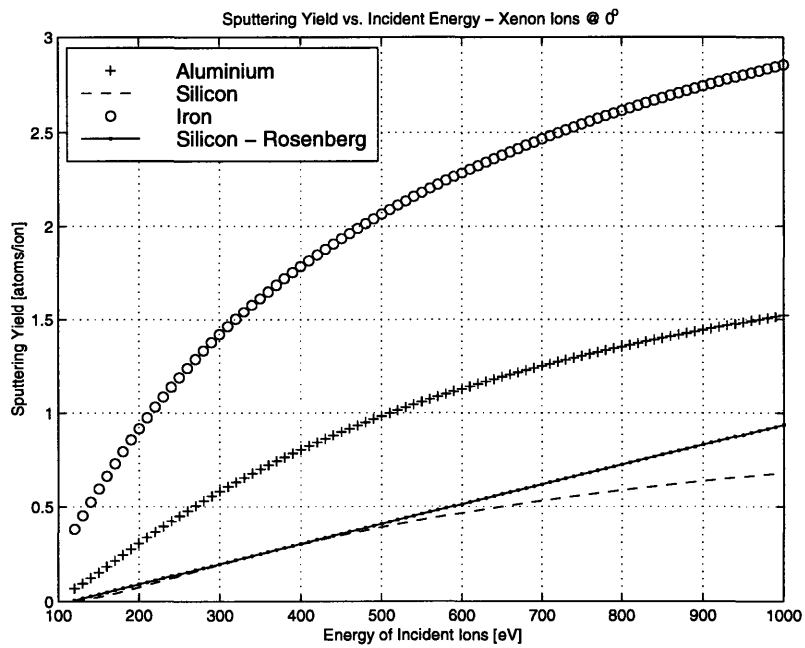**Figure 3.30 Sputtering Yield vs. Incident Energy - Argon Comparison**

Figure 3.31 Sputtering Yield vs. Incident Energy - Xenon Comparison

The graph in appendix A shows the theoretical sputtering yields as a function of incident energy for xenon ions impinging (at 45° angle of incidence) on aluminum, silicon, and iron targets. These show representatives values for the sputtering yield. For a more comprehensive set of results (range of energy and angles of incidence) refer to Appendix B.

3.7.1 Sputtering Yield vs. Incidence Angle

Wehner and *Fetz* [1959] were the first to obtain qualitative information describing the angular dependence of the sputtering yield. For heavy ion bombardment in the keV range a number of scientists found a $cos^{-1}(\theta)$ dependence, where θ is measured from the surface normal. *Sigmund*, however, showed that this dependence is only valid for large ion mass-to-target mass ratios. For smaller mass ratios a faster variation was predicted. Numerous experimental data [*Behrisch*, 1981] showed a stronger dependence on θ than on $cos^{-1}(\theta)$ but in all cases studied, the yield was seen to reach a maximum at angles between 60° and 80°, and it decreased for larger angles.

In his model, Oh did not include the effects of angle of incidence on the sputtering yield. Since the maximum yield tends to occur at non-normal angles of incidence it is possible that Oh over-estimated the erosion rates of surfaces due to sputtering. The figure below (Figure 3.32) shows the variation of the angle at which maximum sputtering occurs as a function of incident energy. This was calculated using the set of equations discussed in Section 3.3.2 .
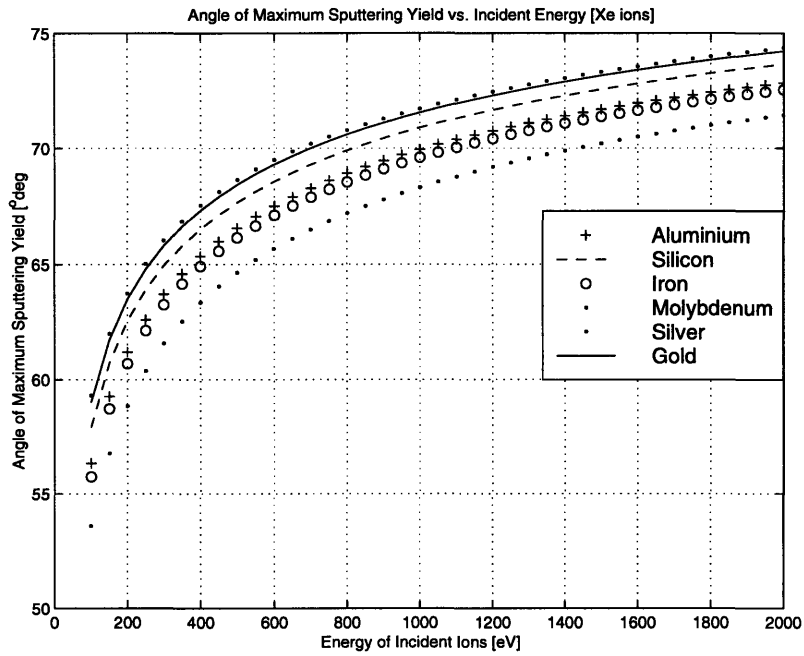
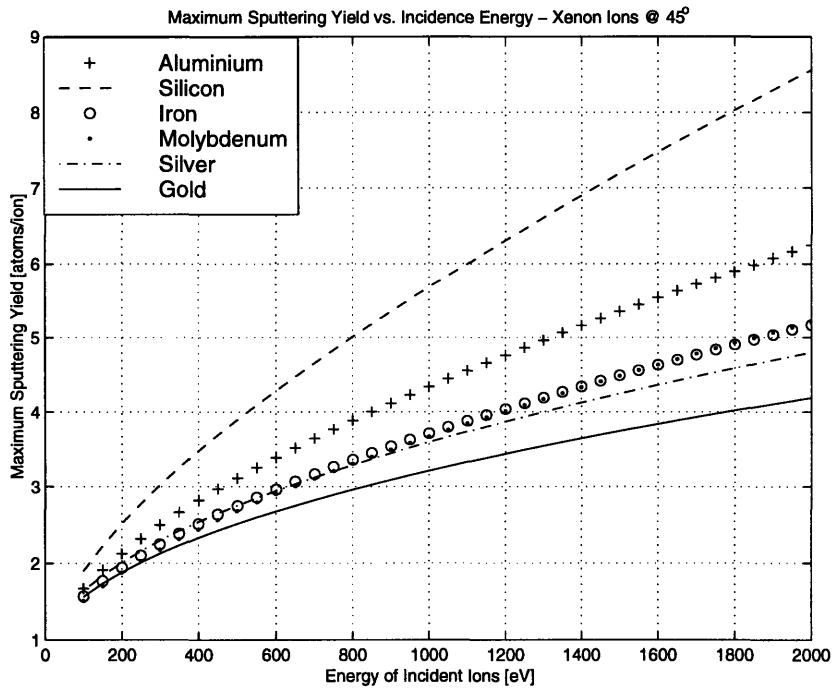**Figure 3.32 Angle of Maximum Sputtering Yield vs. Impinging Ion Incident Energy**

Figure 3.33 Maximum Sputtering Yield vs. Impinging Ion Incident Energy

43

For the spacecraft configuration used in this work (described in the next chapter), Figure 3.34 shows that the average angle of incidence for xenon neutrals and ions on the spacecraft surfaces is approximately 49°. While spacecraft designers are concerned about ions in the 0eV - 400eV range, Figure 3.32 shows that for this particular energy range the maximum sputtering yield occurs in the range 60°- 70°. On the other hand, the histogram below shows that a small fraction of particles in the simulation hit surfaces at an angle in this range. The majority of particles impinge on surfaces with an angle less than 65°. These particles are responsible for most of the damage on the model solar array. The sputtering yield curves in Appendix B show that in the angular range considered the sputtering yield is higher than when particles impinge normally on a surface. Thus, since most of the particles impinge on the spacecraft at non-normal incidence Oh's surface erosion model based on normally incident particle data under predicts the sputtering rates for silver, silicon and quartz..
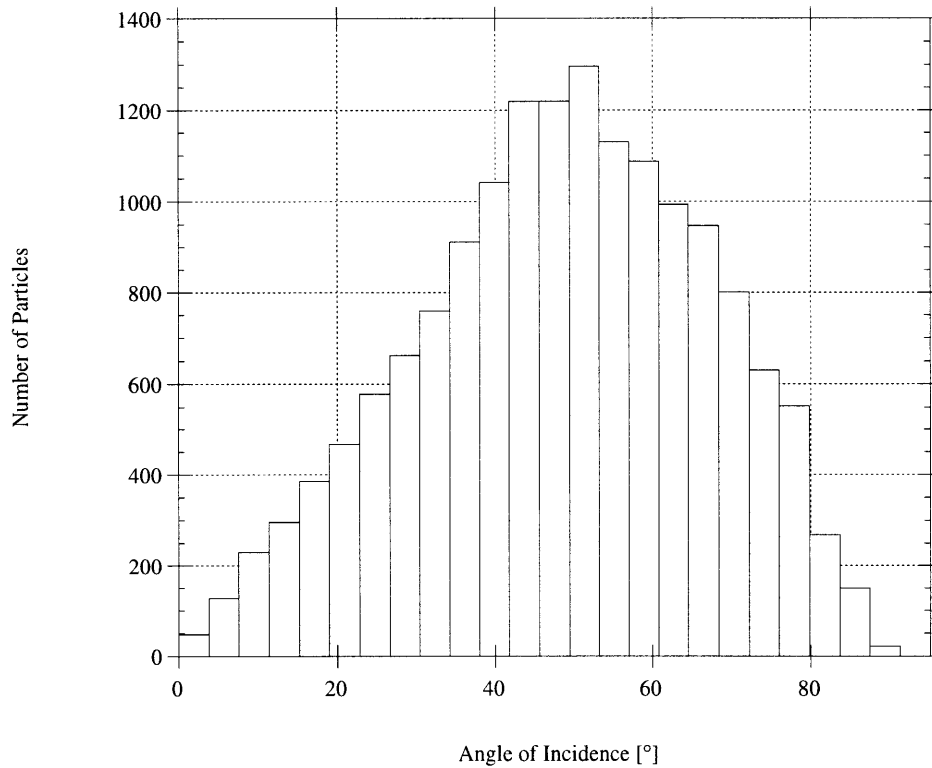
Figure 3.34   **Distribution of Angle of Incidence on all Spacecraft Surfaces - Primarily Solar Array**

44

Chapter 4

Computational Model

4.1 Introduction

A Hybrid-PIC model has been developed at MIT by Fife to simulate the plasma dynamics in the acceleration channel of a Hall Thruster. This model simulates only the heavy species, ions and neutrals, as opposed to a standard PIC code in which both ions and electrons are simulated. In the 'hybrid-PIC' code electron motion is described by integrating the fluid equations of motion. Prior to this development Oh implemented a PIC-DSMC algorithm which tracked plasma behavior and included collisions starting from the exit plane - outside the acceleration channel. Since both models assume that the plasma is quasi-neutral the Poisson equation cannot be used to solve for the plasma potential. Simply inverting the Boltzmann equation to calculate the potential makes this code/model computationally more efficient. This might lead to some inaccuracies as the electron temperature is assumed constant (T_e~3.4eV).

However, in order to perform a complete Hall Thruster simulation - acceleration channel through the exterior - the two models still need to be fully integrated. For purposes of this research effort, Fife's code produced the exit plane particle distribution which was averaged and 'fed' into Oh's code. Oh's model had assumed an exit plane distribution based on empirical data. Developing a scheme that does this efficiently at one pass is of key importance. The Fife-Oh semi-integrated model has been used to simulate plasma expanding from an SPT - 100 into a vacuum tank. This model is referred to as 'semi-integrated' as at the moment in order to incorporate Fife's outputs, it is necessary to sample and reconstruct the ion current density and beam divergence angle distributions at the exit

plane [of Fife's thruster model]. A least squares fit is performed on the output data yielding a 3rd and 4th order polynomial fit for the ion current density and the beam divergence angle respectively.

In his work, Oh developed an axisymmetric two-dimensional plume model as well as a three-dimensional model based on the same PIC-DSMC algorithm. However, since spacecraft are rarely axisymmetric the three-dimensional model was used for purposes of this work. In this chapter the basic assumptions of the model are highlighted while a detailed description of the hybrid (PIC-DSMC) method as well as its implementation can be found in Oh's Doctorate Thesis - Computational Modeling of Expanding Plasma Plumes in Space Using a PIC-DSMC Algorithm. In his work, Oh discusses at length the underlying theory, the limitations as well as the implementation of the method on workstation-type machines.

4.2 The Background Environment

Experiments in the ground-based facilities are performed with a finite amount of gas present in the background. i.e. an ideal vacuum is not achieved as a result of pumping limitations. The density of the background gas, though lower than then density of neutrals near the exit plane of the thruster, must be included in the simulation as the densities are comparable in the far plume. The presence of the background gas is simulated by adding xenon neutral particles along the boundaries with the ambient plasma. The background ion temperature is assumed to be 300 K and the background neutral density was calculated using the ideal gas law [*Oh*, 1997].

Pressure	Number Density
2.2×10^{-6} Torr	$7.085 \times 10^{16}\,\mathrm{m}^{-3}$
5.6×10^{-6} Torr	$1.803 \times 10^{16}\,\mathrm{m}^{-3}$
2.5×10^{-5} Torr	$8.050 \times 10^{16}\,\mathrm{m}^{-3}$
6.3×10^{-5} Torr	$2.029 \times 10^{18}\,\mathrm{m}^{-3}$

Table 4.1: Simulated Pressures and Background Neutral Densities

Note: When simulating the spacecraft in geostationary orbit, the background pressure is set to zero.

4.3 Modeling The Hall Thruster Exit Plane

A Hall thruster was chosen for the initial studies due to its maturity and the relatively large data base with which to compare results. One issue associated with HT devices is that complete ionization cannot be achieved with reasonable levels of power, and hence, neutral gas is emitted at thermal speeds. These slow neutrals are of interest because they charge-exchange with the fast beam ions producing fast neutrals and slow ions which can be influenced by local electric fields in the plume. The electric field structure in the plume, as seen in experiments and in computational models, is radial, and hence the slow ions are pushed out of the beam and move back towards the spacecraft.

Hall thrusters are also known to have a rich spectrum of oscillatory behavior that is believed to be critical to their operation, however, Oh did not include these unsteady oscillations in his model. Instead, the thruster is modeled as a steady source within the domain of the simulation and at each time step, new particles are loaded to represent the flow of neutrals and ions from an SPT-100's exit plane.

In Oh's model exit plane distributions were empirical and based on curve fits to experimental data - Figure 4.2 - Figure 4.4. The ion current density and beam divergence angle data (both as a function of thruster exit radius) were taken from SPT-70 data and normalized to represent an SPT-100. This normalization introduced a slight skewness in the distribution as mentioned by Qarnain. Thus Oh's source was based upon one set of data [*Gavryushin*, 1981] 4mm away from the thruster exit plane. This set was questionable as the originally published results did not have error bars (see Figure 4.3 and Figure 4.4) Also the asymmetric distribution might have suggested that Gavryushin's test thruster was damaged. More importantly, distributions can be expected to depend on operating conditions in some complex way.

In this work Fife's hybrid-PIC code was used instead to simulate the SPT-100 exit plane ion current density and beam divergence angle distributions. These functions consist of an ion current probability distribution function and beam divergence angle probability functions. Qarnain quantified the sensitivity of the plume model to variations in source input and concluded that variations in the probability distribution functions do not substantially affect the output of the plume model [*Qarnain*, 1998]. Fife's source distribution (see Figure 4.3 and Figure 4.4)which showed good agreement with experimental data was

used for purposes of this work. There was a slight shift in the data but that was because two slightly different thruster geometries [different channel widths] were used to generate the distribution functions [*Qarnain,* 1998].
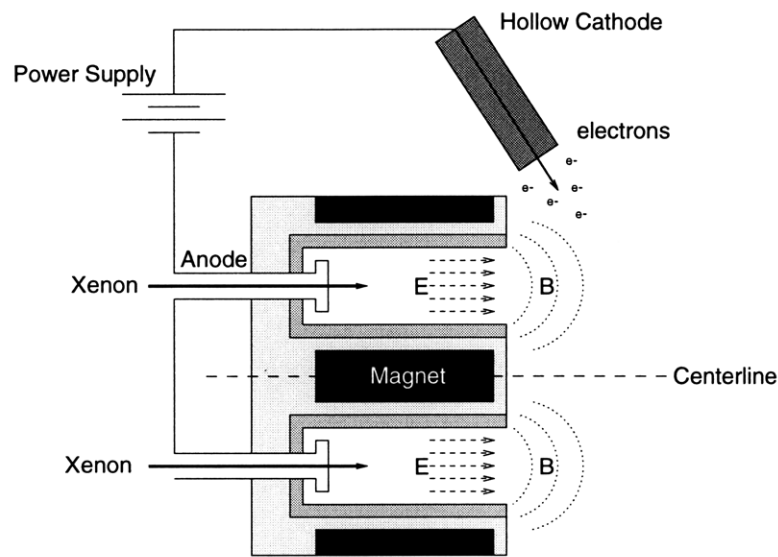
.

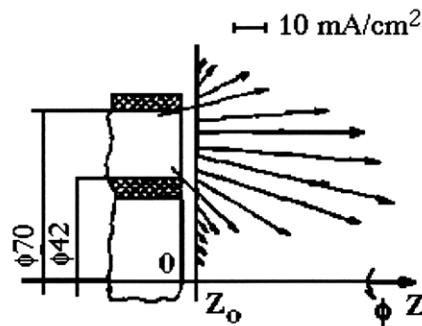**Figure 4.1   Cross Section of SPT-100 Model**

Figure 4.2   Experimental Measurements of Near Field Current Density [Absalamov, 1992 and Gavryushin, 1981]
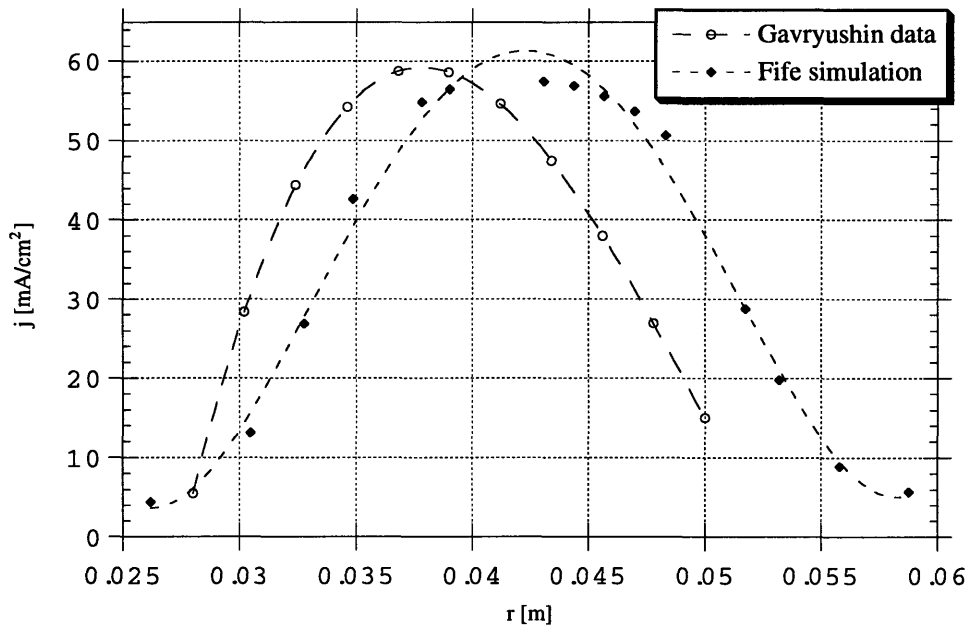
Figure 4.3   Comparison of Fife and Gavryushin Ion Current Distribution 4mm from Thruster Exit
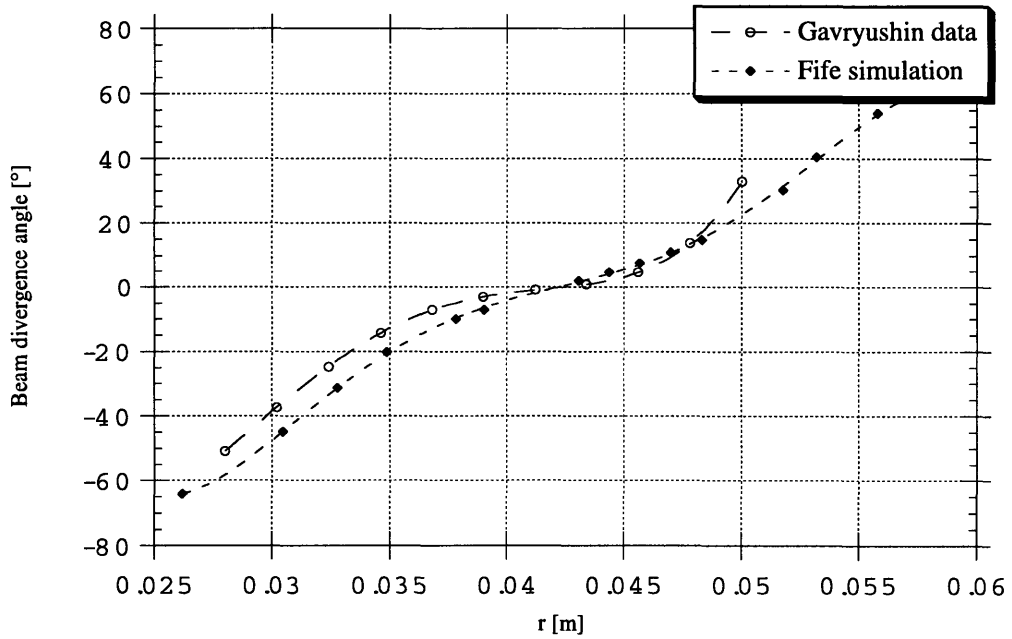**[*Qarnain*, 1998]**

Figure 4.4   Comparison of Fife and Gavryushin beam Divergence Angle Distributions 4mm from
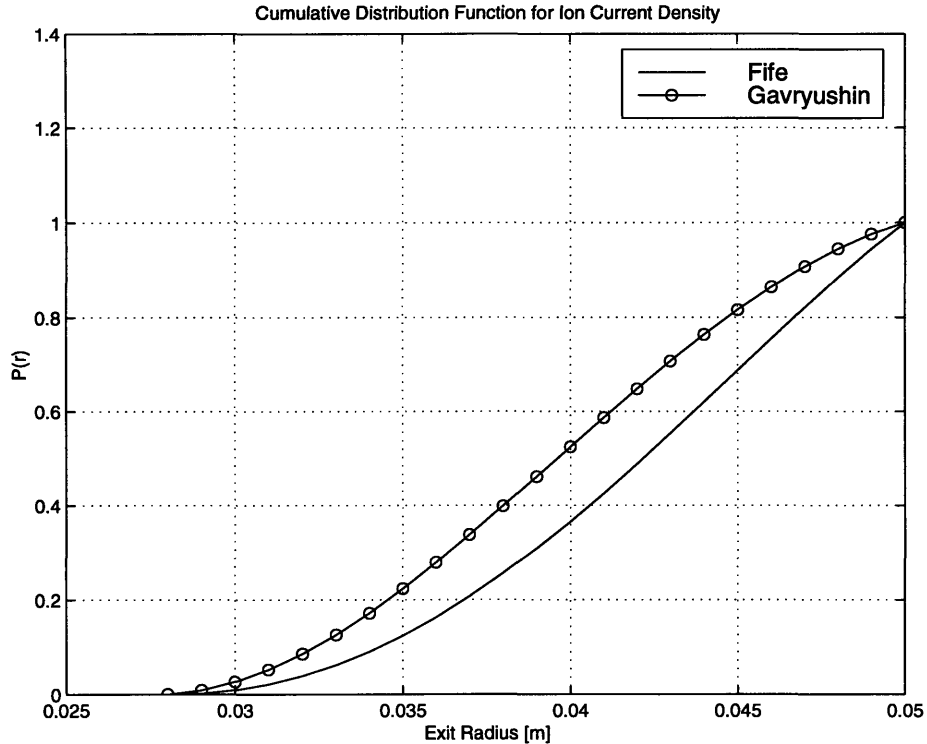**Thruster Exit [*Qarnain*, 1998]**

Figure 4.5 Cumulative Distribution Function for Ion Current Density

4.4 Modeling The Plume

Since a Hall thruster plume is an unmagnetized, quasi-neutral plasma in which both Coulomb forces and CEX collisions have an impact on the development of the flow, neither a PIC method nor a DSMC method alone can be used to simulate these plumes. A PIC method cannot model the collisional effects but is capable of modeling the long range Coulomb forces, whereas a DSMC can be used to model collisional effects in the plasma. It cannot, however, be used to model the charged particles present in the plasma. Oh combined these two methods in his work, and produced a hybrid computational method capable of modeling collisional non-Maxwellian plasmas interacting with neutral gases. Two important differences between the hybrid PIC-DSMC method and the PIC method are:

- the potential is determined using the electron momentum equation and not solving Poisson's equation.

- a collisional routine is included to modify the trajectories of the particles in the plasma.

Simply inverting the Boltzmann equation to calculate the potential makes this code/ model computationally more efficient.

4.4.1 Collisions

The charge exchange (CEX) and elastic collisions which were modeled by Oh in the PIC-DSMC simulations are discussed in the following sections. Coulomb collisions have relatively large Coulomb cross sections and the collision dynamics are primarily dominated by small angle collisions. These interactions have a relatively long mean free path through the plume and thus can be reasonably omitted. For detailed calculations of each of these cross section refer to [*Oh*, 1997]. It must be noted that the estimated error in the CEX cross sections use in the model is 20% [*Hasted*, 1964].

Collision	Type of Collision	Collision Cross Section
Xe - Xe$^+$	CEX	$_{EX} = (0.88\ln(c_r) + 15.13)^2 \cdot 10^{\cdot} \ m^2$
Xe - Xe^{++}	CEX	$\sigma_{CEX} = (3.41 \cdot 10^{-9} - (2.7 \cdot 10^{-10}\ln c_r))^2 \ m^2$
Xe -Xe	Elastic	$\sigma_E = (2.12 \cdot 10^{-18} c_r^{-0.24}) \ m^2$
Xe - Xe$^+$	Elastic	$\sigma_E = (8.28 \cdot 10^{-16}/c_r) \ m^2$
Xe - Xe^{++}	Elastic	$\sigma_E = 2 \cdot (8.28 \cdot 10^{-16}/c_r) \ m^2$

Table 4.2: Collision Cross Sections assumed in PIC-DSMC Model

Charge Exchange Collisions

One issue associated with HT devices is that complete ionization cannot be achieved with reasonable levels of power, and hence, neutral gas is emitted at thermal speeds. These slow neutrals are of interest because they charge-exchange with the fast beam ions producing fast neutrals and slow ions which can be influenced by local electric fields in the plume. The electric field structure in the plume, as seen in experiments and in computational models, is radial, and hence the slow ions are pushed out of the beam and move back towards the spacecraft.

In the PIC-DSMC algorithm, Oh used the collision cross-sections based on theory or experiment. For Xenon neutral-Xenon single ion CEX collisions the cross-section calculated by *Rapp and Francis* [1962] was used whereas the cross section for Xe-Xe^{++} CEX collisions were determined by *Hasted* [1964]. It was shown that the collision cross section

for Xe^+-Xe^{++} CEX collisions was an order of magnitude smaller than that for Xe-Xe^+ CEX cross section - this led to the exclusion of this type of collision.

Ion-Neutral Elastic Collisions

Elastic collisions between species are also included in the simulation. Xe-Xe^+ and Xe-Xe^{++} collision cross sections, calculated by *Banks* [1966], are of a Maxwellian Collision type where each collision frequency is not dependent on velocity. Also, as shown by *Dalgarno* in 1958, the Xe-Xe^{++} elastic cross section is twice that of the Xe-Xe^+ cross section.

Neutral-Neutral Elastic Collisions

Oh also included xenon neutral - xenon neutral collisions to allow the simulation of situations where thrusters have a high neutral flow rate. Such collisions have been studied extensively and numerous models have been proposed, but the model assumed in this simulation is the variable soft sphere model as it has the most degrees of freedom.

4.5 Modeling the Surface Interactions

Experiments have shown that the plume of an SPT-100 contains traces of ceramic (Boron Nitride from the channel wall), boron and nitrogen, but these materials are inert and experiments have shown no evidence of deposition on surfaces exposed to the plume [*Randolph,* 1994]. Possible deposition of these substances onto any solid boundaries (tank walls or spacecraft surfaces) was ignored in the original model [*Oh,* 1997]. In this work the same assumption is made.

When particles such as xenon neutrals and ions (Xe^+ and Xe^{++}) hit surfaces they undergo numerous phenomena depending on a number of conditions described in Section 3.2. Particles can be backscattered, they can come to thermal equilibrium and evaporate at the surface, cause secondary electron emission, cause radiation damage or remove particles from the target material's surface (sputtering). In Oh's model, however, the ions were neutralized and removed from the simulation whereas neutrals were reflected specularly back into the domain. Also erosion rates were calculated based on empirical data for sputtering at normal incidence.

Qarnain improved upon Oh's model and included the angular dependence of sputtering yield by introducing an angular dependence coefficient as a multiplier to the normal sputtering yield. However, this factor was based on high energy ion data (30 keV), which may have over-estimated the angular dependence, as seen from the results presented in Appendix A. This coefficient, derived by Yamamura *et al.*, was discussed in Section 3.3. Qarnain found that the model gave 'believable' results for xenon ions with energy above 50eV sputtering silver and above 200eV sputtering silicon [*Qarnain*, 1998].

In this work, the surface interaction model developed by Oh and Qarnain has been improved upon. Xenon ions are no longer removed from the simulation when they hit an object boundary but instead they are neutralized and reflected specularly, except for a 20% energy loss. In order to accommodate these new particles, it must be noted that approximately 30% more memory is needed when running each simulation. Also the time for each simulation is increase by about 50% to 70%. In real-time this translates to 2 to 4 days of computational time (on a workstation with R8000 75MHz Processor), depending on the number of particles used.

In the surface interaction model the following assumptions have been made:

- energetic neutrals and ions are responsible for erosion of surfaces

- xenon ions hitting any 'hard' boundary (e.g. tank walls or spacecraft surfaces) are neutralized at the boundary as it is improbable that the ions retain their charge after interacting with the surface atoms

- the energy of reflected particles is 80% of their incident energy. In this work, this value is an initial guess.

- it is improbable that [target] atoms sputtered off of the tank walls will collide with neutrals or ions in the plasma as the mean free path is large (e.g. 20-30m)

- in reality sputtered material is ejected from surfaces as a function of energy but for purposes of this work this is assumed constant at 10 eV since what matters in this case is where this sputtered material is deposited.

- the ejection angle of the sputtered material is assumed to be 45° for all ejected material, as it was difficult to implement Equation 3.1 derived by Yamamura in 1981, and discussed in Section 3.1 .

4.6 The Tank Geometry

The ground-based simulation includes a Hall thruster mounted on a 'thrust stand' in a generic rectangular vacuum tank. The tank is comprised of six walls (2.63 m by 3.68 m by 2.63 m) and a pumping orifice (to evacuate the background gas during the simulation run-time). As shown in the figure below the 1.15 m x 1.15 m thrust stand is approximately 0.4 m (in the x-direction) away from the pumping orifice.
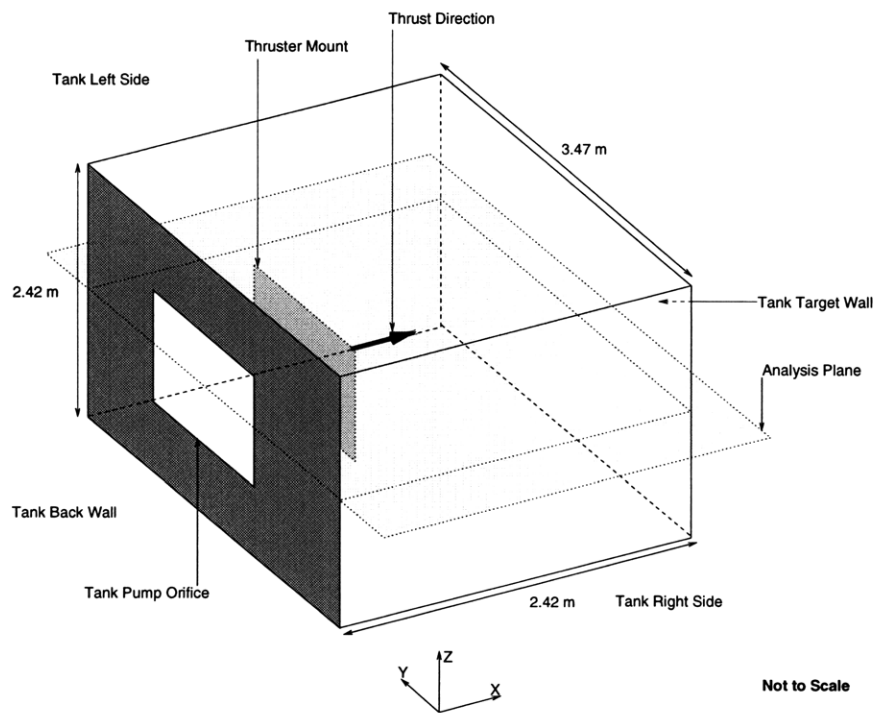

Figure 4.6   Vacuum Tank Configuration. Includes Thrust Stand and Pumping Orifice

It must be noted that the outer walls are not shaded in order to allow visualizing the interior setup of the tank.

4.7 The Spacecraft Geometry

The 'space' study was conducted on a generic spacecraft (based on a geostationary communications satellite) configuration as shown in Figure 4.7 below. This configuration was chosen for the following reason. Oh studied the effect of an expanding plume on an array with its base 1.9 m away from the thruster exit plane and almost entirely immersed in the plume. In this work the "array" is placed closer to the exit plane but parallel to the

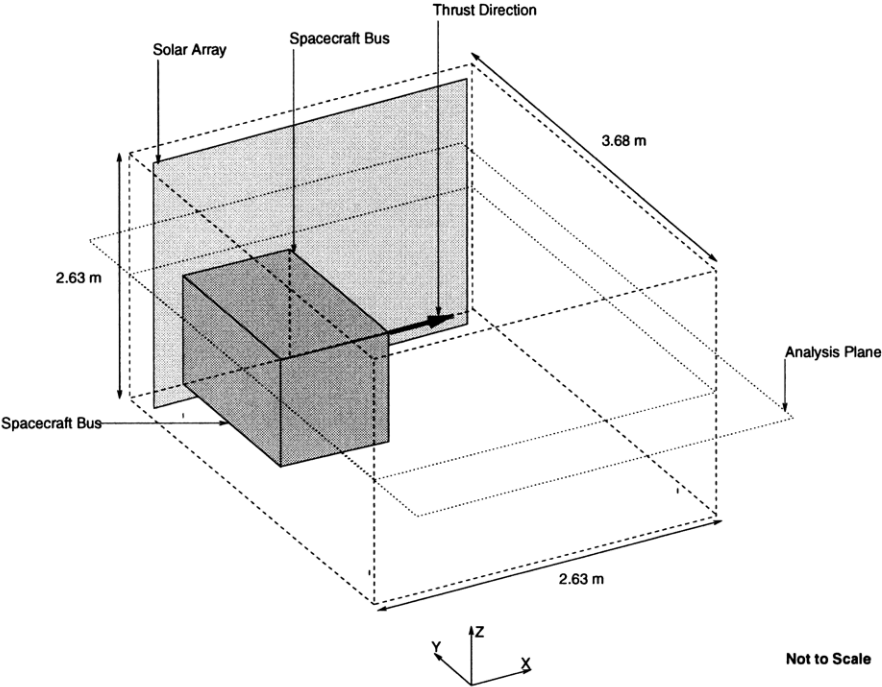thrust axis as it is believe that most of the damage caused by CEX ions occurs near the thruster exit.

Figure 4.7 Spacecraft Baseline Configuration. Includes Bus, Solar Array and Protective Shields

Chapter 5

Results

5.1 Introduction

An enhanced three dimensional PIC-DSMC based model of a Hall thruster's plasma plume expanding into vacuum has been developed by Oh. The main benefit of developing such a three dimensional simulation is that it can be used to model more realistic spacecraft geometries in a short amount of time and at a lower cost. Some of the applications that spacecraft designers are interested when designing space missions include, north-south stationkeeping on geostationary satellites, long duration orbital transfers and orbit raising.

Even though numerical tests check the consistency of a simulation, an experimental comparison is needed to verify that the computational model accurately represents reality. Since a variety of experiments mapping out the plume region of an HT have been conducted by the scientific community, it is easy to verify the code against existing experimental data. Oh [1997] performed these checks and studied the sensitivity of the model to axial ion temperature whereas Qarnain [1998] analyzed the sensitivity to the source model. Oh found out that increasing the ion temperature improves the match between the simulation and experimental measurements. Oh found that if the ion temperature is high the beam is more diffuse, and when the ion temperature is low, the beam is more focused. This change can be seen in the number of CEX ions hitting the side wall of the tank. More diffuse beams tend to have a lower number of CEX ions produced and thus the dumbbell shape discussed is less pronounced.

The following operating conditions for the thruster have been assumed in the simulations: a current of 4.5 A, 300 V discharge voltage, total flow rate of 5.37 mg/s (7.1% flows through cathode), efficiency of 49.7% and a facility back pressure of 2.2 x 10^{-6} $Torr$. This pressure corresponds to that under which Manzella [1993] operated. **Note:** For simulations in the space environment a 0 $Torr$ background pressure has been assumed.

The dimensions of the simulation domain are 2.63 m x 3.68 m x 2.63 m discretized into 25 x 35 x 25 cells in the x, y, and z directions respectively where each grid cell is 0.105 m on each side. This domain size provides the plume with enough space to expand and develop fully. All simulations were run for 5000 to 15000 iterations with a time step of 0.1 normalized units (each timestep is 1.73 x 10^{-6} s in duration) and took 20 to 40 hours on a workstation (256 megabytes of memory and R8000 75MHz Processor).

The results for the ground-based simulation which includes a Hall thruster mounted on a 'thrust stand' in a generic rectangular vacuum tank are presented in this section. The imaginary plane shown in Figure 4.6 was used to traverse, study and map out the plume properties as well as particle distributions in the backflow region. In the next section the simulations (without shields) are discussed. This is followed by a discussion comparing results of simulations which involve a protective shield, the length of which was varied. In the tank simulation the key comparative metrics will be the Xenon ion flux and energy distribution on the left side wall whereas in the space simulation, the ion flux, energy and erosion rates on the solar array will be used.

5.2 The Tank Simulation

5.2.1 Species Distribution in Hall Thruster Plume

As expected most of the ions are concentrated along the centerline of the plume and move in the direction of the thrust vector. In order to explain the expanding nature of the plume one must look closely at the ion distribution in the region. As the potential falls off with density, an electric field whose radial magnitude initially rises then falls of with distance from the centerline, is created locally. This electric field accelerates ions in the radial direction (away from the centerline), explaining the shape of the plume.

58

The current density 0.5m away from the thruster's exit plane shows similar trends to the current density experimentally measured by King and computationally determined by VanGilder *et al.* [1999] Between 15° and 40° off the centerline, there is fairly good agreement between the simulation and King's data but near the centerline the PIC-DSMC model predicts a current 4 times greater than data indicate for the same thruster.
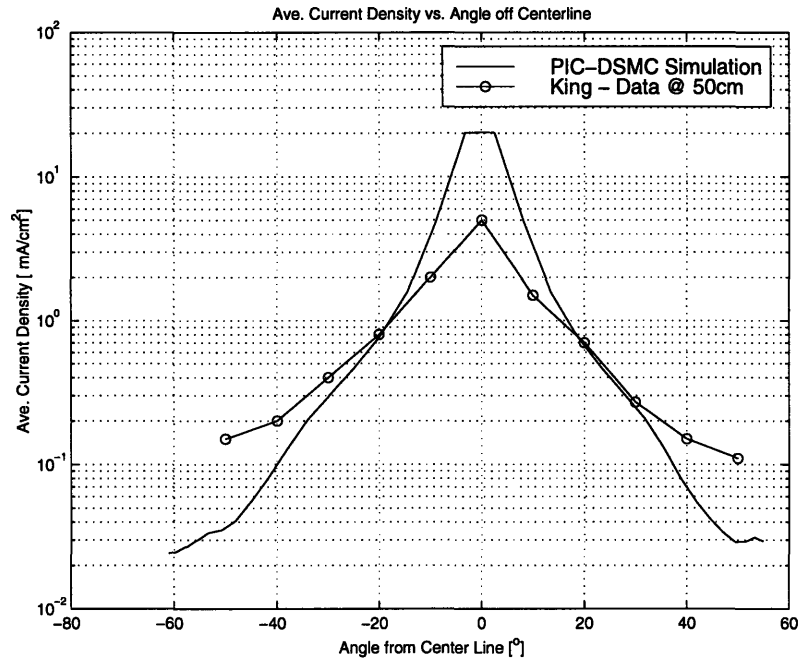

Figure 5.1   Current Density Distribution 1 m from Thruster Exit Plane Compared to King's Data.

The facility background pressure was set initially to 2.2 x 10^{-6} *Torr*, corresponding to a neutral density of 7.085 x 10^{16} m^{-3}. During the simulation's run-time the SPT-100 thruster adds neutrals to the domain while neutrals escape through the pumping orifice. At the end of each tank simulation (10,000 iterations) the average neutral density in the tank was approximately 5.5 x 10^{16} m^{-3}. Neutral densities have been measured by King using a retarding pressure sensor 0.5 m from the thruster exit plane and they show that the flux varied from 1 x 10^{20} to 1 x 10^{22} m^{-2} sec^{-2} [*King*, 1996]. Assuming a neutral thermal velocity of 350 m/s the number density 0.5 m away from the exit plane averages at 3 x 10^{17} m^{-3}. This value is approximately 5.5 times higher than the density obtained in the PIC-DSMC simulation and an explanation could be that King's pumping speed was approximately 5.5 times lower than that implied in this work.

The neutrals appear to be evenly distributed throughout the tank. However, when comparing the neutral flux on the bottom and top wall of the tank an interesting point is revealed (compare Figure 5.3and Figure 5.4). The neutral distribution is slightly skewed towards the bottom of the tank. This is a result of the hollow cathode, located directly above the thruster, introducing neutrals at an angle beyond the exit plane. These neutrals are primarily directed towards the bottom wall of the tank.

When referring to the figures shown in the next couple of sections, the thruster position must be noted. The thruster is located approximately 1.7 m away from the wall with its centerline parallel to and in the same plane as the wall and array centerlines. The thruster plume expand from the left to the right in all cases.

It is interesting to note the dumbbell shaped ion (Xe^+ and Xe^{++}) flux distribution on the left wall of the vacuum tank. This shape is a result of the radially moving CEX ions originating primarily near the exit plane of the thruster. Unlike the primary beam ions the CEX ions tend to follow curved paths away from the plume centerline as the CEX ions have a smaller turning radius and are influenced easily by electric fields.
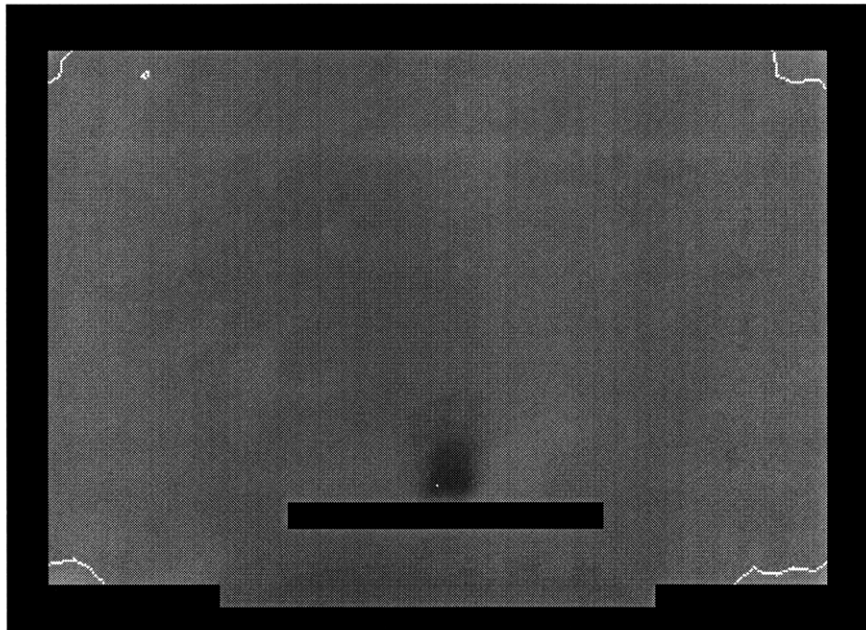

Figure 5.2   Neutral Density in Plane Dissecting Tank [approx. 5.5×10^{16} m^{-3}] after 10,000 Iterations

The two lobes of the dumbbell structure are caused by the CEX ions on the left of the array/wall and the primary beam ions form the lobe on the far right.
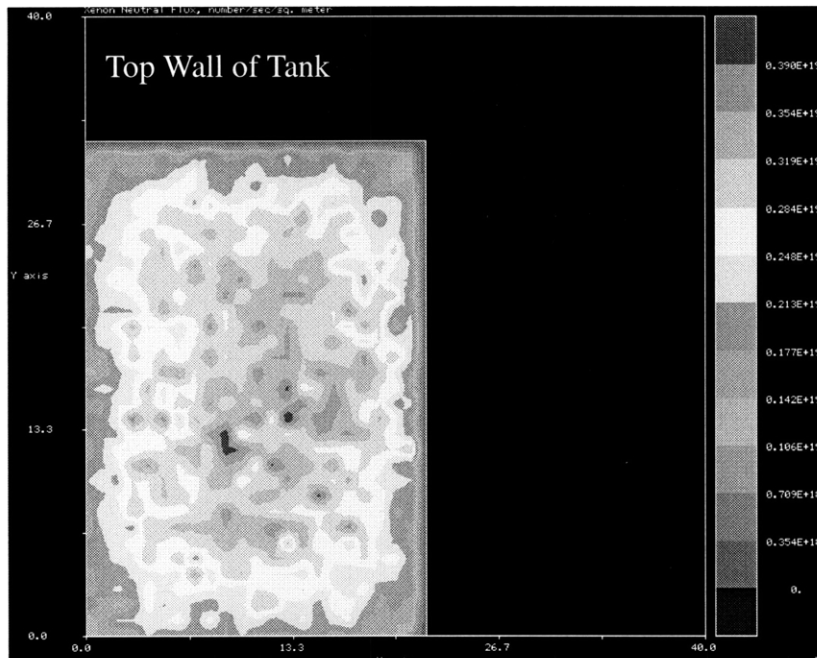
60

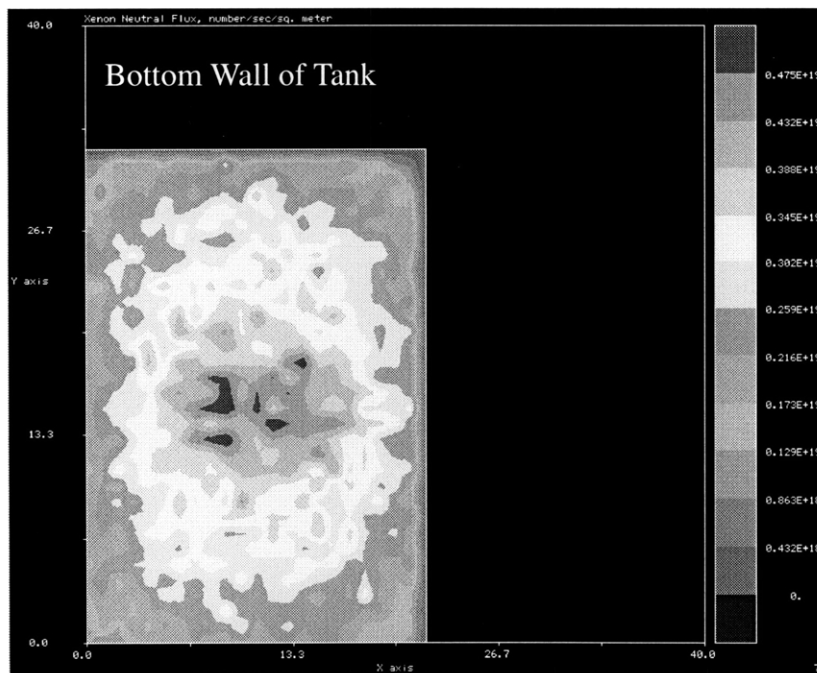**Figure 5.3 Xenon Neutral Flux on Top Wall of Tank**

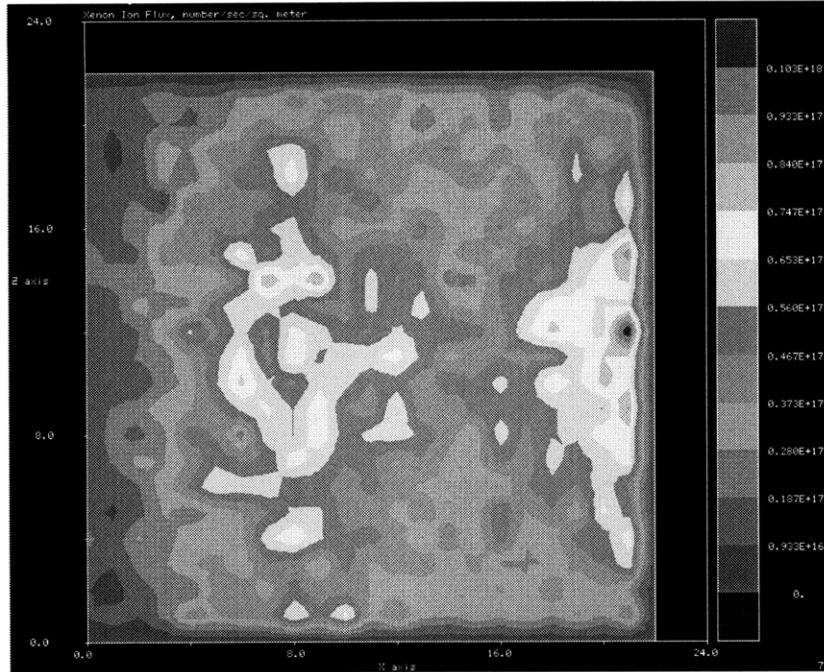**Figure 5.4 Xenon Neutral Flux on Bottom Wall of Tank**

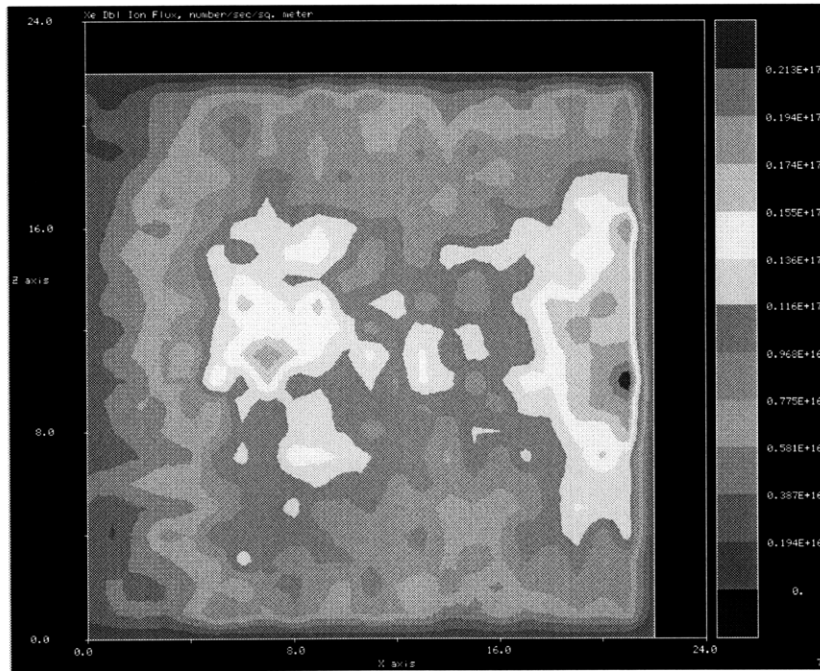**Figure 5.5 Xenon Ion (Xe$^+$) Flux on Left Wall of Tank**

Figure 5.6 Xenon Ion (Xe++) Flux on Left Wall of Tank

The domain size was chosen so as to emulate the realistic dimensions of an average sized test facility. In order to maintain a desired background pressure of 2.2 x 10^{-6} *Torr*, a 1.4 m^2 pumping orifice was placed at one end of the tank (behind the thrust stand). This maintained a constant pumping speed of approximately 140 m^3/s.

Each iteration time step in the simulation represents 1.73 x 10^{-6} *s* of thruster operation, thus in 10,000 iterations a total operational time of 0.0173 *s* has elapsed. When steady state is achieved, the number of particles in the simulation domain should remain constant. i.e. the rate at which particles are introduced into the domain by the thruster should be equal to the rate at which they are removed by the pump. However, Figure 5.7 indicates that, up to 10,000 steps at least, the number of particles decreases with each time step.
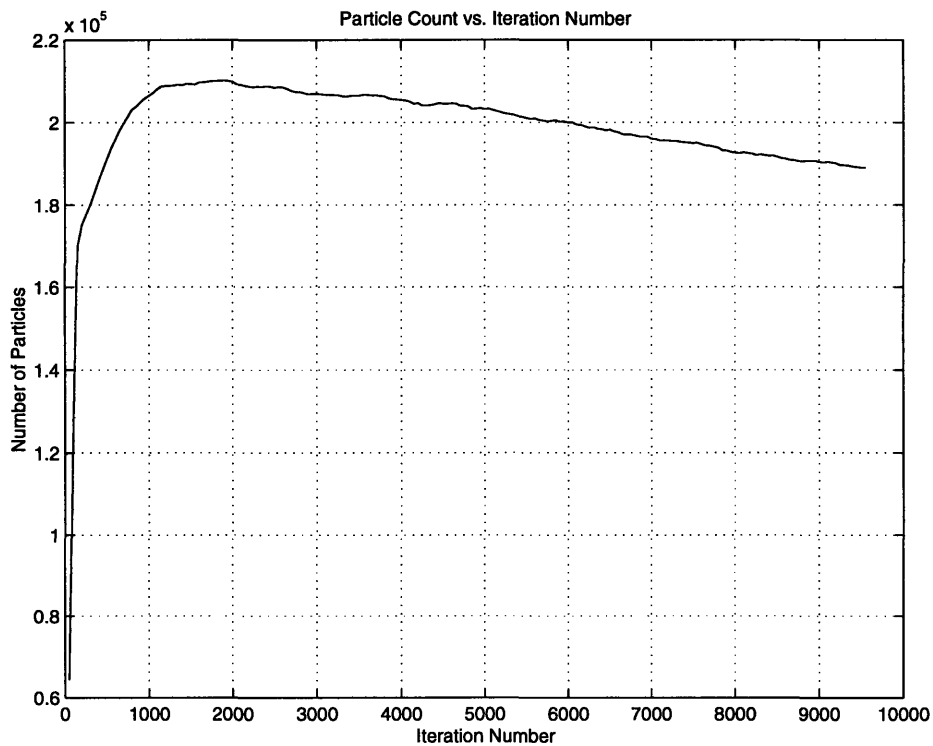

Figure 5.7   Total Particle Count vs. Iteration Number

This indicates that steady state conditions have not been achieved after 10,000 iterations and at this point in time it is unsure whether a longer run will achieve an equilibrium state. It is suggested, however, that (using this algorithm) run times 3 to 5 times as long should be tried in future work. The neutral density shown in Figure 5.2 implies that spatial

uniformity has been achieved since the distribution of neutrals appears to be fairly even. This can be explained by the fact that after 10,000 iterations, the neutrals have had enough time to travel throughout the domain, but have not had enough time to reach their limiting (constant) density.

5.3 Simulation of the Effects of a Plume Shield

The results for the space-based simulation which includes a Hall thruster mounted on a generic spacecraft are presented in this section. In his work, Oh studied the effect of the plume on an array with its base placed 1.9 m away from the thruster exit plane and almost entirely immersed in the plume. In this work the array is placed closer to exit plane and the thruster centerline as it is believed that most of the damage due to CEX ions occurs near the thruster exit plane.

In order to protect the spacecraft subsystems from the destructive effects of the plasma plume, the use of protective shields around the thruster exit has been proposed. The purpose of this shield is to prevent the energetic CEX ions created in the near plume from ever reaching the spacecraft subsystems. Thus the effect of extending a protective shield of diameter, 0.3 m, from 0.0 m to 0.3 m beyond the thruster exit plane has been studied. **Note**: The solar array is placed approximately 1.7 m away from the plume centerline in all simulations and all results are compared to the baseline configuration (i.e. with no shield). Figure 5.8 shows the important dimensions used.
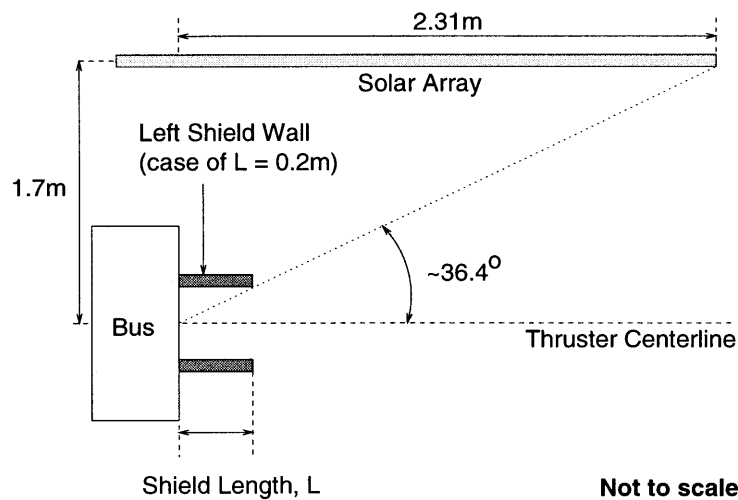
Figure 5.8 Sketch Showing Important Dimensions Used in Shield Study

5.4 The Effect of Protective Shields

The current density, the ion flux distribution, energy of impinging ions and the erosion rates were used to assess and compare the damage on the spacecraft's solar array. For the chosen configuration, it has been observed that a shield is effective in protecting the solar array from ion impacts, but may lead to problems related to the deposition of material sputtered from the shield itself. As can be seen in the following figures (Figure 5.9- Figure 5.32), all key ion-related metrics show a decrease in magnitude for a shield length above 0.2 m. From Figure 5.8, when L > 0. 2 m, there is no direct line of sight to the panel from the center of the thruster exit plane. Thus, longer shield limit CEX flux to that arising progressively farther and farther into the plume, which explain the decrease.

As in the case of the tank simulations, it is interesting to note the dumbbell shaped ion (Xe^+ and Xe^{++}) flux distribution on the solar array in the case without the shield (see next section). This distribution is produced by the radially moving CEX ions originating primarily near the exit plane of the thruster. Unlike the primary beam ions the CEX ions tend to follow curved paths away from the plume centerline as the CEX ions have a smaller turning radius and are influenced easily by electric fields.

65

When the shield is mounted and its length is increased to 0.2 m, the slow moving CEX ions are prevented from reaching the solar array and the dumbbell shape is gradually diffused. A shield of length 0.3 m, seems to pronounce the dumbbell shape, however, the overall magnitude of the distributions decrease substantially.

In order to assess the damage on the solar array, it is necessary to know how the shields affect the erosion of material off the arrays. The plot below shows silver, silicon and quartz erosion rates on the array as a function of shield length. The erosion rate increases slightly as the shield length is increased from 0 to 0.1 m and then drops off substantially for shield lengths greater than 0.2 m. The slight increase below 0.1 m can be attributed to the fact that the shield focuses the beam, thus increasing the charge density as well as neutral density along the centerline. This increase in neutral and ion densities leads to a higher frequency of CEX collisions in the near field tending to produce more CEX ions (Xe^+ and Xe^{++}) which travel in the direction of the spacecraft bus. This explains the more pronounced dumbbell shape in the Xe^+, and the Xe^{++} flux distributions on the portion of the solar array closest to the thruster exit plane. However, if the shield is long enough (> 0.1 m), this additional flux is intercepted anyway, and the net received at the array decreases.

Even though keeping the erosion rate on the solar array low is of prime importance, one has to consider the erosion rate of the shield itself. In Figure 5.40, the erosion rate on the left wall of the protective shield is plotted as a function of shield length. Although the plots are for silver, silicon and quartz as these were the baseline materials implemented in Oh's code, the increase in erosion rates as a function of shield length is very apparent.

The thickness of the shield will be a critical parameter in the design of an optimum shield. Ideally the lifetime of a typical thruster on a geostationary satellite should be of the order of 8000hrs. This is approximately 11 months of continuous thrust time. As seen in Figure 5.39, the average erosion rate for silver is 500 microns per month when a 0.2 m shield is chosen. Molybdenum (density = 10.22 g/cm^3) is chosen for a preliminary sizing of the protective shield as its sputtering yield is about 13 times lower than silver and it is also cheaper. Assuming the shield is concentric with the thruster's centerline its major dimensions are a 15 cm diameter, 0.12 cm in thickness (assuming a safety factor of 3), and 25 cm in length, it will weigh approximately 1.44 kg. **Note:** If a similar shield were built of

aluminum, which has a density of $2.702 g/cm^3$, it would be approximately 4 times lighter than a molybdenum shield. Yet, the sputtering yields (as a function of incident energy and angle) of molybdenum and aluminum are very similar as shown by the theoretical results (see Appendix B) based on Matsunami's and Yamamura's theories (Chapter 3).

The geometry and position of the shield could also be important. In this work, for example, a shield half the proposed diameter could have been used to protect the solar array from damage. For any given thruster geometry, if spacecraft designers have a better understanding of the expanding plume and its ion distributions, they could design shields which preferentially protect the spacecraft, thus reducing overall mass. Possible shield geometries could include flat plates or semi-concentric structures. For the configuration used in this work, if a flat plate is used, its position from the thruster's centerline could be varied. If it is placed closer to the centerline, it is possible that a smaller shield would be necessary to protect the solar array.

5.5 Deposition of Shield Material on Solar Array

When designing protective shields, spacecraft engineers must bear in mind that sputtered shield material could redeposit itself onto critical spacecraft components. It is the goal of this section to explore and understand the effect of shield length on the deposition of shield material on the model solar array.

In this work, aluminum was used for the baseline shield design, and the redeposition of aluminum on the solar array is presented. The simulations were run for shield lengths of $0.1\ m$ - $0.3\ m$, all other dimensions being constant. The series of figures, Figure 5.41 - Figure 5.50, shows the results for the redeposition of aluminum on the modeled solar array. The last three figures in particular, illustrate an interesting non-intuitive point. The sputtering model in this work assumed the sputtered material is ejected from surfaces at 45° and thus it was expected that the shield material would be sputtered at 45° from the thruster centerline. The figures, however, indicate otherwise. When the shield is longer than $0.2\ m$, it is eroded in the region closer to the thruster exit plane and the sputtered material is primarily deposited at the shield's lip.

The study also shows that shields shorter than 0.2 m do not only exacerbate the damage on the solar array due to CEX ions but also have a negative effect as aluminum sputtered from the shield of length 0.1 m is deposited on the middle part of the solar array (Figure 5.41). Thus one can easily conclude that in order to completely protect spacecraft subcomponents in the backflow region, the longest possible shield should be employed. This, however, needs to be traded off against a shields weight, volume and cost.

5.6 Plume Structure

Figure 5.44 to Figure 5.47 show the plume structure when a protective shield is used. The plume tends to be less diffuse with an increase in shield length. It is interesting to note that when the shield is 0.30 m long neutrals from the thruster are more directed towards the centerline of the plume leading to an increase in the neutral density two thruster diameters from the exit plane. In fact, the length of the shield (0.30 m) prevents neutrals from reaching the array as defined in this geometry. Thus no values were obtained for the neutral flux and impact energy distributions with a 0.30 m shield.

The increase in neutral density leads to a higher frequency of CEX collisions in the near field tending to produce more CEX ions (Xe^+ and Xe^{++}) which travel in the direction of the spacecraft bus. This explains the more pronounced dumbbell shape in the current density, the Xe^+, and the Xe^{++} flux distributions on the solar array closest to the thruster.

Referring to Figure 5.36 - Figure 5.38, depicting the neutral impact energy distributions, it can be inferred that the energy with which the neutrals hit the middle of the array is higher when the shield is 0.20 m long. This is a result of the increase in plume density about 2 thruster diameters away from the exit plane, which builds up a higher plume potential. This higher potential subsequently imparts a greater amount of energy to the CEX ions heading in the direction of the array.

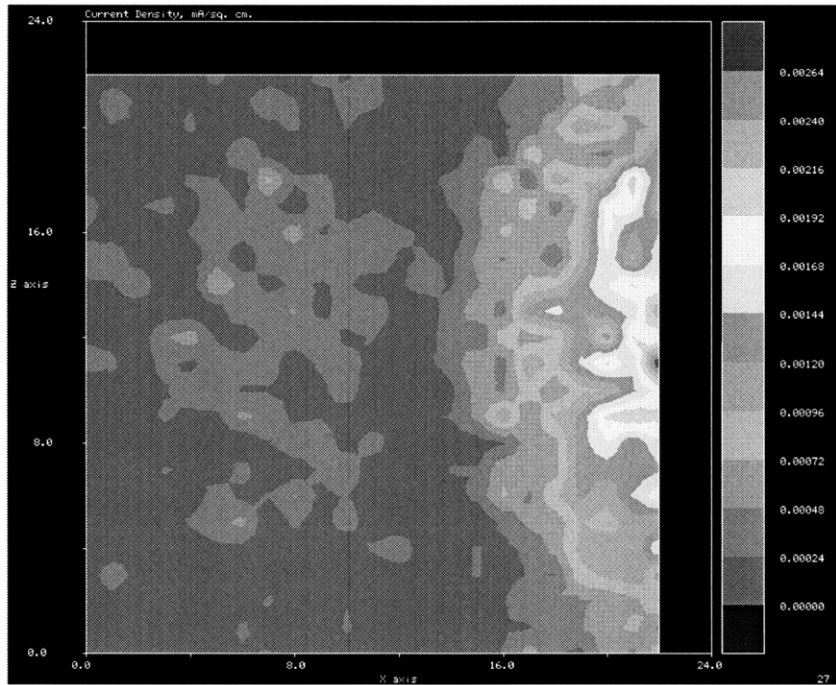# 5.7 Key Ion-Related Distributions on Solar Array

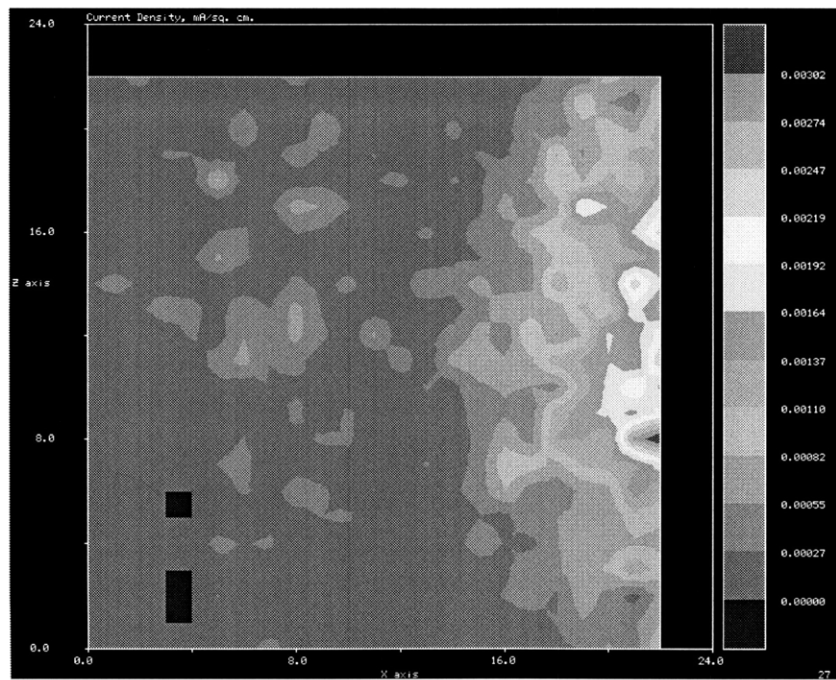**Figure 5.9   Current Density on Solar Array - Shield Length = 0.00 m**

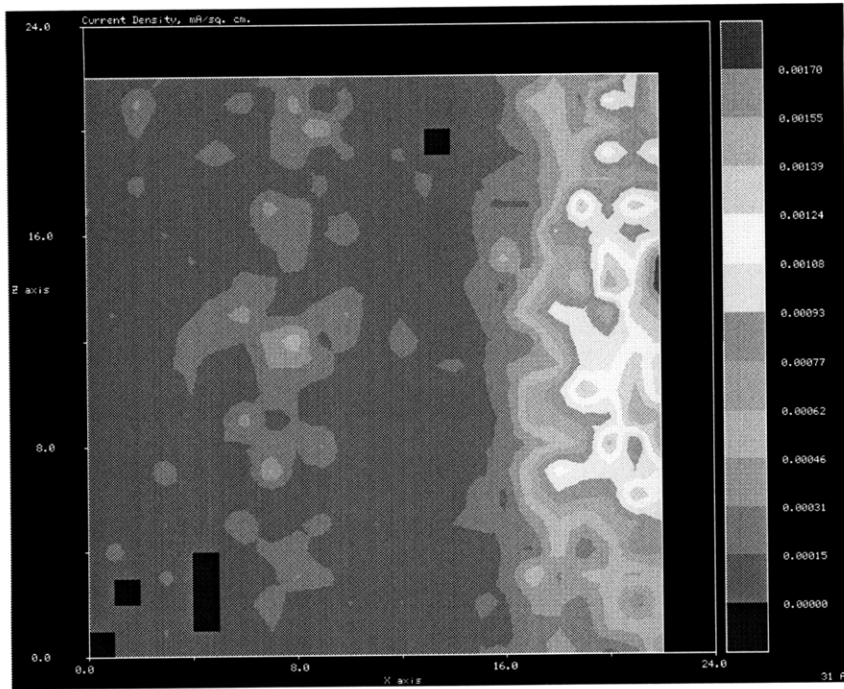**Figure 5.10   Current Density on Solar Array - Shield Length = 0.10 m**

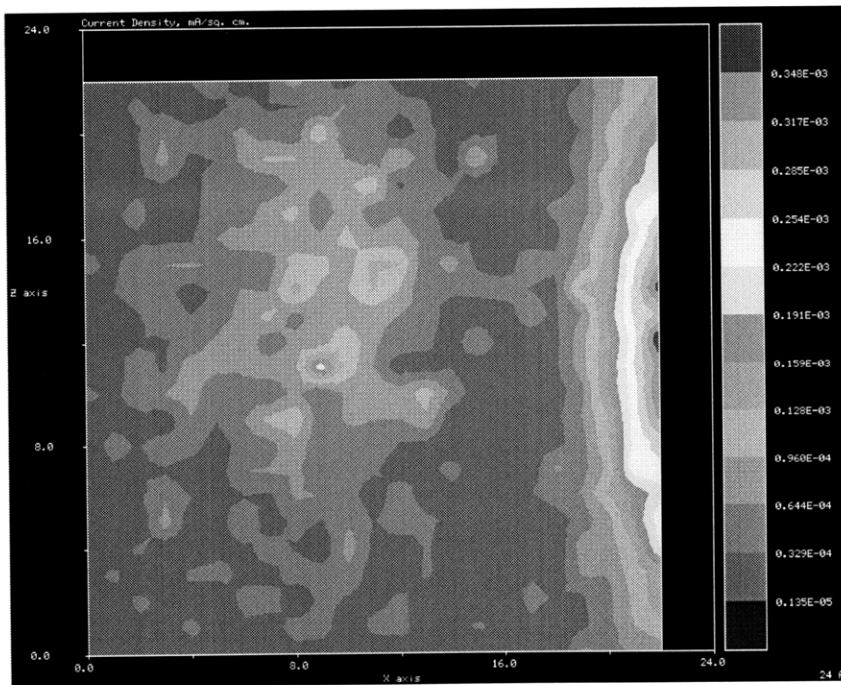**Figure 5.11   Current Density on Solar Array - Shield Length = 0.20 m**

Figure 5.12   Current Density on Solar Array - Shield Length = 0.30 m

Figure 5.13 Xe$^+$ Flux Distribution on Solar Array - Shield Length = 0.00 m

Figure 5.14 Xe$^+$ Flux Distribution on Solar Array - Shield Length = 0.10 m
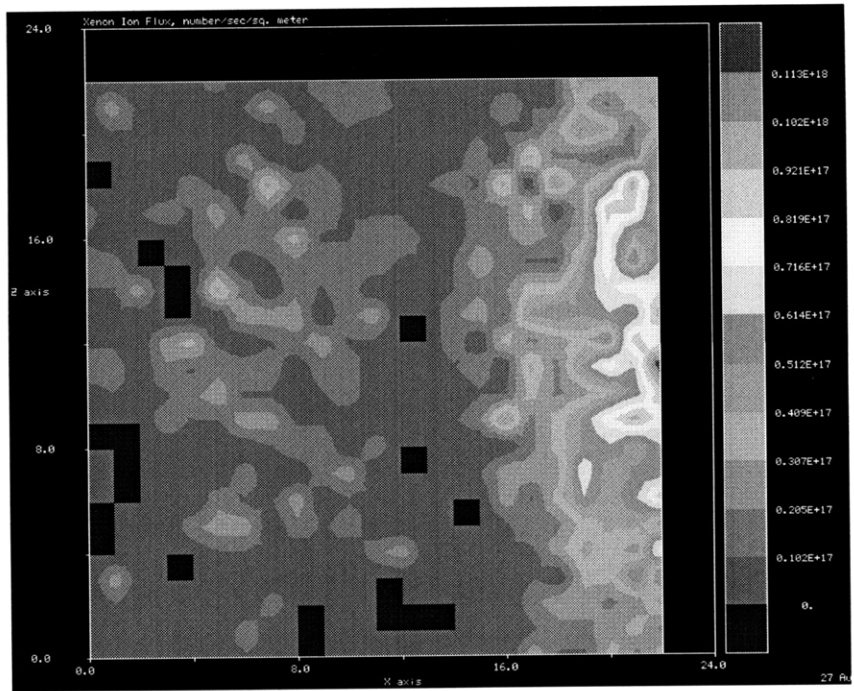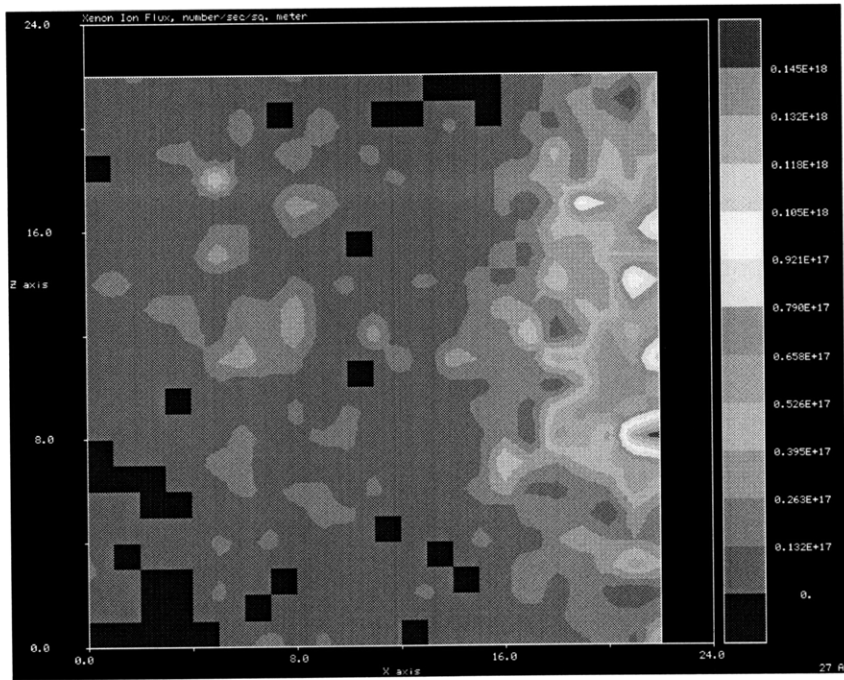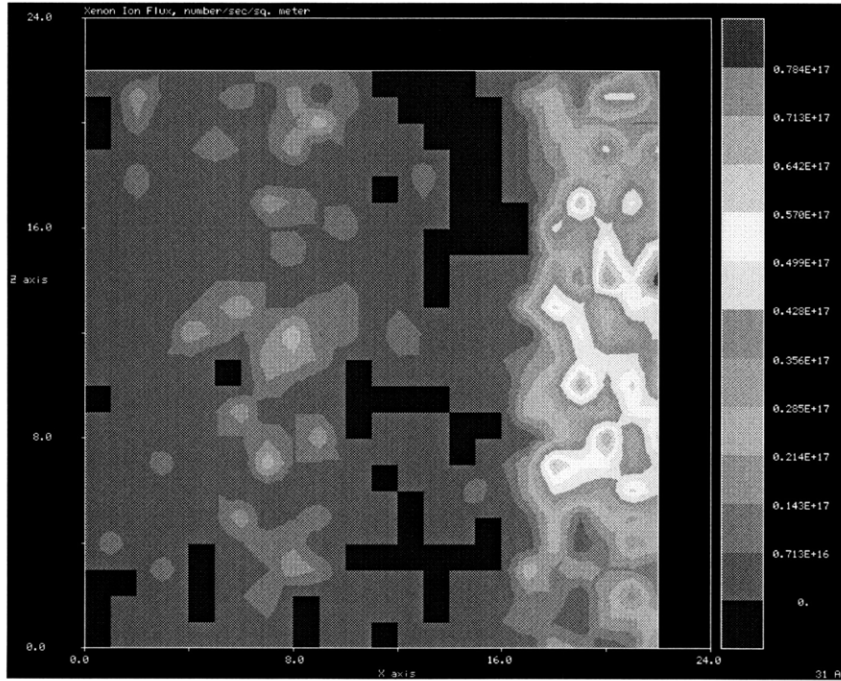
71

Figure 5.15 Xe⁺ Flux Distribution on Solar Array - Shield Length = 0.20 m

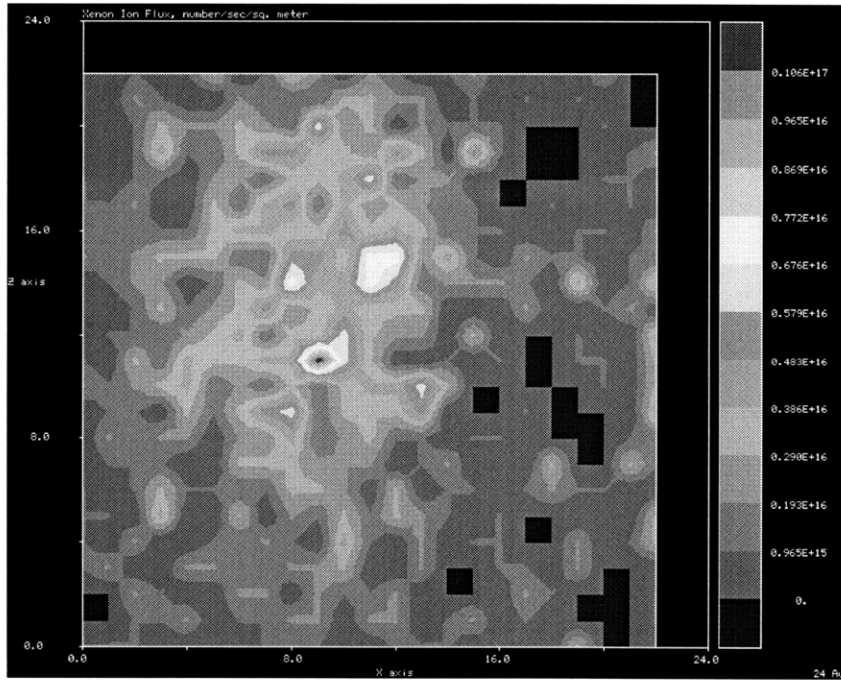**Figure 5.16 Xe⁺ Flux Distribution on Solar Array - Shield Length = 0.30 m**

Figure 5.17   Xe^{++} Flux Distribution on Solar Array - Shield Length = 0.00 m
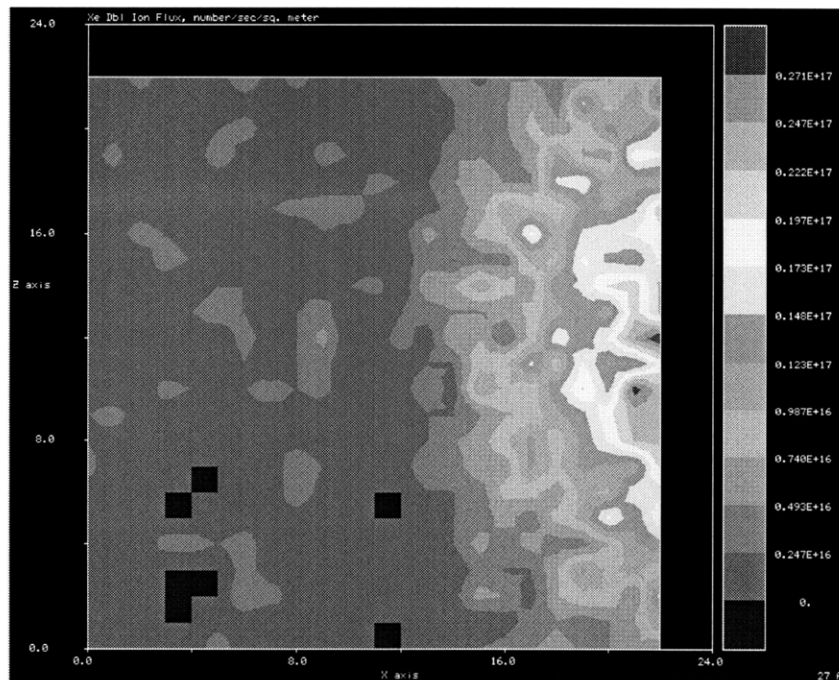
Figure 5.18   Xe^{++} Flux Distribution on Solar Array - Shield Length = 0.10 m
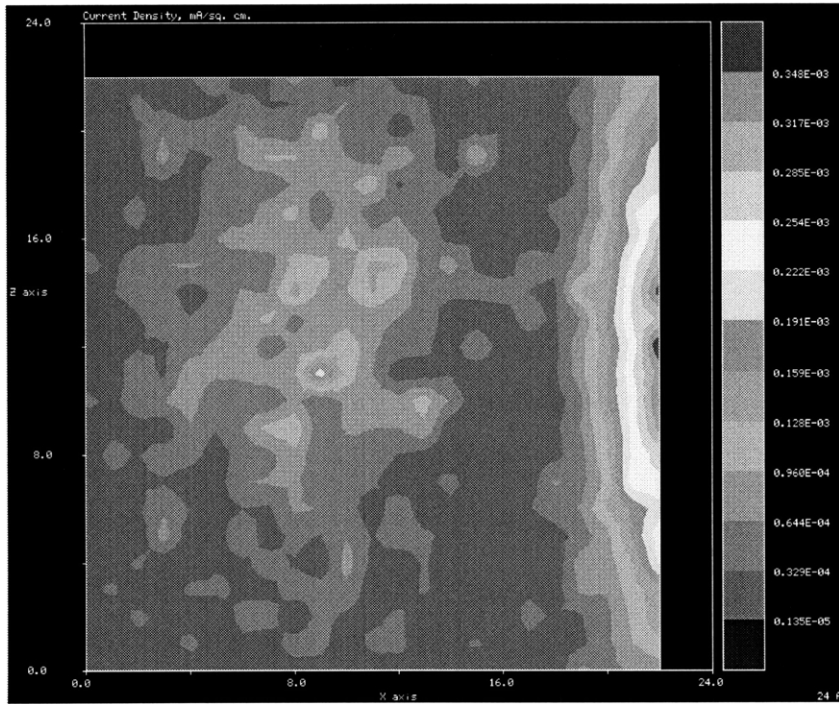
Figure 5.19   Xe^{++} Flux Distribution on Solar Array - Shield Length = 0.20 m
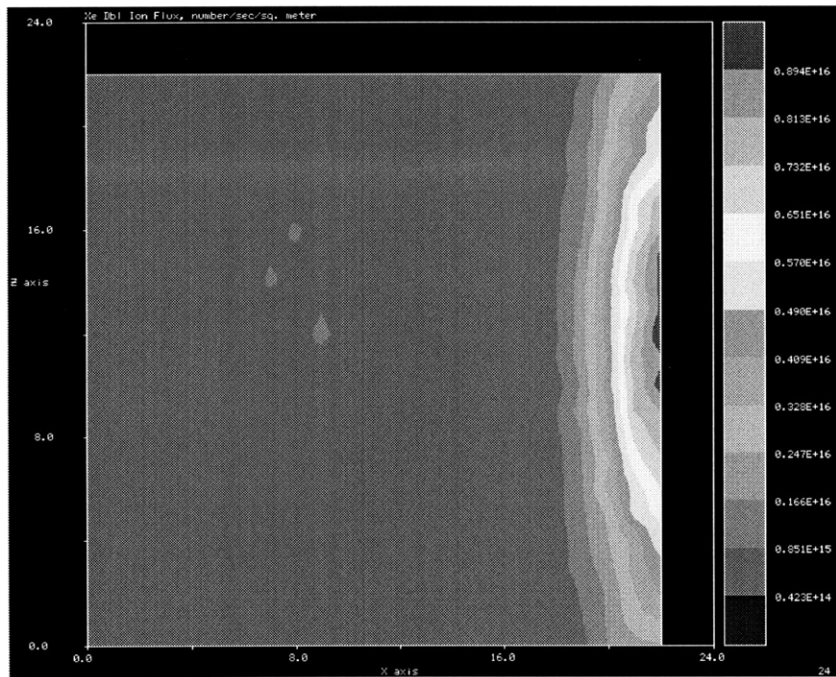
Figure 5.20   Xe^{++} Flux Distribution on Solar Array - Shield Length = 0.30 m
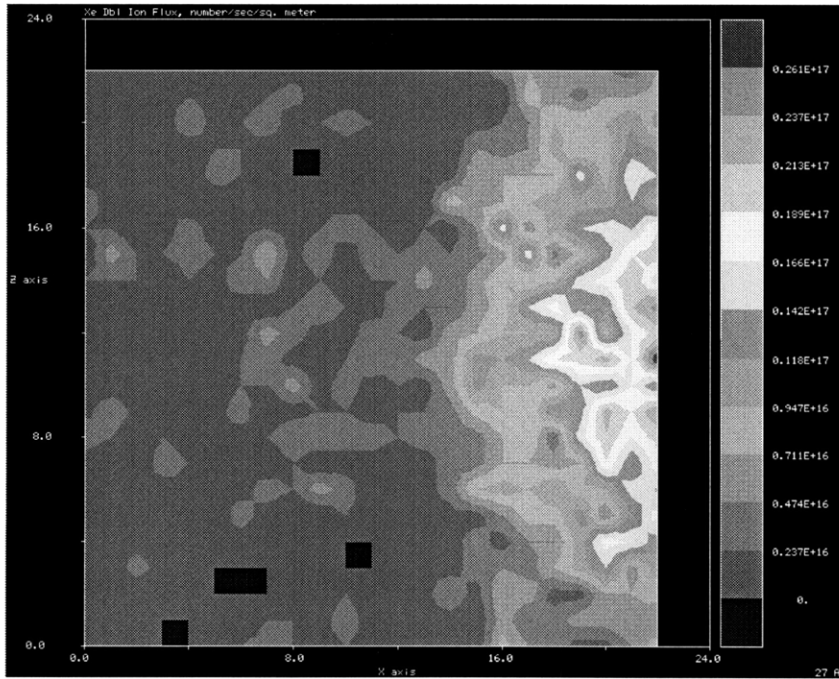
Figure 5.21 Quartz Erosion Rate on Solar Array - Shield Length = 0.00 m
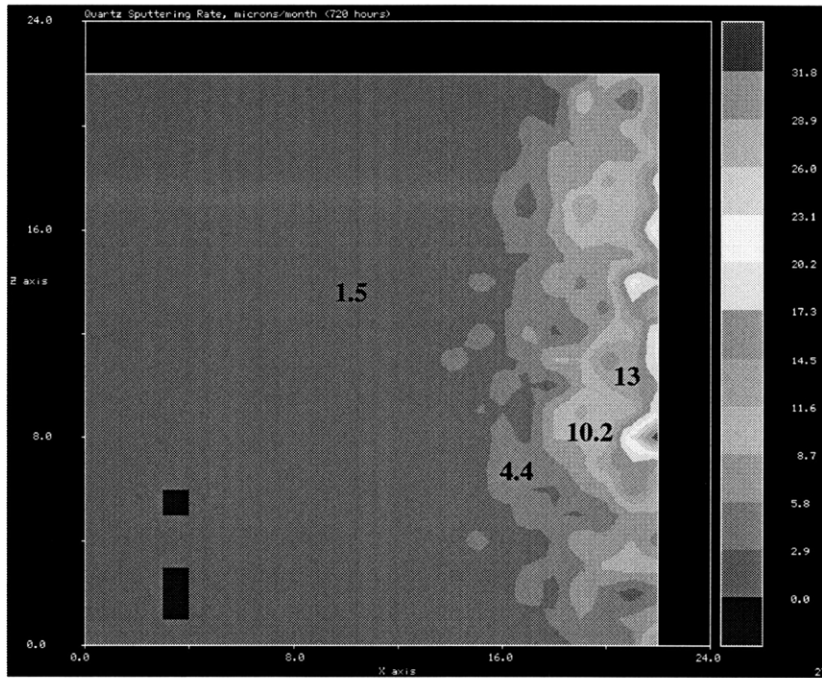
Figure 5.22 Quartz Erosion Rate on Solar Array - Shield Length = 0.10 m
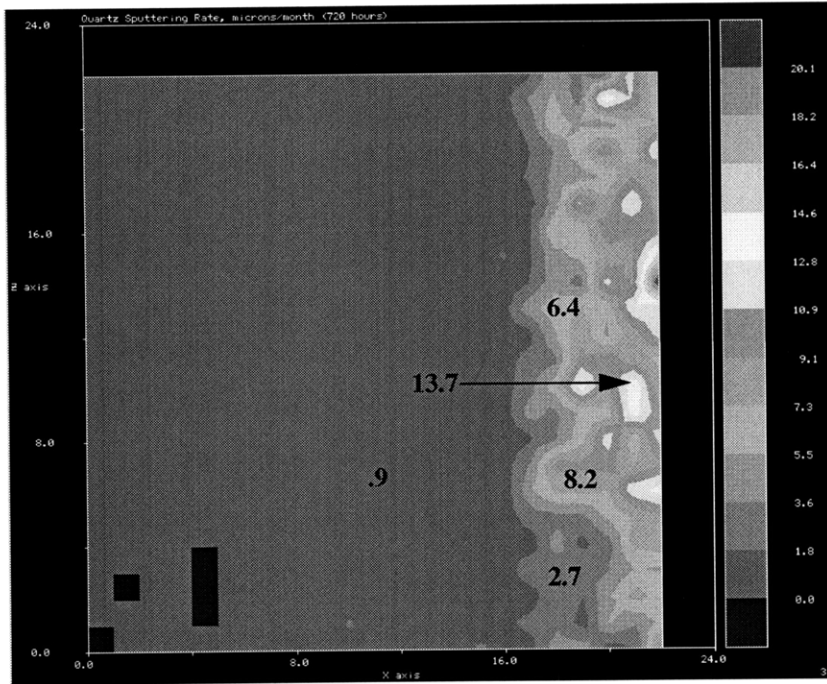
Figure 5.23   Quartz Erosion Rate on Solar Array - Shield Length = 0.20 m
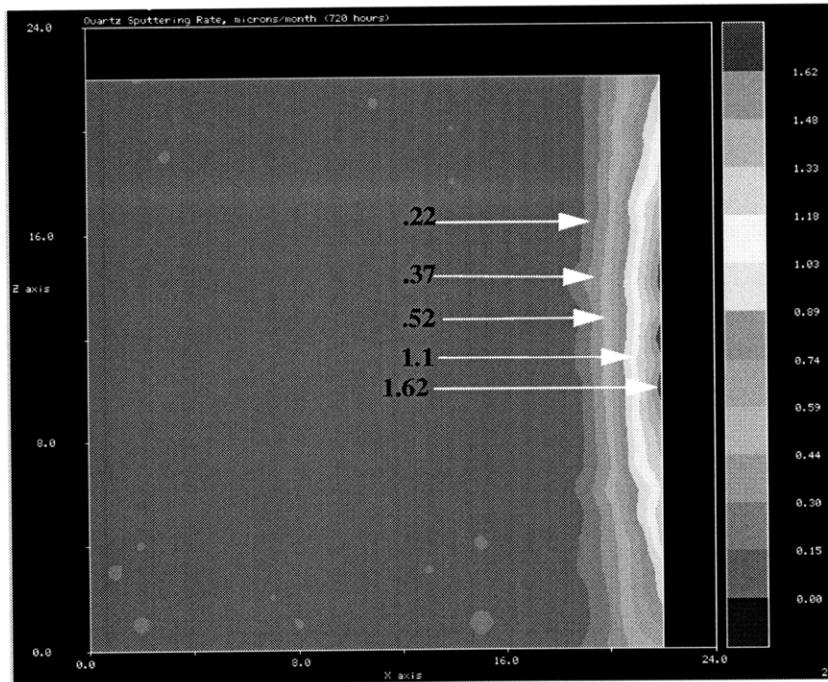
Figure 5.24   Quartz Erosion Rate on Solar Array - Shield Length = 0.30 m
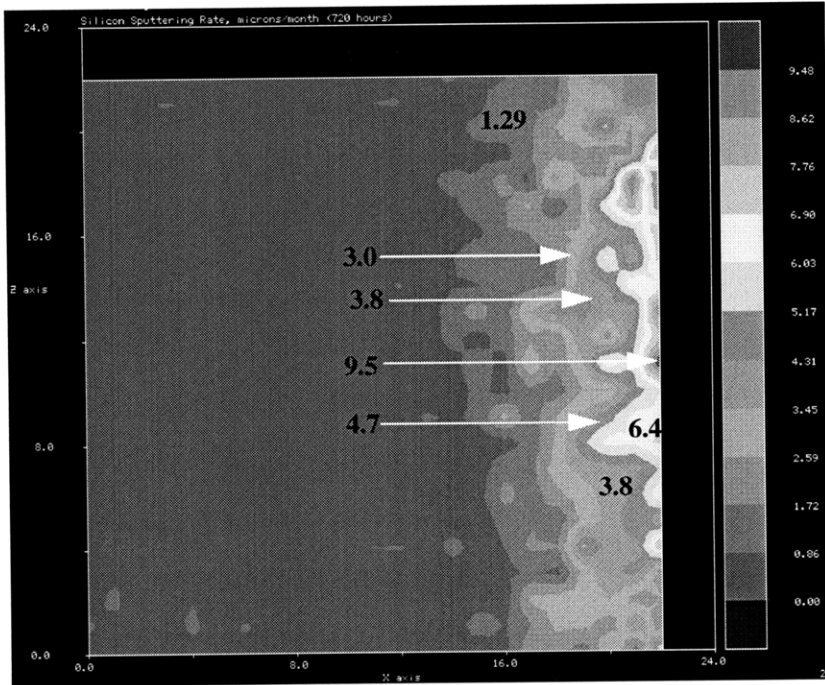
Figure 5.25   Silicon Erosion Rate on Solar Array - Shield Length = 0.00 m
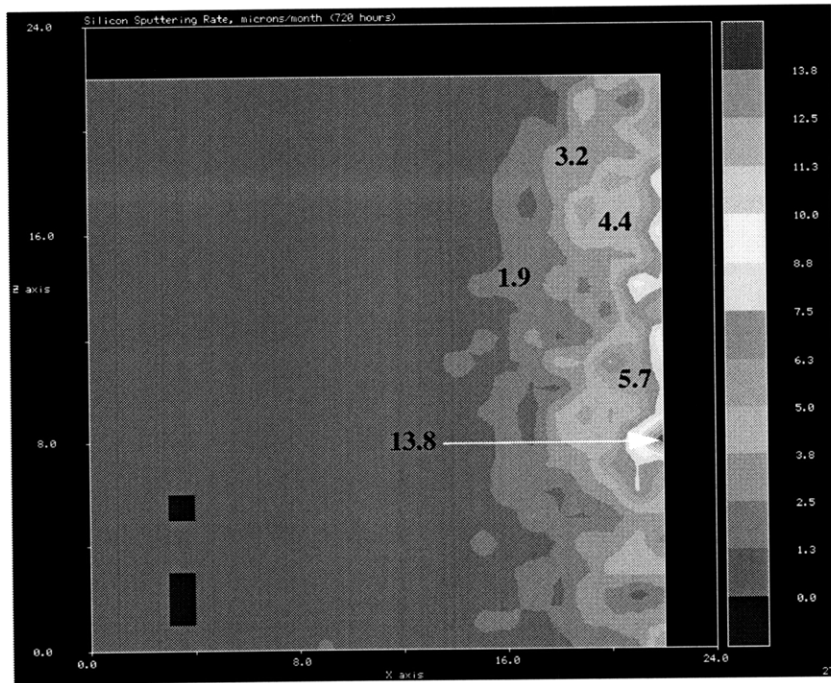
Figure 5.26   Silicon Erosion Rate on Solar Array - Shield Length = 0.10 m
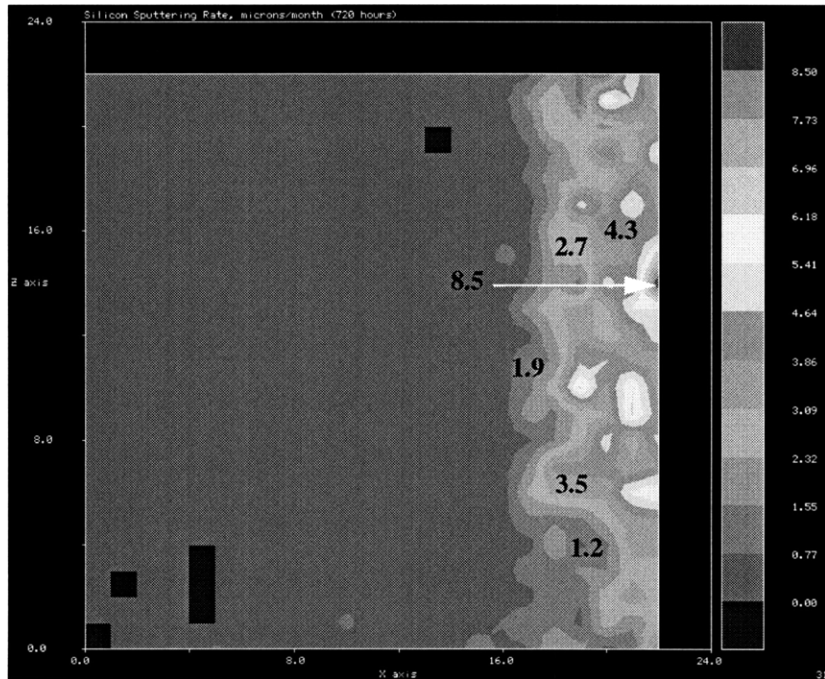
Figure 5.27   Silicon Erosion Rate on Solar Array - Shield Length = 0.20 m
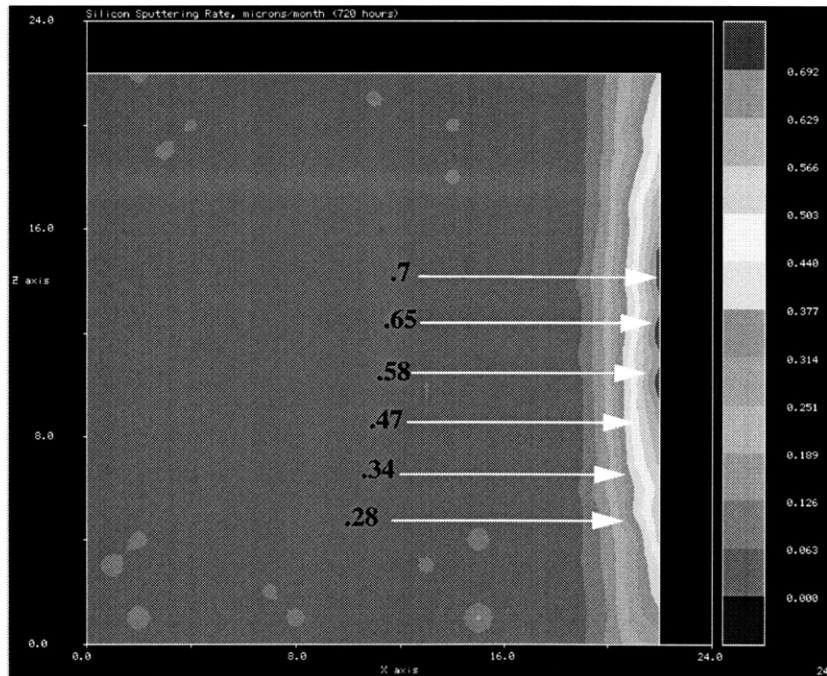
Figure 5.28   Silicon Erosion Rate on Solar Array - Shield Length = 0.30 m
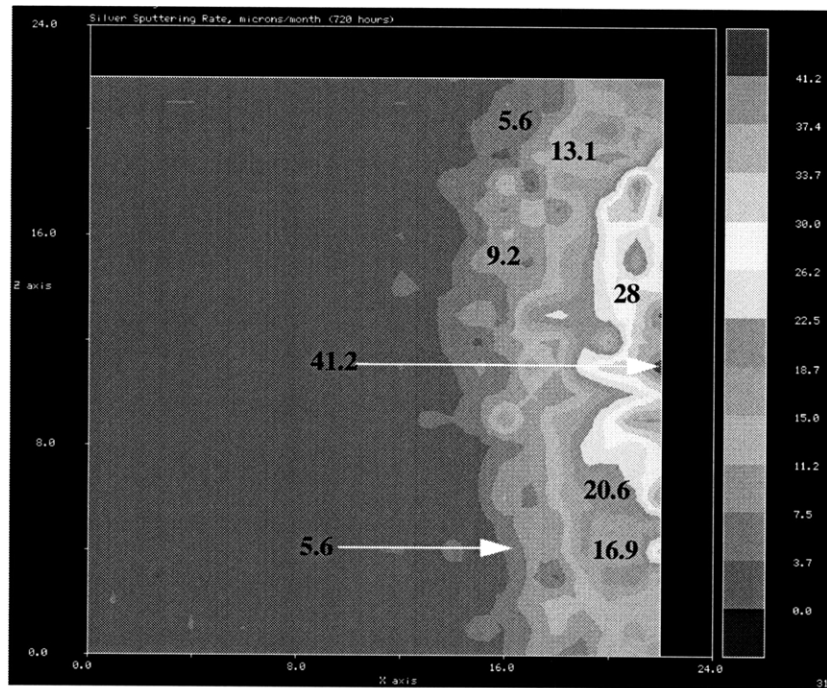
Figure 5.29   Silver Erosion Rate on Solar Array - Shield Length = 0.00 m

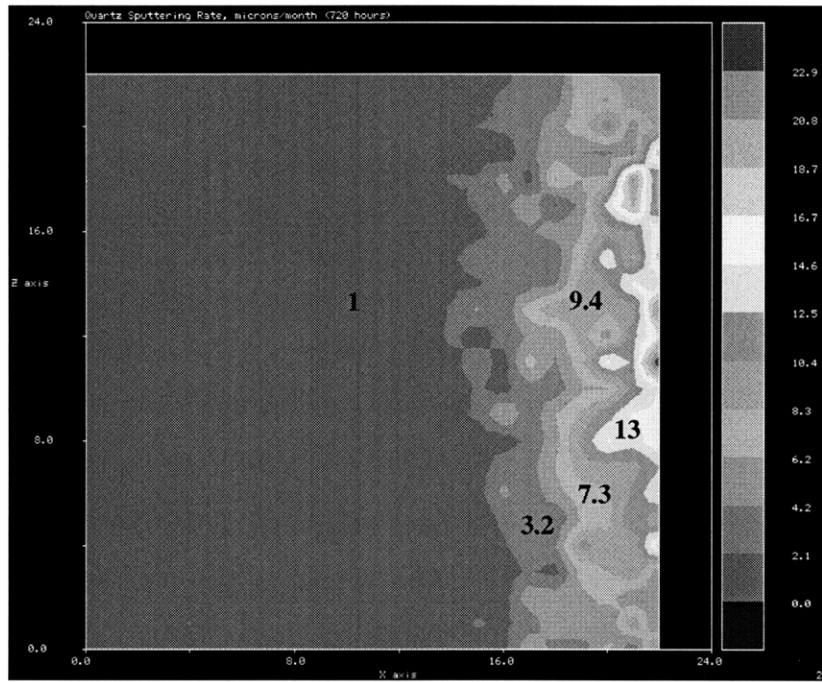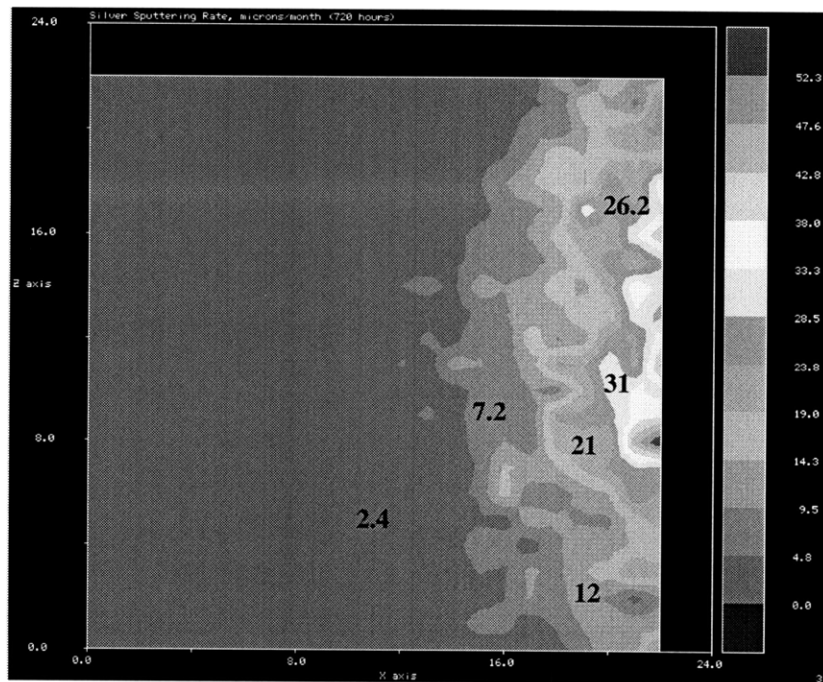**Figure 5.30   Silver Erosion Rate on Solar Array - Shield Length = 0.10 m**
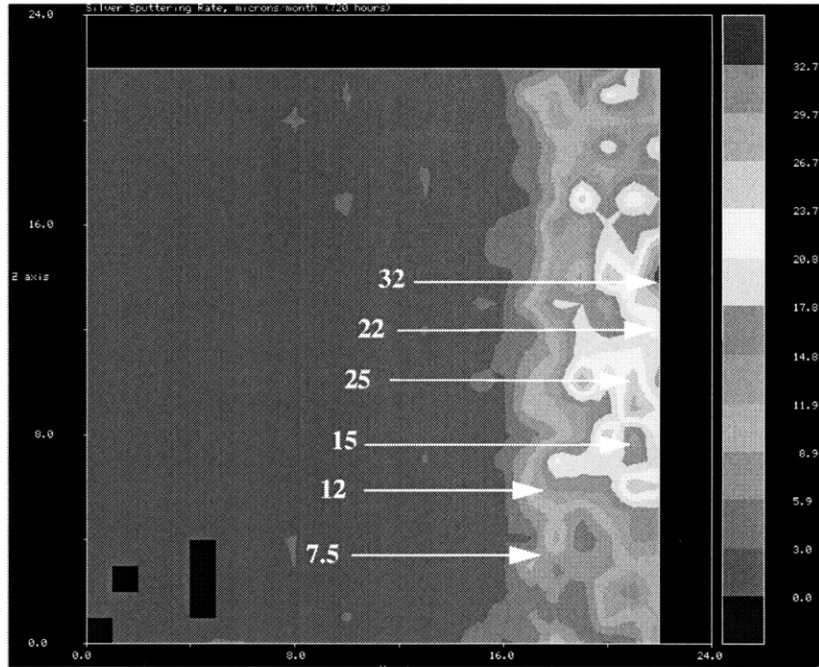
Figure 5.31   Silver Erosion Rate on Solar Array - Shield Length = 0.20 m
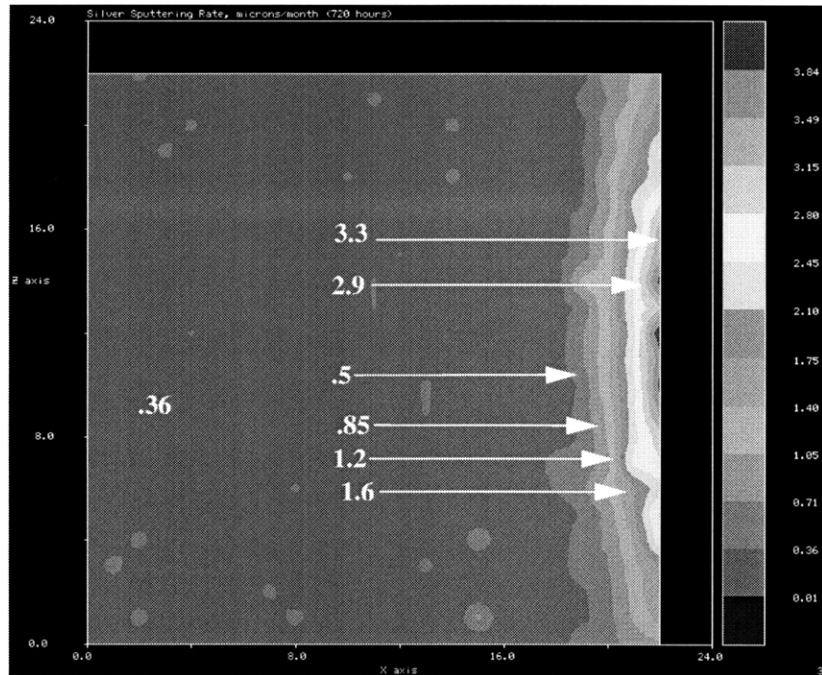
Figure 5.32   Silver Erosion Rate on Solar Array - Shield Length = 0.30 m

5.8 Neutral (Xe) Flux Distribution on Array
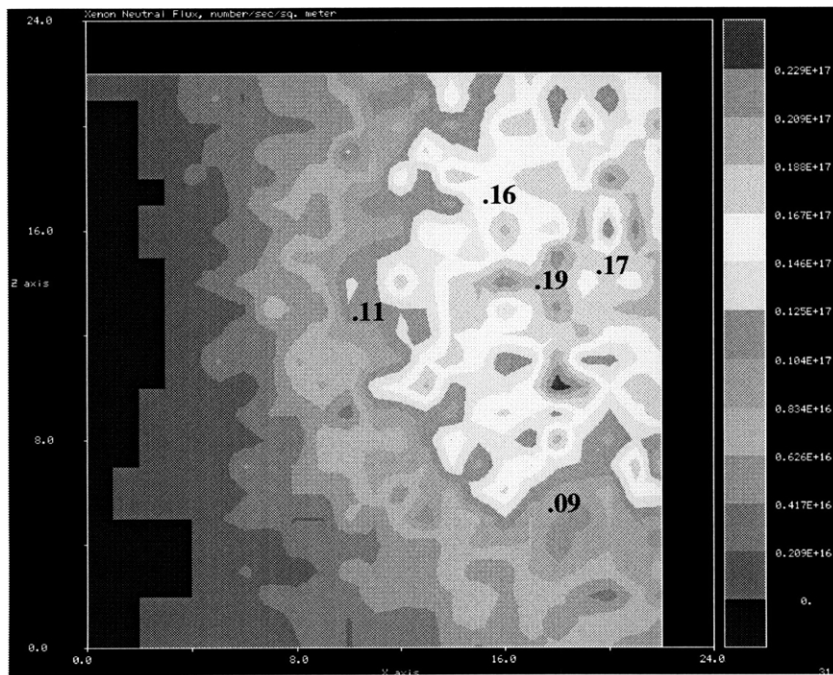
Figure 5.33   Xe Neutral Flux Distribution (x10^{17}) on Solar Array - Shield Length = 0.00 m
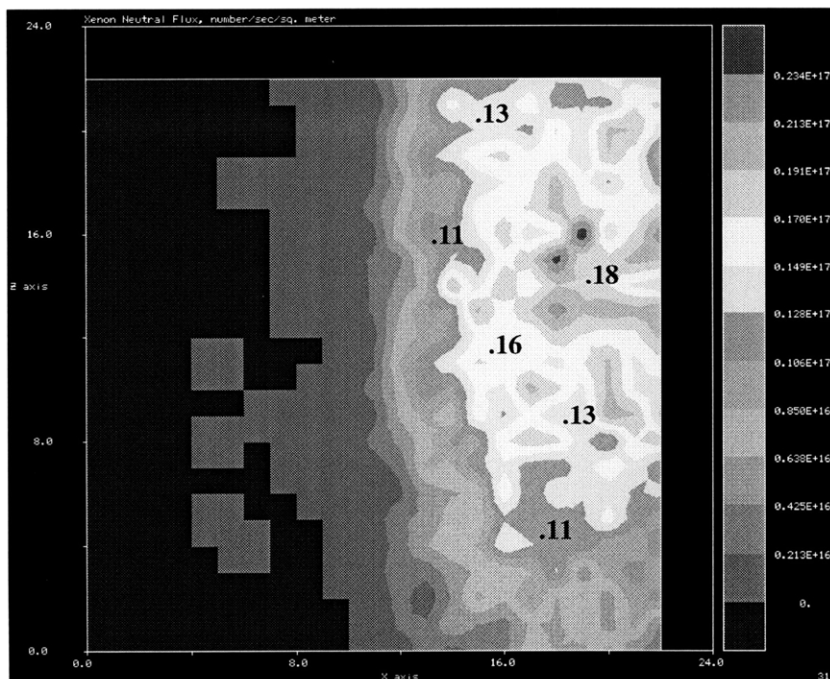
Figure 5.34   Xe Neutral Flux Distribution (x10^{17}) on Solar Array - Shield Length = 0.10 m
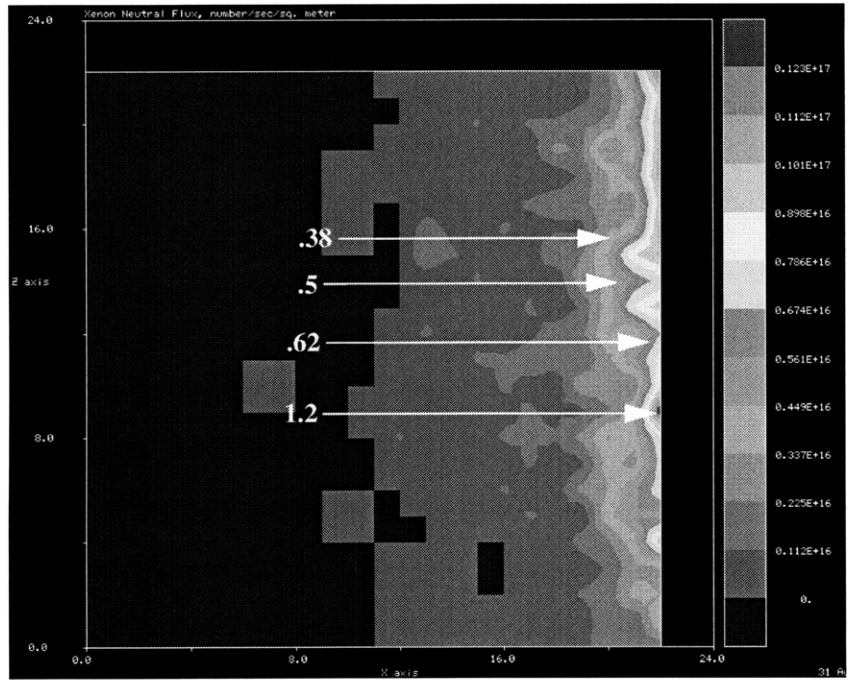
Figure 5.35   Xe Neutral Flux Distribution (x10^{16}) on Solar Array - Shield Length = 0.20 m

5.9 Neutral (Xe) Impact Energy Distribution on Array
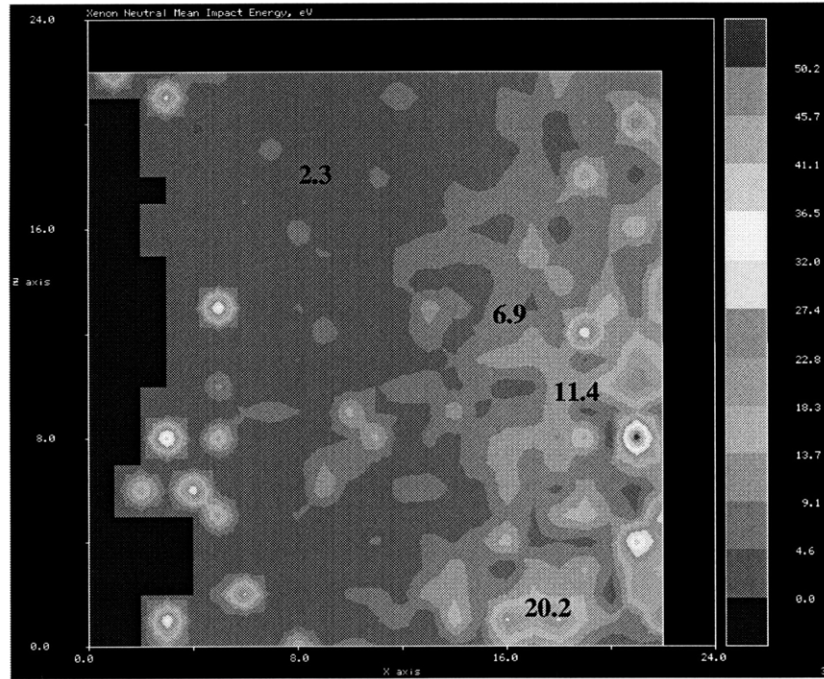
Figure 5.36   Xe Neutral Energy Distribution on Solar Array - Shield Length = 0.00 m
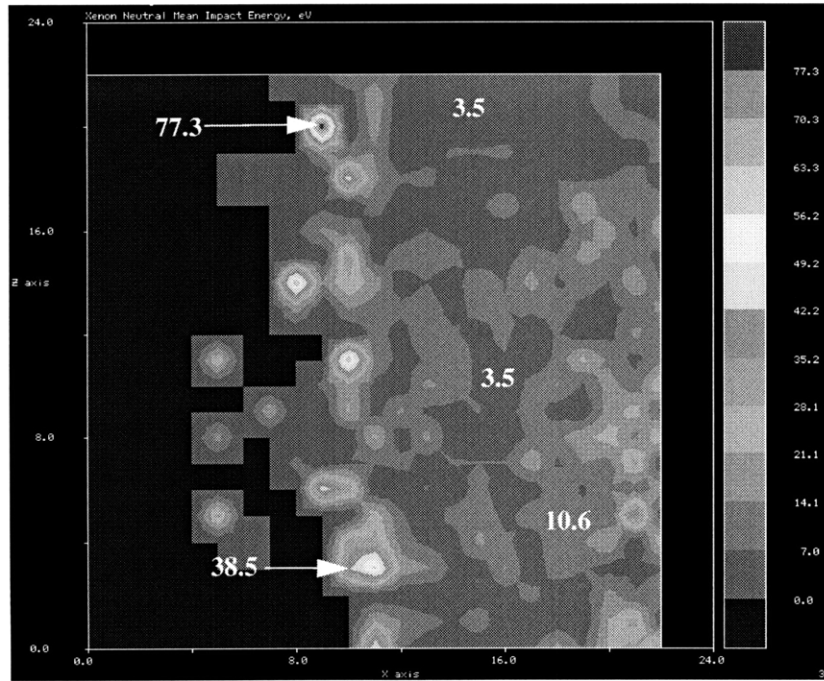
Figure 5.37   Xe Neutral Energy Distribution on Solar Array - Shield Length = 0.10 m
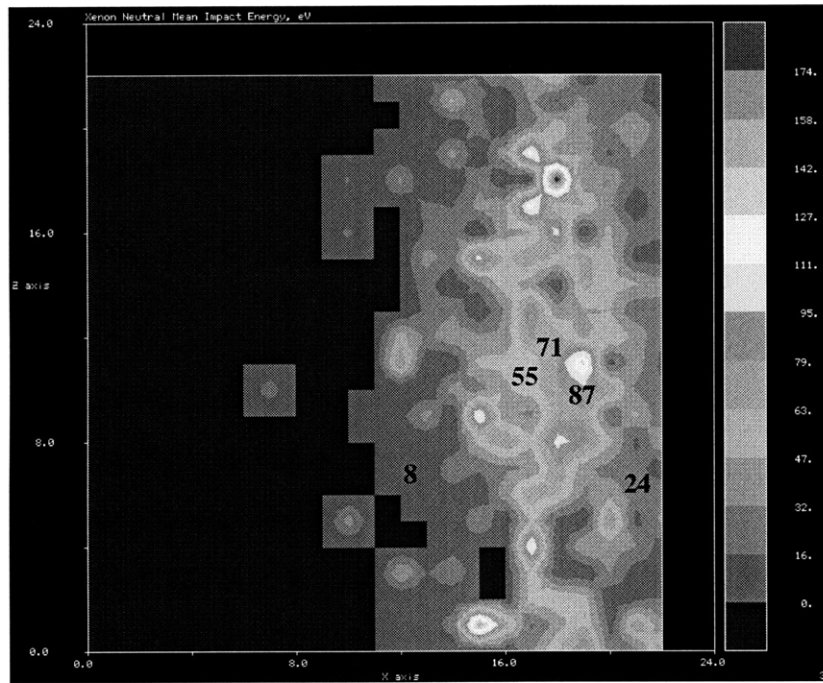
Figure 5.38 Xe Neutral Energy Distribution on Solar Array - Shield Length = 0.20 m

5.10 Erosion Rates of Solar Array and Shield Wall
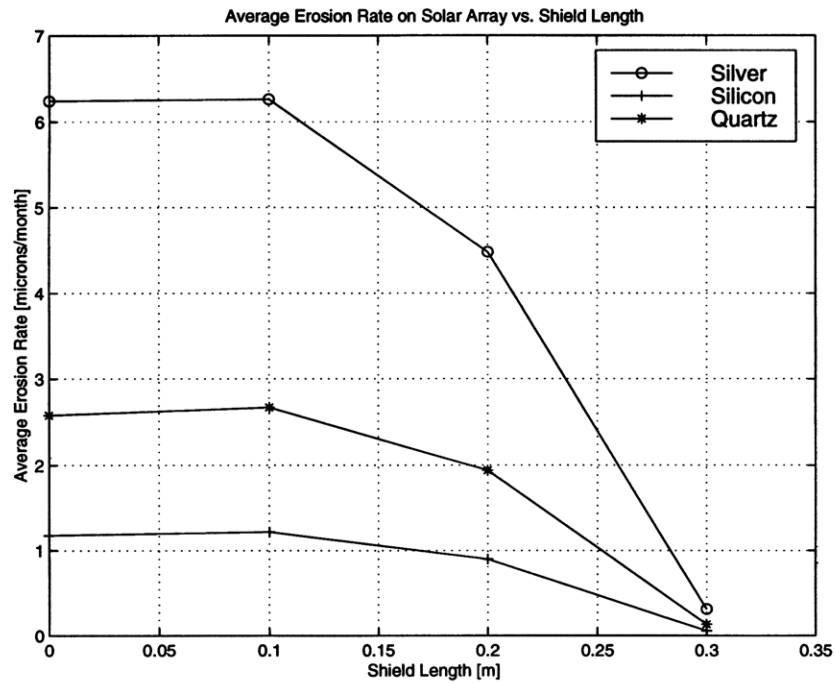
Figure 5.39   Erosion Rate for Silver, Silicon and Quartz on Solar Array vs. Shield Length
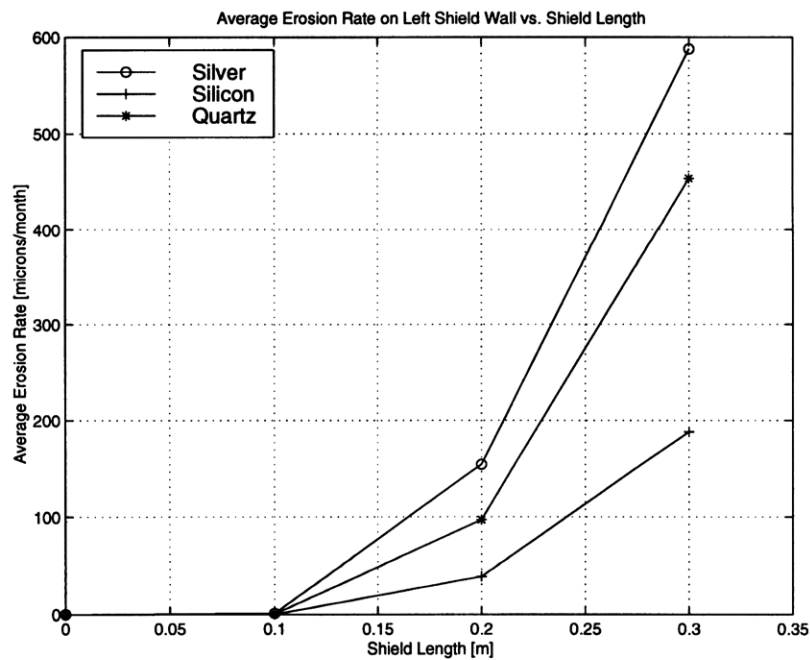
Figure 5.40   Erosion Rates on Left Wall of Shield

5.11 Deposition of Aluminum on Solar Array
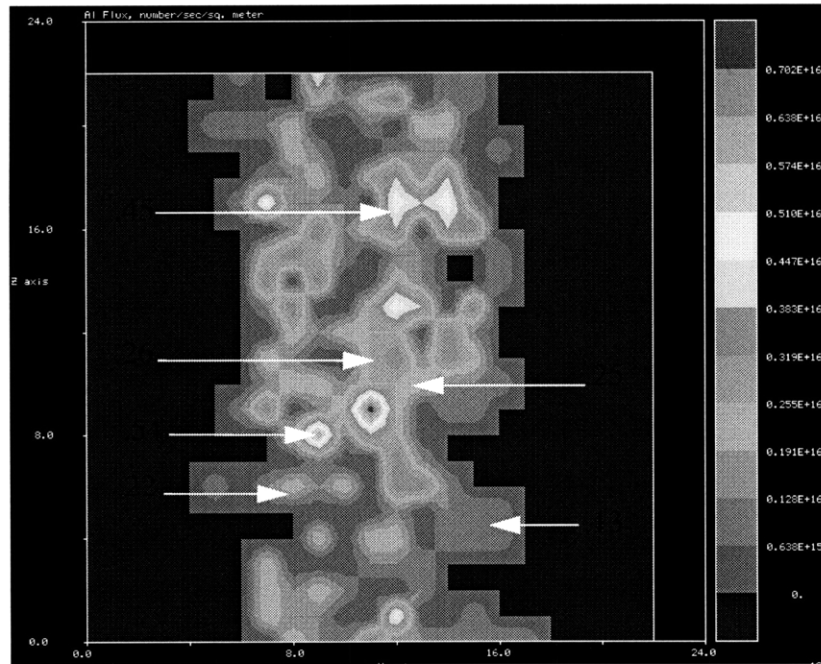
Figure 5.41   Aluminum Deposition Distribution ($\times 10^{16}$) on Solar Array - Shield Length = 0.10 _m_
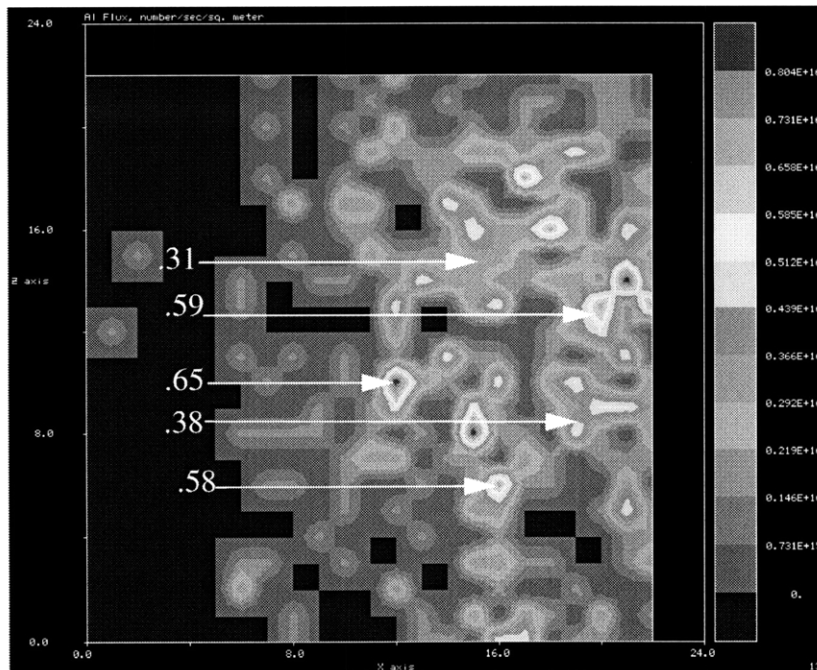
Figure 5.42   Aluminum Deposition Distribution ($\times 10^{16}$) on Solar Array - Shield Length = 0.20 _m_
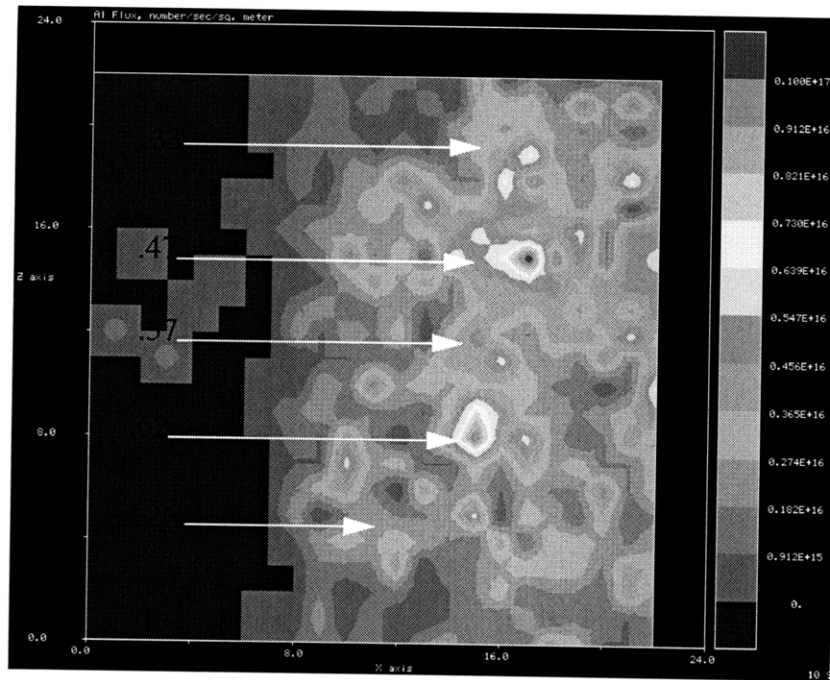
Figure 5.43 Aluminum Deposition Distribution (x10^{16}) on Solar Array - Shield Length = 0.30 *m*

5.12 Collimating Effect of Shield Visualized
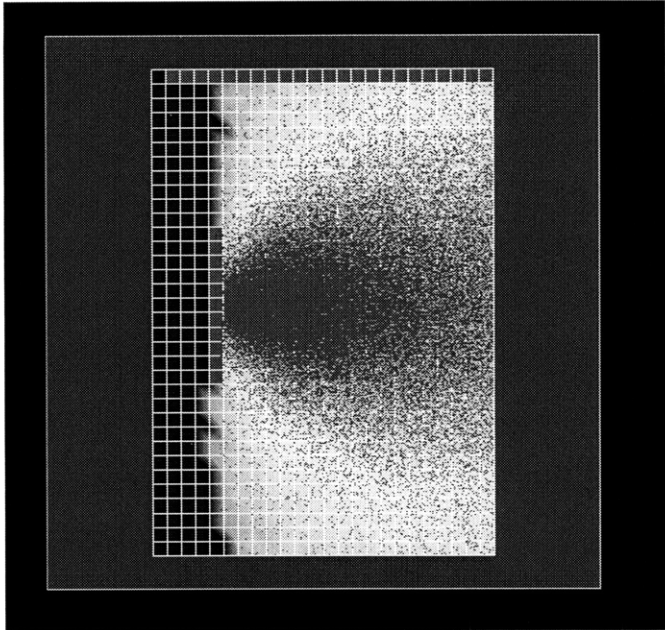
Figure 5.44   Plume Particle Distribution Without Protective Shield
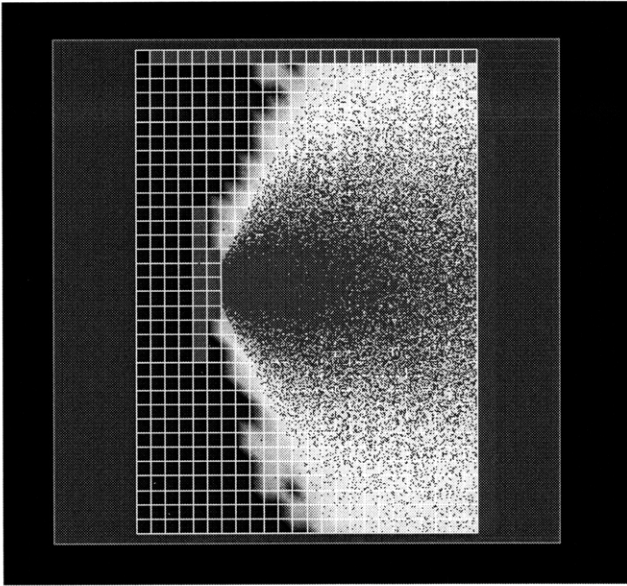
Figure 5.45   Plume Particle Distribution - Shield Length = 0.10 m
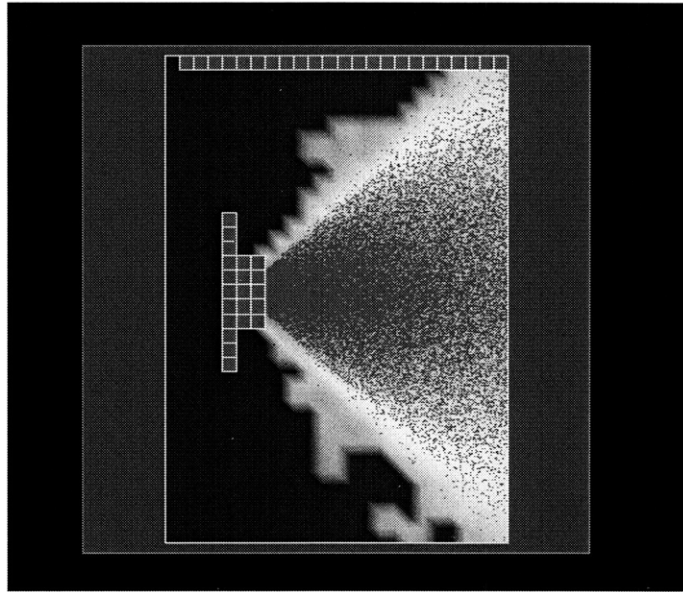
Figure 5.46   Plume Particle Distribution - Shield Length = 0.20 m
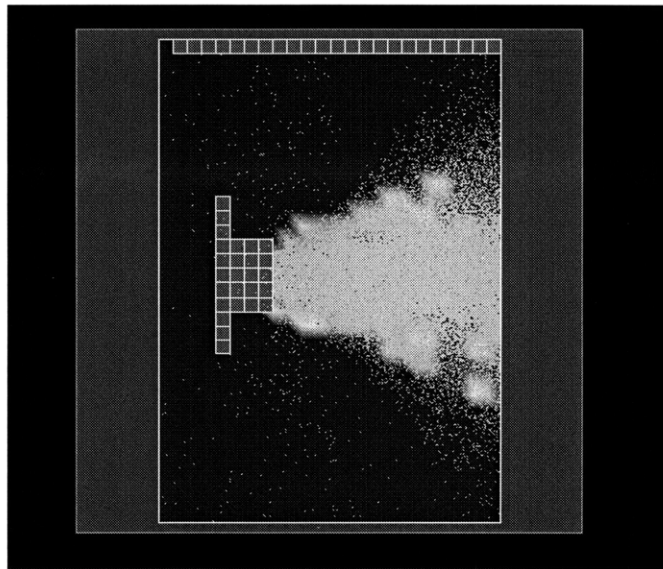
Figure 5.47   Plume Particle Distribution - Shield Length = 0.30 m

5.13 Deposition of Shield Material on Solar Array
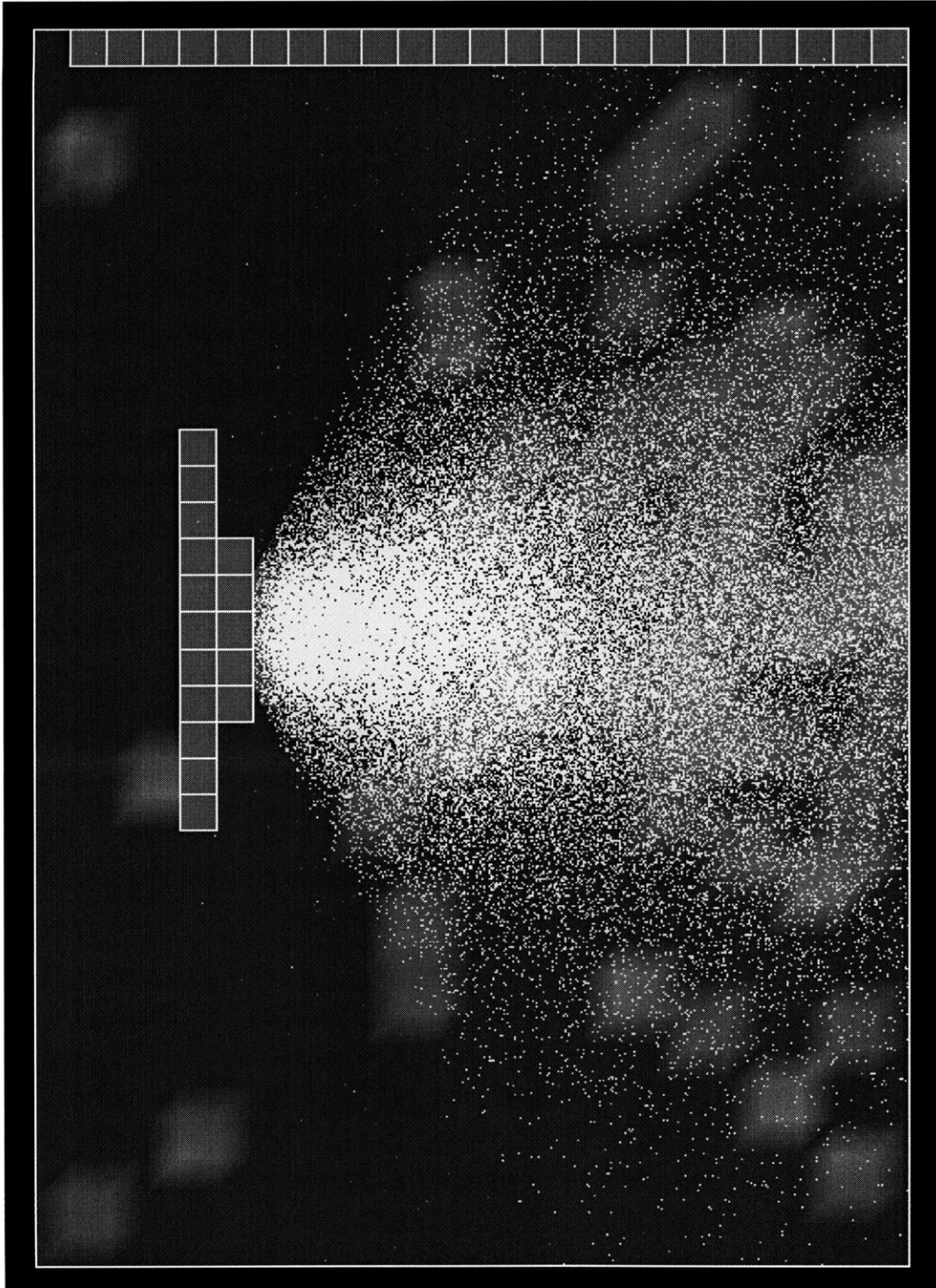
Figure 5.48   Aluminum Deposition on Solar Array - Shield Length = 0.10 *m*
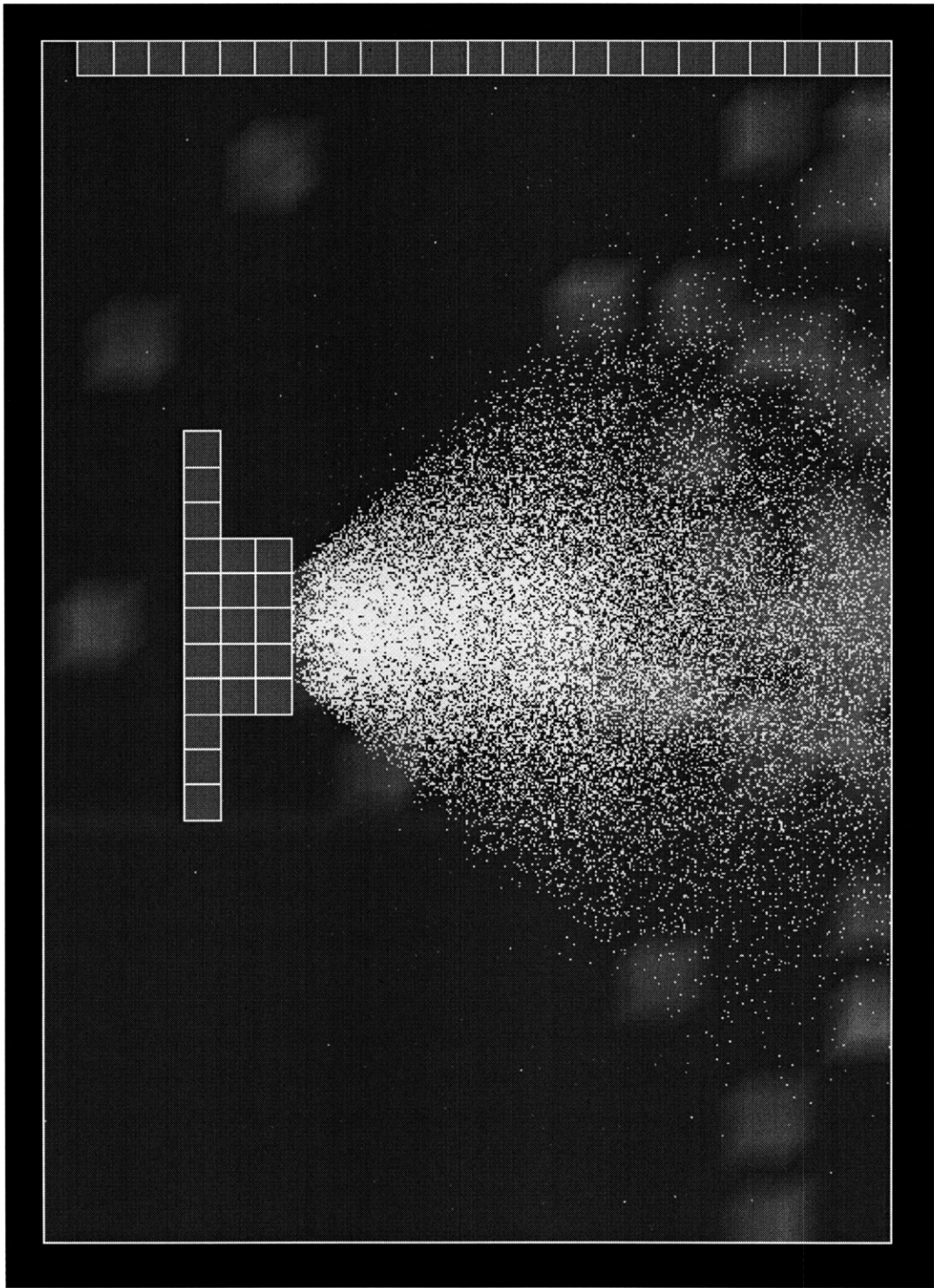
Figure 5.49   Aluminum Deposition on Solar Array - Shield Length = 0.20 *m*
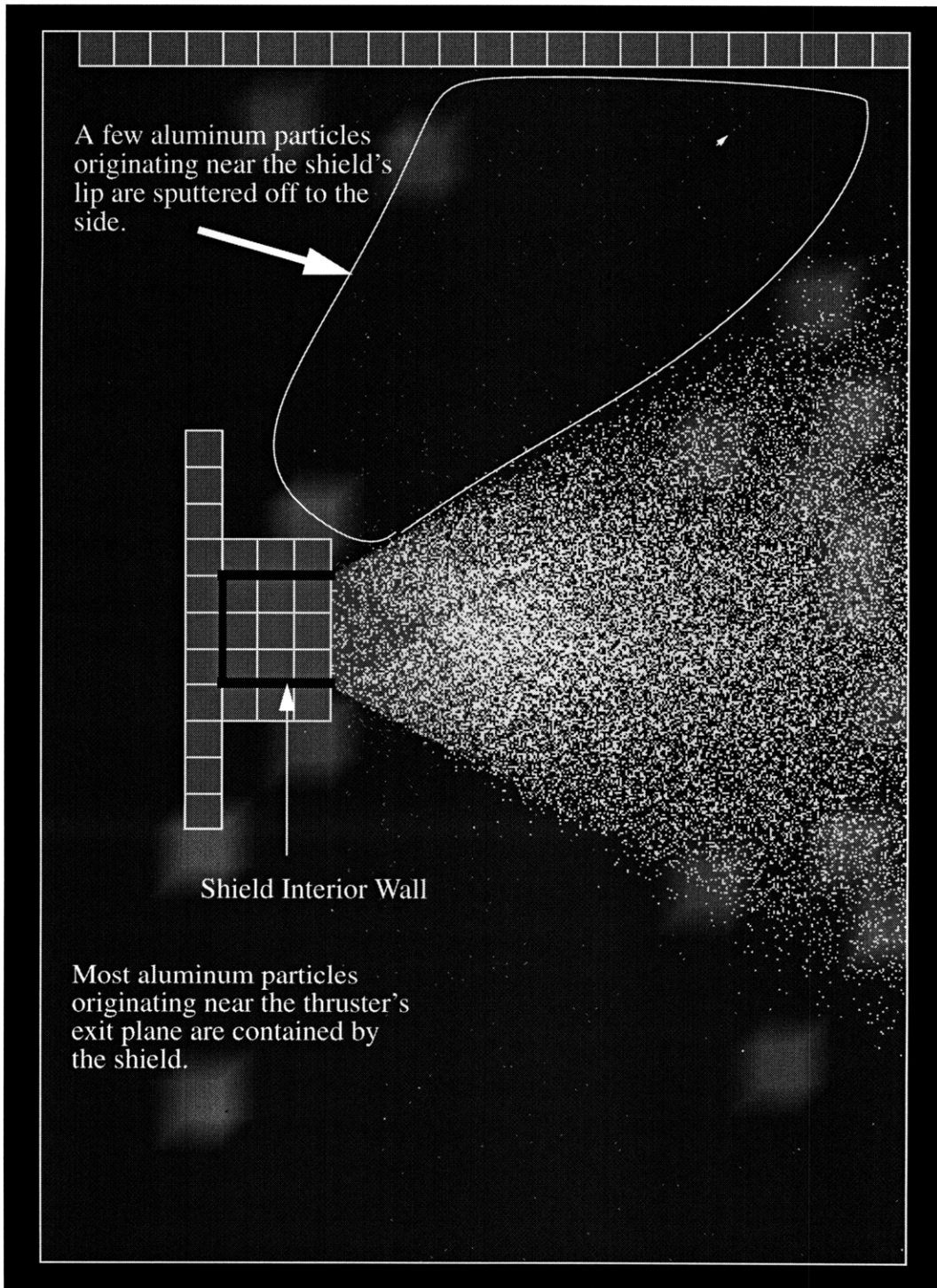
Figure 5.50 Aluminum Deposition on Solar Array - Shield Length = 0.30 *m*

5.14 Summary

Charge exchange ions created in the plume of a Hall Thruster are primarily responsible for the degradation of spacecraft sub-components located very close to the exit plane of the EP device i.e. in the backflow region. In order to protect the spacecraft from the energetic ions, a protective shield (shroud) was placed concentrically around the exit of the thruster and its length (away from the exit plane) was varied with each simulation.

The 0.2 m shield had a collimating effect on the beam and it prevented CEX ions from reaching the backplane of the thruster. It was found that shield lengths shorter than 0.1m had little impact in preventing erosion of the solar arrays whereas shield lengths greater than 0.2 m actually did protect the arrays. For the particular configuration chosen, lengths greater than 0.3 m prevented CEX ions from hitting the solar array and thus there was very little erosion of the array.

It has also been observed from the computation that even though the shield is effective in protecting the modeled solar array from the erosive effects of the HT plume, the presence of a shield introduced a new problem. The shield itself is subject erode and its sputtered material is shown to redeposit on the solar array. More importantly, for longer shields (length > 0.2 m) it is found that most of the shield erosion occurs in the region closer to the exit plane of the thruster and most of the material is deposited around the shield's lip region. The results indicate that the longer the shield is, the better it shields the solar array from damage (both ion and deposition), but the model for angular distribution of particles being ejected needs to be fully implemented to draw precise conclusions about the latter. Of course this needs to be traded off against the additional weight and volume of a very long shield. This trade can be facilitated by our results on shield erosion.

Chapter 6

Conclusion

A PIC-DSMC algorithm has been developed at MIT in the Space Systems Laboratory to model the expansion of plasma from an SPT thruster into a vacuum. This model is based on theoretical work initiated by Oh in 1997 which assumed the plasma to be a quasi-neutral gas with collisionless electrons. It also included a surface interaction model which calculated erosion rates on realistic spacecraft geometries and was used in studying the impact of using protective shields to protect spacecraft subcomponents. The results of this work as well as recommendations for future work are summarized below.

6.1 Results

The goal of this work was to improve the computation of sputtering yields in the 0 eV to 1000 eV energy range, as well as to track the material sputtered from any object interacting with the energetic plume. This was achieved by adopting Matsunami's and Yamamura's energy and angular dependent sputtering yields in the sub 1 keV energy range, although some aspects of their numerical implementation were not completed.

The plasma properties in a tank were studied and it has been concluded that in order to fully understand how the ionized gas interacts with a vacuum tank it is necessary to increase the simulation time three to four fold (unless smaller tanks are simulated). This would allow the plasma to reach an equilibrium state, equivalent to that achieved when running a thruster in a real facility.

Since the plume has such an erosive effect on spacecraft subcomponents in its vicinity, a shield which diverts the beam away from critical systems was proposed and the trade-

offs studied. An aluminum shield, 15 *cm* in diameter was mounted concentrically around the thruster exit and its length was varied from 0 *m* to 0.3 *m*. It was observed that a shield, in fact, was effective in preventing the energetic CEX ions from damaging the modeled solar array but introduced a new level of complexity in the form of material sputtered off its walls. Results from the 'shield study' suggest that in order to fully protect the spacecraft from the damaging CEX ions created in the plume as well as to minimize the redeposition of material sputtered from the shield, it is necessary to use the longest possible shield though this needs to be traded off against it weight, volume and cost. Future research should include studying the effects of different materials for manufacturing such a shield and the impact of size and shape on the shield's effectiveness.

6.2 Recommendations for Future Work

- Since King and Gallimore [1998] provided the first ever documentation of the existence Xe^{+++} ions in the plume of a Hall thruster, a future computational model should include CEX collisions which produce these triply charged energetic ions. Even though less than 1% of the plume consists of triply charged xenon ions, they will hit surfaces with energy 3 times as high as the singly charged ions currently do, thus damaging spacecraft components which may see no erosion otherwise, because Xe^+ or even Xe^{++} may be below threshold.

- The sensitivity of the plume to electron temperature variations should be studied in detail since VanGilder *et al.* found that the results from a model implementing a variable electron temperature agreed better with experimental data. Thus in order to improve Oh's PIC-DSMC algorithm a variable electron model needs to be implemented in future work.

- In order to study plasma instabilities in a Hall thruster a time-dependent plume code needs to be implemented though re-writing the current code might prove infeasible. Qarnain [1998] concluded that the time step required to include plasma instabilities might increase the total running time of the simulation tenfold.

- Since the development of the code by Oh, *Sankovic* [1997] showed that contamination by particulates from the thruster channel are a problem at high angles from

the thrust axis. Future work should include these particles in the source model of the thruster.

- In the surface interaction model implemented, neutrals are reflected with 20% less energy than the had prior to impact. It is assumed that in the low energy range (<100eV) this model might be adequate but when considering higher impact energy ranges (>100eV) this model will have to be revised to include various sputtering regimes.

Appendix A

Sputtering Yield vs. Incident Energy at 45° Angle of Incidence
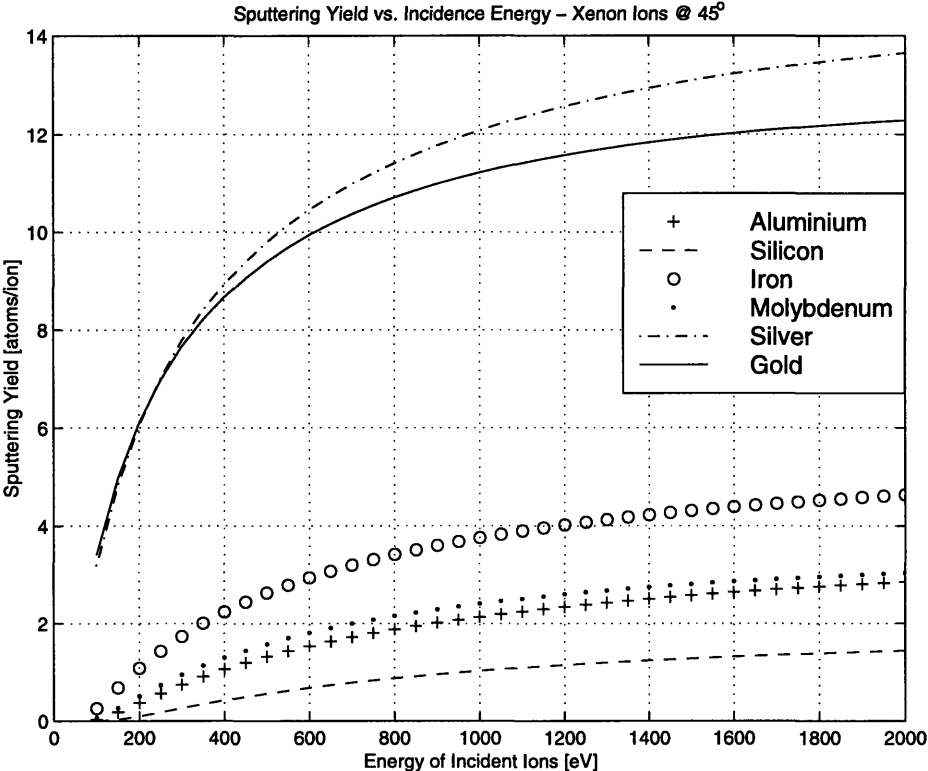
Figure A.1: Sputtering Yield vs. Incidence Energy at 45° Angle of Incidence

Appendix B

Sputtering Yield vs. Incidence Angle

These graphs show the theoretical sputtering yield as derived in Section 3.3 and Section 3.0.1 for energetic xenon ions impinging on aluminum, silicon, iron, molybdenum, silver and gold in the 150eV to 1000eV energy range.
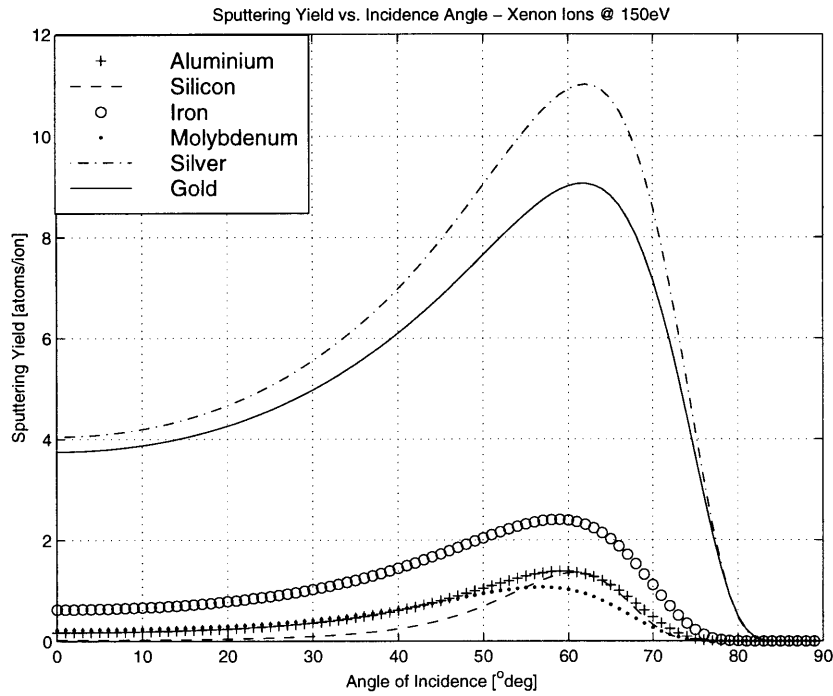
Figure B.1: Sputtering Yield vs. Angle of Incidence at 150eV
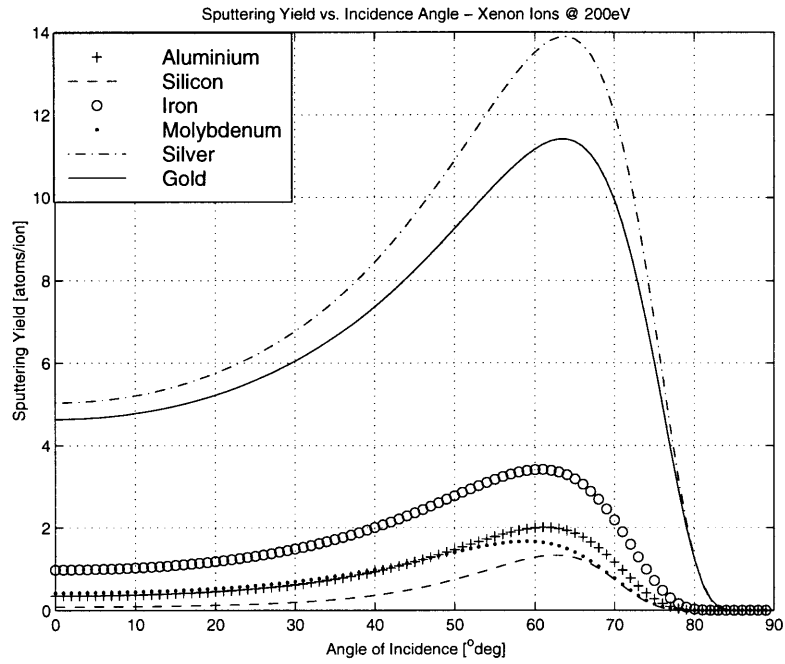
Figure B.2: Sputtering Yield vs. Incident Angle at 200eV
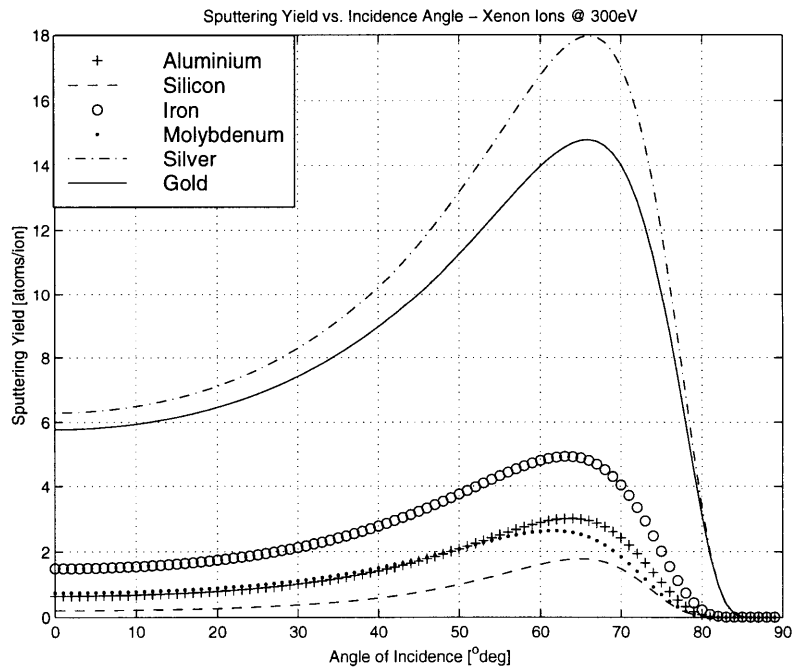
Figure B.3: Sputtering Yield vs. Incident Angle at 300eV
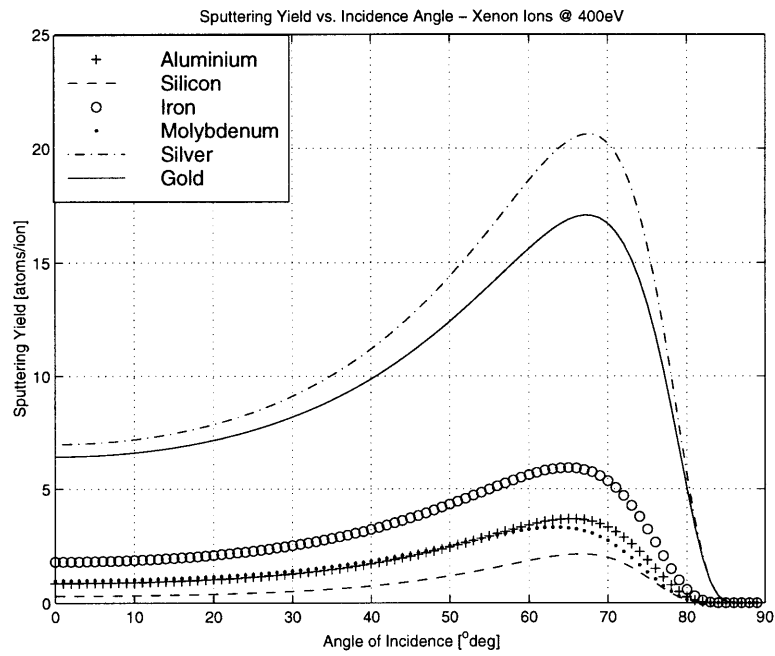
Figure B.4: Sputtering Yield vs. Incident Angle at 400eV
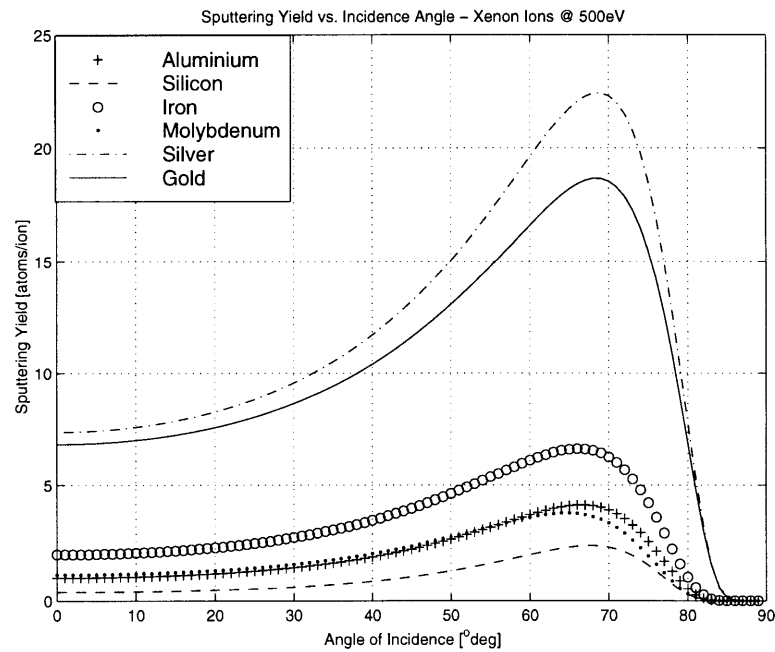
Figure B.5: Sputtering Yield vs. Incident Angle at 500eV
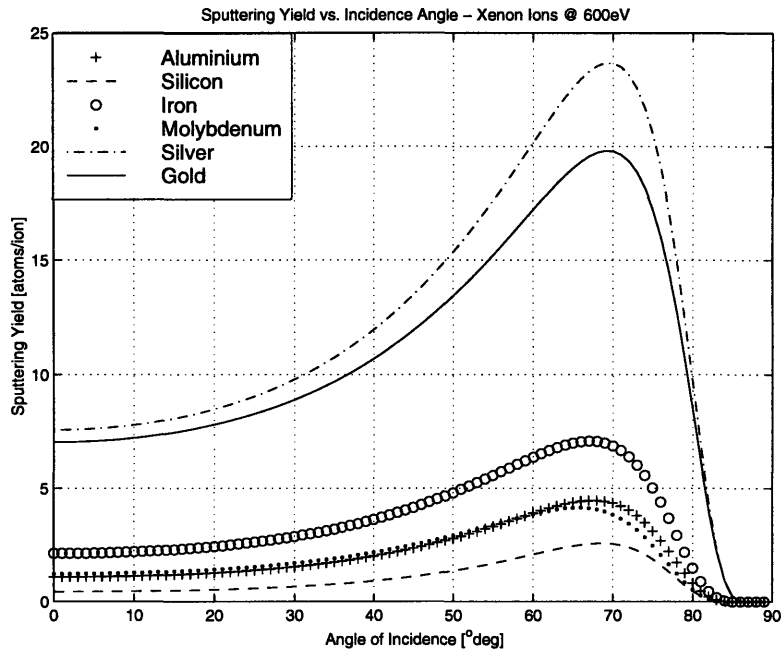
Figure B.6: Sputtering Yield vs. Incident Angle at 600eV
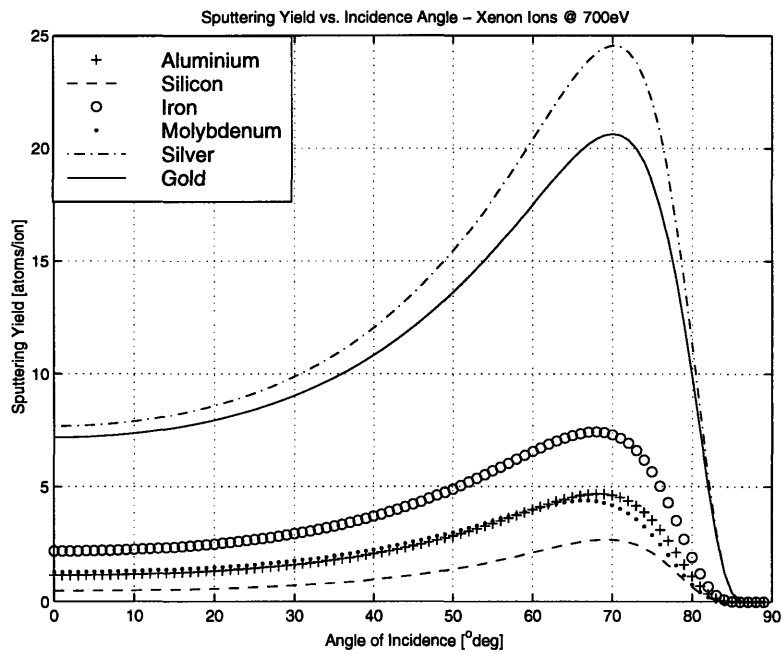
Figure B.7: Sputtering Yield vs. Incident Angle at 700eV

116
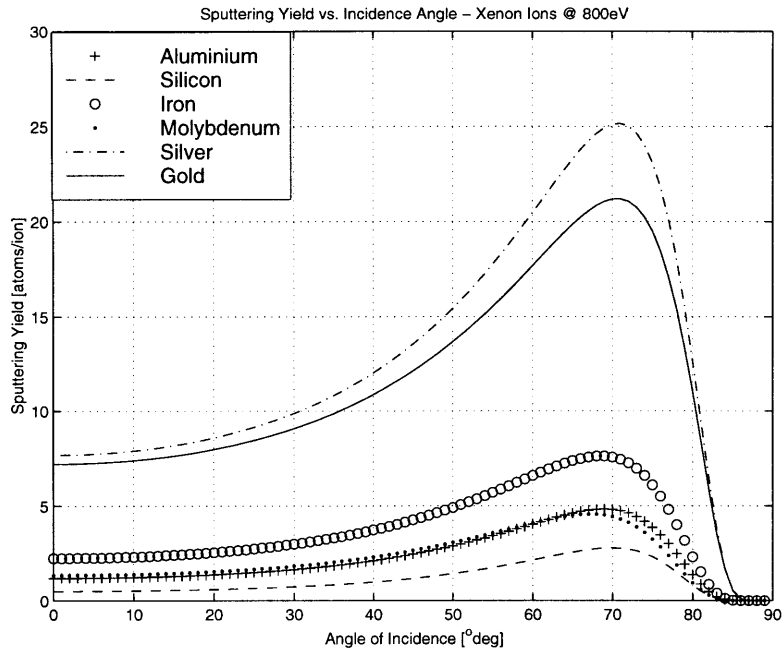
Figure B.8: Sputtering Yield vs. Incident Angle at 800eV
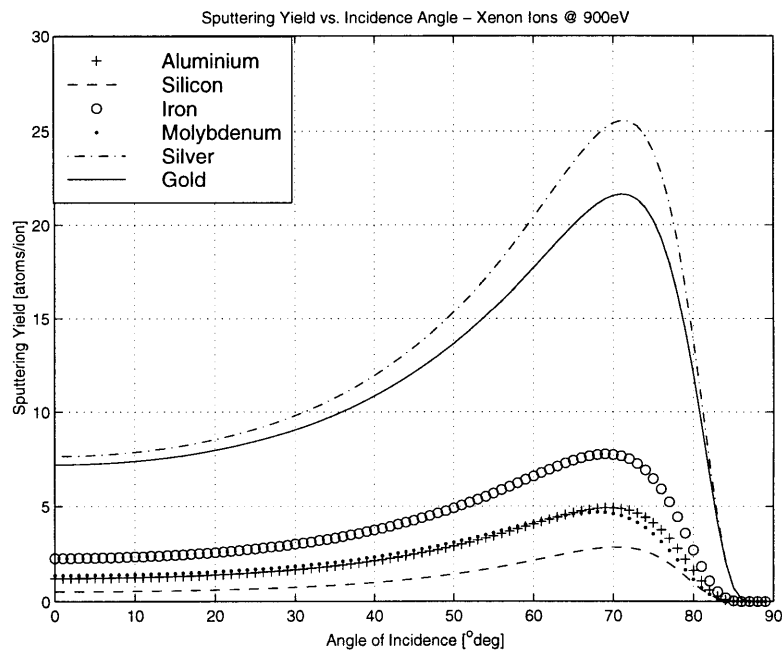
Figure B.9: Sputtering Yield vs. Incident Angle at 900eV
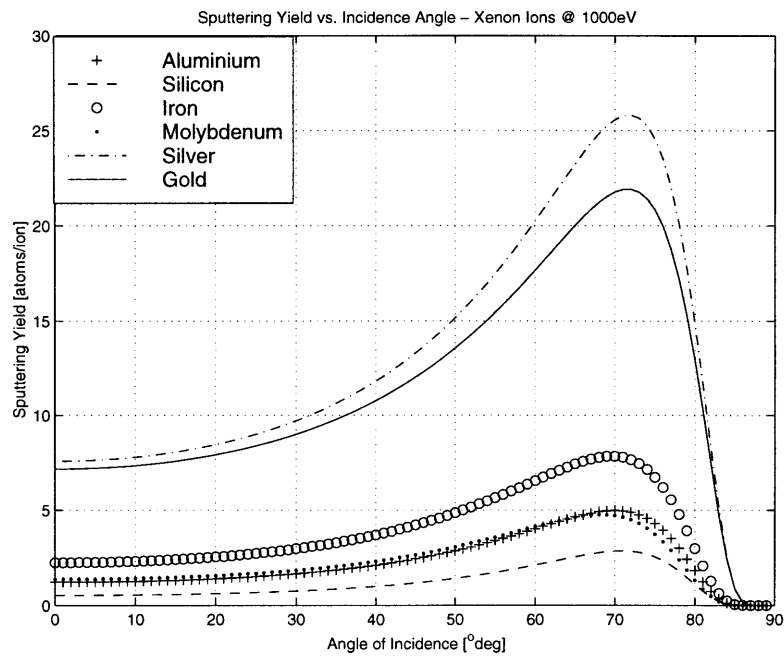
Figure B.10: Sputtering Yield vs. Angle of Incidence at 1000eV

Appendix C

Sample Weighting Input File

```
/* --------------------------------------------------------------------------------*/
/* For xe_ion_wt: the key here is to chose on average 10 macro particles          */
/* per cell in regions of interest                                                 */
/* For xe_ion_wt: in general, if xe_ion_wt is set correctly and                    */
/* anode_double_ion_fraction_fraction is equal to XX then, xe_2_ion_wt             */
/* should be XX times xe_ion_wt                                                    */
/* For xe_neutral_wt: the key here is to chose on average 10 macro                 */
/* particles per cell in regions of interest                                       */
/* --------------------------------------------------------------------------------*/
/* ---------------------------SAMPLE CALCULATION------------------------------------*/
/* Total Number of Cells = 25 * 35 * 25 = 21,875                                   *//
/* Number of macro-particles per cell = 10                                         */
/* Total number of macroparticles = 21,875 * 10 = 218,750                          */
/* Using above figures number of Xe ions = 218,750 * 1.25e11 = 2.73e14            */
/* Using above figures number of Xe_2 ions = 218,750 * 1.69e9 = 3.69e14           */
/* Using above figures number of Xe neutrals = 218,750 * 8e10 = 1.75e16           */
/* ----------------------------------------------------------------------------- */


bkg_neutral_density: 7.085e16              /* molecules/meter cubed */
anode_prop_ingestion_fraction: 0.2         /* ambient neutrals ingested */
anode_double_ion_fraction: 0.135           /* fraction leaving as double ions */
                                           /* aiaa-99-2423 ave. of king & gallimore*/


xe_ion_wt: 3.67e10                         /* real particles/macro particle */
xe_2_ion_wt: 4.050e9                       /* real particles/macro particle */
xe_neutral_wt: 8.0e11                      /* real particles/macro particle */
```

Appendix D

Sample Input Geometry File

```
/* domain.c */
/* This file is where the simulation's geometry is specified          */
/* The grid resolution used to resolve an object depends on how it sits */
/* in the domain.  An object has the resolution of the finest grid     */
/* in which it is ENTIRELY contained.                                  */
/* Objects must be at least two cells wide on some grid that contains them */
/* or the object will never be resolved enough to show on the grid     */
/* Define the objects in the routine defineObjects (below)             */
/* Placing an interior edge within one grid cell of an exterior boundary, */
/* or within one grid cell of another interior boundary, is definately */
/* a bad idea                                                          */
/* Domain_width_in_cells X Cell_Width X ref_length = Real_Life_Dimension */
/* eg. 25 cells X 10 units_per_cell * 0.010513 = 2.63 meters           */
/* This configuration is a generic vacuum tank                         */
/* The thruster has guards around its exit which are about 0.315 - 0.4 m deep */
/* The back of the tank is open as surfplot cannot accomodate more than 10 */
/* objects at the moment...might need to refine that for future simulations.. */


/* Domain dimension are:                 */
/* x_max = 2.63 m                        */
/* y_max = 3.68 m                        */
/* z_max = 2.63 m                        */

/* Dimensions of vacuum tank:            */
/* x_dimension = 2.42 m                  */
/* y_dimension = 3.47 m                  */
/* z_dimension = 2.42 m                  */

/* Dimensions of pumping orifice         */
/* y_dimension = 1.89 m                  */
/* z_dimension = 0.74 m                  */

#include <stdio.h>
#include <math.h>
#include "constants.h"
#include "mesh3.h"
#include "globals.h"

/* Domain Definition */
#define DOMAIN_X_WIDTH 25                /* Cells in X direction */
#define DOMAIN_Y_WIDTH 35                /* Cells in Y direction */
#define DOMAIN_Z_WIDTH 25                /* Cells in Z direction */

#define CELL_WIDTH 10.0                  /* Normalized units */

/* Needed to calculate thruster flow rate */
#define XE_ION_MASS (0.1313/AVOGADRO)

void defineBoundaries()
/* Sets the exterior boundary conditions (along edges of the domain) */
{
```

```
    particle_bnd_switch[NORTH] = ABSORBING;
    particle_bnd_switch[SOUTH] = ABSORBING;
    particle_bnd_switch[EAST] = ABSORBING;
    particle_bnd_switch[WEST] = ABSORBING;
    particle_bnd_switch[UP] = ABSORBING;
    particle_bnd_switch[DOWN] = ABSORBING;

    neutral_flux_switch[NORTH] = TRUE;
    neutral_flux_switch[SOUTH] = TRUE;
    neutral_flux_switch[EAST] = TRUE;
    neutral_flux_switch[WEST] = TRUE;
    neutral_flux_switch[UP] = TRUE;
    neutral_flux_switch[DOWN] = TRUE;

    ion_flux_switch[NORTH] = FALSE;
    ion_flux_switch[SOUTH] = FALSE;
    ion_flux_switch[EAST] = FALSE;
    ion_flux_switch[WEST] = FALSE;
    ion_flux_switch[UP] = FALSE;
    ion_flux_switch[DOWN] = FALSE;
}

/* When defining the embedded grid remember:                  */
/* 1. the width/offset is in grid points of parent grid       */
/* 2. there are two embeddedgrid cells per unit parent cell   */

void defineEmbeddedGrids()
{
    nembeddedgrid = 0;                                /* nembeddedgrid is a global variable */
    embeddedgrid = (embeddeddata *) calloc (nembeddedgrid, sizeof(embeddeddata));

    /* Piece 1: a box - child grid around thruster exit area */
    if (nembeddedgrid > 0) {
      embeddedgrid[0].xc = 11;                        /* Width in grid points on parent mesh */
      embeddedgrid[0].yc = 11;
      embeddedgrid[0].zc = 11;
      embeddedgrid[0].xoffc = 4;                      /* Offset in grid points on parent mesh */
      embeddedgrid[0].yoffc = 9;
      embeddedgrid[0].zoffc = 7;
      embeddedgrid[0].parent = -1;                    /* -1 indicates the top mesh is the parent */
    }
}

void defineObjects()
{
    nobjects = 10;                                    /* nobjects is a global variable, type short int */
    objects = (box *) calloc (nobjects, sizeof(box));

    /* Piece 1: Thruster Mount */
      objects[0].index = 0;                           /* Grid in which coord are given */
      objects[0].xc = 1;                              /* X-width, coord. */
    objects[0].yc = 11;                               /* Y-width, coord. */
    objects[0].zc = 11;
    objects[0].xoffc = 4;
    objects[0].yoffc = 12;
    objects[0].zoffc = 7;
    objects[0].type = FLOATING;                       /* Object surface boundary type */
    sprintf(objects[0].name, "Thruster_Mount");       /* NO SPACES ALLOWED in name */
```

```c
if (nobjects > 1) {
  /* Piece 2: Top Wall */
  objects[1].index = 0;
  objects[1].xc = 23;
  objects[1].yc = 33;
  objects[1].zc = 1;
  objects[1].xoffc = 1;
  objects[1].yoffc = 1;
  objects[1].zoffc = 22;
  objects[1].type = FLOATING;
  sprintf(objects[1].name, "Top_Wall");

}

if (nobjects > 2) {
  /* Piece 4: Target Wall */
  objects[2].index = 0;
  objects[2].xc = 1;
  objects[2].yc = 34;
  objects[2].zc = 23;
  objects[2].xoffc = 23;
  objects[2].yoffc = 0;
  objects[2].zoffc = 1;
  objects[2].type = FLOATING;
  sprintf(objects[2].name, "Target_Wall");
}

if (nobjects > 3) {
  /* Piece 4: Left Side Wall*/
  objects[3].index = 0;
  objects[3].xc = 23;
  objects[3].yc = 1;
  objects[3].zc = 23;
  objects[3].xoffc = 1;
  objects[3].yoffc = 33;
  objects[3].zoffc = 0;
  objects[3].type = FLOATING;
  sprintf(objects[3].name, "Left_Side_Wall");
}

if (nobjects > 4) {
  /* Piece 4: Right Side Wall */
  objects[4].index = 0;
  objects[4].xc = 23;
  objects[4].yc = 1;
  objects[4].zc = 23;
  objects[4].xoffc = 1;
  objects[4].yoffc = 0;
  objects[4].zoffc = 0;
  objects[4].type = FLOATING;
  sprintf(objects[4].name, " Right_Side_Wall");
}

if (nobjects > 5) {
  /* Piece 4: Bottom Wall */
  objects[5].index = 0;          /* Grid in which coord are given */
               /* This grid must surround the object ENTIRELY */
  objects[5].xc = 23;                    /* X-width, coord. */
  objects[5].yc = 33;                    /* Y-width, coord. */
```

```
        objects[5].zc = 1;
        objects[5].xoffc = 1;
        objects[5].yoffc = 1;
        objects[5].zoffc = 0;
        objects[5].type = FLOATING;
        sprintf(objects[5].name, " Bottom_Wall");


    }

if (nobjects > 6) {
  /* Piece 1: Bottom Backplate */
  objects[6].index = 0;
  objects[6].xc = 1;
  objects[6].yc = 33;
  objects[6].zc = 5;
  objects[6].xoffc = 1;
  objects[6].yoffc = 1;
  objects[6].zoffc = 1;
  objects[6].type = FLOATING;
  sprintf(objects[6].name, "Bottom_Backplate");


}

  if (nobjects > 7) {
  /* Piece 1: Top Backplate */
  objects[7].index = 0;
  objects[7].xc = 1;
  objects[7].yc = 33;
  objects[7].zc = 5;
  objects[7].xoffc = 1;
  objects[7].yoffc = 1;
  objects[7].zoffc = 17;
  objects[7].type = FLOATING;
  sprintf(objects[7].name, "Top_Backplate");

                                                        }


  if (nobjects > 8) {
  /* Piece 1: Left Backplate */
  objects[8].index = 0;
  objects[8].xc = 1;
  objects[8].yc = 11;
  objects[8].zc = 23;
  objects[8].xoffc = 1;
  objects[8].yoffc = 23;
  objects[8].zoffc = 0;
  objects[8].type = FLOATING;
  sprintf(objects[8].name, "Left_Backplate");

                                                        }


  if (nobjects > 9) {
  /* Piece 1: Right Backplate */
  objects[9].index = 0;
  objects[9].xc = 1;
  objects[9].yc = 11;
  objects[9].zc = 23;
  objects[9].xoffc = 1;
  objects[9].yoffc = 1;
```

```c
objects[9].zoffc = 0;
objects[9].type = FLOATING;
sprintf(objects[9].name, "Right_Backplate");


                                                    }

}


void defineSources()

    /* Modified for 3-D                                                    */
    /* The source location is given by its center.  So, if you place the source   */
    /* on a flat edge, and then turn it to any non-zero gimble angle, you'll get   */
    /* particles showing up INSIDE the object it's attached to (which is    */
    /* obviously a bad thing).  So, be cautious in how you use these sources    */
    /* at least for the near future                                        */
    /* 27th May 1999, -ba                                                          */
    /*BA - LINES BELOW - make sure you define the coords. of thruster with         */
    /* respect to the embedded grid defined above e.g. if the embedded grid is     */
    /* 10 by 10 by 10 parent grid cells then there are in fact 20 by 20 by 20      */
    /* embedded grid cells. if each parent cell has a normalized length of 10      */
    /* then each embedded grid cell will be 5 normalized unit cells wide.          */
    /* thus if u want to place thruster in the middle of the embedded grid then    */
    /* its coords. should be [(10parentcell*2embeddedcellsperparentcell*5normalizedunits/2]  */
    /* or more precisely [50,50,50]                                                */
{
  nsources = 1;
  sources = (sourcedata *) calloc (nsources, sizeof(sourcedata));


  if (nsources > 0) {
    /* Piece 1: a hall thruster */
    sources[0].nobj = 0;                        /* Object it's attached to */
    sources[0].xc = 11.500;                     /* Coordinates on object (normalized units */
    sources[0].yc = 55.000;
    sources[0].zc = 55.000;


    /* Vector pointing along the thruster exit direction                   */
    /* Quasi3 uses the thrust vector to determine the flow direction       */
    /* This vector can have an arbitrary magnitude                         */

    sources[0].thrustx = 1.0;
    sources[0].thrusty = 0.0;
    sources[0].thrustz = 0.0;


    /* Vector perpendicular to thrust vector pointing from center to cathode   */
    /* Quasi3 uses this vector to place cathode with respect to anode          */
    /* The vector can be of arbitrary magnitude but should be perpendicular    */
    /* to the thrust vector, or unpredictable things may happen                */

    sources[0].cathodex =  0.0;
    sources[0].cathodey =  0.0;
    sources[0].cathodez = -1.0;


    /* Total propellant flow rate in #_of_molecules/sec (sum of both cathode and anode)   */
    sources[0].flow_rate = (5.37e-6/XE_ION_MASS);
  }
}
void initializeVariables()
    /* Sets globals to values specified in define statements at the top of  */
    /* domain.c                                                             */
```

```
{
  domain_x_width = DOMAIN_X_WIDTH;
  domain_y_width = DOMAIN_Y_WIDTH;
  domain_z_width = DOMAIN_Z_WIDTH;
  cell_width = CELL_WIDTH;
}
```

Appendix E

Sputtering Yield Calculation - M-File

This is an m-file which was used to derive the sputtering yield based on Matsunami's and Yamamura's Theories outlined in Chapter 3.

```
E           = [115:50:1000]; %incident energy in eV
angle       = [0];

%% Xenon Properties
/***************/
m_xe        = 131.29;
z_xe        = 54;

%% Atomic Number of target elements
/**************************/
z_al        = 13;
z_si        = 14;
z_fe        = 26;
z_mo        = 42;
z_ag        = 47;
z_au        = 79;

%% Mass of target elements in amu
/************************/
m_al        = 26.982;
m_si        = 28.086;
m_fe        = 55.845;
m_mo        = 95.94;
m_ag        = 107.868;
m_au        = 196.967;

%% Sigmund's f factor for target elements
/****************************/
f_s_al      = 1.8;
f_s_si      = 1.8;
f_s_fe      = 1.84;
f_s_mo      = 1.85;
f_s_ag      = 1.84;
f_s_au      = 1.73;

%% Sublimation Energies as obtained by Yamamura
/***********************************/
Us_al       = 3.39;
Us_si       = 4.63;
Us_fe       = 4.28;
Us_mo       = 6.82;
Us_ag       = 2.95;
Us_au       = 3.81;

%% Threshold Energies as obtained by Yamamura
/**********************************/
Eth_al      = 69.2;
Eth_si      = 95.24;
```

```
Eth_fe        = 46.57;
Eth_mo        = 63.45;
Eth_ag        = 19.57;
Eth_au        = 17.74;

zeta_al       = 1 - sqrt(Eth_al./E);
zeta_si       = 1 - sqrt(Eth_si./E);
zeta_fe       = 1 - sqrt(Eth_fe./E);
zeta_mo       = 1 - sqrt(Eth_mo./E);
zeta_ag       = 1 - sqrt(Eth_ag./E);
zeta_au       = 1 - sqrt(Eth_au./E);

%% Q(z) Parameter
/**************/
Q_Z_al        = 1.1;
Q_Z_si        = 0.75;
Q_Z_fe        = 1.12;
Q_Z_mo        = 0.91;
Q_Z_ag        = 1.13;
Q_Z_au        = 0.98;

R_o_al        = 2.56;
R_o_si        = 2.72;
R_o_fe        = 2.28;
R_o_mo        = 2.01;
R_o_ag        = 2.58;
R_o_au        = 2.57;

gama_al       = 4*m_xe*m_al / (m_xe+m_al)^2;
gama_si       = 4*m_xe*m_si / (m_xe+m_si)^2;
gama_fe       = 4*m_xe*m_fe / (m_xe+m_fe)^2;
gama_mo       = 4*m_xe*m_mo / (m_xe+m_mo)^2;
gama_ag       = 4*m_xe*m_ag / (m_xe+m_ag)^2;
gama_au       = 4*m_xe*m_au / (m_xe+m_au)^2;

%% Screening Radius is calculated
/***********************/
a_al          = 0.4685/sqrt((z_xe^2/3+z_al^2/3));
a_si          = 0.4685/sqrt((z_xe^2/3+z_si^2/3));
a_fe          = 0.4685/sqrt((z_xe^2/3+z_fe^2/3));
a_mo          = 0.4685/sqrt((z_xe^2/3+z_mo^2/3));
a_ag          = 0.4685/sqrt((z_xe^2/3+z_ag^2/3));
a_au          = 0.4685/sqrt((z_xe^2/3+z_au^2/3));

E_L_al        = 563.5;
E_L_si        = 591.3;
E_L_fe        = 694.5;
E_L_mo        = 847.9;
E_L_ag        = 904.3;
E_L_au        = 1250;

N_al          = (1/R_o_al)^3;
N_si          = (1/R_o_si)^3;
N_fe          = (1/R_o_fe)^3;
N_mo          = (1/R_o_mo)^3;
N_ag          = (1/R_o_ag)^3;
N_au          = (1/R_o_au)^3;

R_L_al        = 1/pi/N_al/gama_al/(a_al)^2;
```

```
R_L_si          = 1/pi/N_si/gama_si/(a_si)^2;
R_L_fe          = 1/pi/N_fe/gama_fe/(a_fe)^2;
R_L_mo          = 1/pi/N_mo/gama_mo/(a_mo)^2;
R_L_ag          = 1/pi/N_ag/gama_ag/(a_ag)^2;
R_L_au          = 1/pi/N_au/gama_au/(a_au)^2;


k_al            = .11;
k_si            = .112;
k_fe            = .125;
k_mo            = .146;
k_ag            = .153;
k_au            = .207;


eps_al          = E/E_L_al;
eps_si          = E/E_L_si;
eps_fe          = E/E_L_fe;
eps_mo          = E/E_L_mo;
eps_ag          = E/E_L_ag;
eps_au          = E/E_L_au;


s_e_eps_al      = k_al * sqrt(eps_al);
s_e_eps_si      = k_si * sqrt(eps_si);
s_e_eps_fe      = k_fe * sqrt(eps_fe);
s_e_eps_mo      = k_mo * sqrt(eps_mo);
s_e_eps_ag      = k_ag * sqrt(eps_ag);
s_e_eps_au      = k_au * sqrt(eps_au);


psi_al          = ((a_al/R_o_al)^(3/2))*sqrt(z_xe*z_al./E./sqrt(z_xe^2/3+z_al^2/3));
psi_si          = ((a_si/R_o_si)^(3/2))*sqrt(z_xe*z_si./E./sqrt(z_xe^2/3+z_si^2/3));
psi_fe          = ((a_fe/R_o_fe)^(3/2))*sqrt(z_xe*z_fe./E./sqrt(z_xe^2/3+z_fe^2/3));
psi_mo          = ((a_mo/R_o_mo)^(3/2))*sqrt(z_xe*z_mo./E./sqrt(z_xe^2/3+z_mo^2/3));
psi_ag          = ((a_ag/R_o_ag)^(3/2))*sqrt(z_xe*z_ag./E./sqrt(z_xe^2/3+z_ag^2/3));
psi_au          = ((a_au/R_o_au)^(3/2))*sqrt(z_xe*z_au./E./sqrt(z_xe^2/3+z_au^2/3));


theta_opt_al    = 90 - 286*psi_al.^0.45;
theta_opt_si    = 90 - 286*psi_si.^0.45;
theta_opt_fe    = 90 - 286*psi_fe.^0.45;
theta_opt_mo    = 90 - 286*psi_mo.^0.45;
theta_opt_ag    = 90 - 286*psi_ag.^0.45;
theta_opt_au    = 90 - 286*psi_au.^0.45;

f_al            = f_s_al*(1 + 2.5*(1-zeta_al)/zeta_al);
f_si            = f_s_si*(1 + 2.5*(1-zeta_si)/zeta_si);
f_fe            = f_s_fe*(1 + 2.5*(1-zeta_fe)/zeta_fe);
f_mo            = f_s_mo*(1 + 2.5*(1-zeta_mo)/zeta_mo);
f_ag            = f_s_ag*(1 + 2.5*(1-zeta_ag)/zeta_ag);
f_au            = f_s_au*(1 + 2.5*(1-zeta_au)/zeta_au);

alpha_al        = 0.08 + 0.164*(m_al/m_xe).^0.45 + 0.0145*(m_al/m_xe).^1.29;
alpha_si        = 0.08 + 0.164*(m_si/m_xe).^0.45 + 0.0145*(m_si/m_xe).^1.29;
alpha_fe        = 0.08 + 0.164*(m_fe/m_xe).^0.45 + 0.0145*(m_fe/m_xe).^1.29;
alpha_mo        = 0.08 + 0.164*(m_mo/m_xe).^0.45 + 0.0145*(m_mo/m_xe).^1.29;
alpha_ag        = 0.08 + 0.164*(m_ag/m_xe).^0.45 + 0.0145*(m_ag/m_xe).^1.29;
alpha_au        = 0.08 + 0.164*(m_au/m_xe).^0.45 + 0.0145*(m_au/m_xe).^1.29;

Sigma_al        = f_al * cos(theta_opt_al * pi/180);
Sigma_si        = f_si * cos(theta_opt_si * pi/180);
```

```
Sigma_fe      = f_fe * cos(theta_opt_fe * pi/180);
Sigma_mo      = f_mo * cos(theta_opt_mo * pi/180);
Sigma_ag      = f_ag * cos(theta_opt_ag * pi/180);
Sigma_au      = f_au * cos(theta_opt_au * pi/180);


P_al      = 25.54;
P_si      = 13.66;
P_fe      = 38.47;
P_mo      = 28.41;
P_ag      = 88.31;
P_au      = 81.26;


S_n_eps_al_num      = (3.441.*sqrt(eps_al).*log10(eps_al + 2.718));
S_n_eps_si_num      = (3.441.*sqrt(eps_si).*log10(eps_si + 2.718));
S_n_eps_fe_num      = (3.441.*sqrt(eps_fe).*log10(eps_fe + 2.718));
S_n_eps_mo_num      = (3.441.*sqrt(eps_mo).*log10(eps_mo + 2.718));
S_n_eps_ag_num      = (3.441.*sqrt(eps_ag).*log10(eps_ag + 2.718));
S_n_eps_au_num      = (3.441.*sqrt(eps_au).*log10(eps_au + 2.718));
S_n_eps_al_den      = (1 + 6.355.*sqrt(eps_al) + eps_al.*(-1.708 + 6.882.*sqrt(eps_al)));
S_n_eps_si_den      = (1 + 6.355.*sqrt(eps_si) + eps_si.*(-1.708 + 6.882.*sqrt(eps_si)));
S_n_eps_fe_den      = (1 + 6.355.*sqrt(eps_fe) + eps_fe.*(-1.708 + 6.882.*sqrt(eps_fe)));
S_n_eps_mo_den      = (1 + 6.355.*sqrt(eps_mo) + eps_mo.*(-1.708 + 6.882.*sqrt(eps_mo)));
S_n_eps_ag_den      = (1 + 6.355.*sqrt(eps_ag) + eps_ag.*(-1.708 + 6.882.*sqrt(eps_ag)));
S_n_eps_au_den      = (1 + 6.355.*sqrt(eps_au) + eps_au.*(-1.708 + 6.882.*sqrt(eps_au)));


S_n_eps_al      = S_n_eps_al_num / S_n_eps_al_den;
S_n_eps_si      = S_n_eps_si_num / S_n_eps_si_den;
S_n_eps_fe      = S_n_eps_fe_num / S_n_eps_fe_den;
S_n_eps_mo      = S_n_eps_mo_num / S_n_eps_mo_den;
S_n_eps_ag      = S_n_eps_ag_num / S_n_eps_ag_den;
S_n_eps_au      = S_n_eps_au_num / S_n_eps_au_den;


S_n_E_al_num      = (3.441.*sqrt(E).*log10(E + 2.718));
S_n_E_si_num      = (3.441.*sqrt(E).*log10(E + 2.718));
S_n_E_fe_num      = (3.441.*sqrt(E).*log10(E + 2.718));
S_n_E_mo_num      = (3.441.*sqrt(E).*log10(E + 2.718));
S_n_E_ag_num      = (3.441.*sqrt(E).*log10(E + 2.718));
S_n_E_au_num      = (3.441.*sqrt(E).*log10(E + 2.718));
S_n_E_al_den      = (1 + 6.355.*sqrt(E) + E.*(-1.708 + 6.882.*sqrt(E)));
S_n_E_si_den      = (1 + 6.355.*sqrt(E) + E.*(-1.708 + 6.882.*sqrt(E)));
S_n_E_fe_den      = (1 + 6.355.*sqrt(E) + E.*(-1.708 + 6.882.*sqrt(E)));
S_n_E_mo_den      = (1 + 6.355.*sqrt(E) + E.*(-1.708 + 6.882.*sqrt(E)));
S_n_E_ag_den      = (1 + 6.355.*sqrt(E) + E.*(-1.708 + 6.882.*sqrt(E)));
S_n_E_au_den      = (1 + 6.355.*sqrt(E) + E.*(-1.708 + 6.882.*sqrt(E)));


S_n_E_al      = S_n_E_al_num / S_n_E_al_den;
S_n_E_si      = S_n_E_si_num / S_n_E_si_den;
S_n_E_fe      = S_n_E_fe_num / S_n_E_fe_den;
S_n_E_mo      = S_n_E_mo_num / S_n_E_mo_den;
S_n_E_ag      = S_n_E_ag_num / S_n_E_ag_den;
S_n_E_au      = S_n_E_au_num / S_n_E_au_den;


%%Matsunami's 3rd formula for normal sputtering
/***************************************/
Yield_al_norm      = (P_al .* S_n_eps_al .* (1 - sqrt(Eth_al./E)).^2.8) ./ (1 + 0.35 .* Us_al .* s_e_eps_al);
Yield_si_norm      = (P_si .* S_n_eps_si .* (1 - sqrt(Eth_si./E)).^2.8) ./ (1 + 0.35 .* Us_si .* s_e_eps_si);
Yield_fe_norm      = (P_fe .* S_n_eps_fe .* (1 - sqrt(Eth_fe./E)).^2.8) ./ (1 + 0.35 .* Us_fe .* s_e_eps_fe);
Yield_mo_norm      = (P_mo .* S_n_eps_mo .* (1 - sqrt(Eth_mo./E)).^2.8) ./ (1 + 0.35 .* Us_mo .* s_e_eps_mo);
```

Bibliography

[1] Abel, G., Ross, G., Terreault, B., Labrie, J. P.: Nucl. Instrum. Methods 170, 171 (1980).

[2] Absalamov, S. K., Andreev, V. B. et al. "Measurement of Plasma Parameters in the Stationary Plasma Thruster (SPT-100) plume and its Effects on Spacecraft Components." AIAA-92-3156, July 1992.

[3] Adesida, I., Karapiperis, L.: Radiat. Eff. 61, 223 (1982).

[4] Attaya, H., Kulcinski, G.L.: Report UWFDM-479, University of Wisconsin (1982).

[5] Banks, P., "Collision Frequencies and Energy Transfer Electrons." Planet. Space Sci., Vol. 14, 1966, pp. 1085-1101.

[6] Behrisch, R., "Sputtering by Particle Bombardment I: Introduction and Overview." *Topics in Applied Physics*, Vol 47, 1981.

[7] Behrisch, R., "Sputtering by Particle Bombardment I: Physical Sputtering of Single-Element Solids." *Topics in Applied Physics*, Vol 1, 1981

[8] Behrisch, R., "Sputtering by Particle Bombardment II: Sputtering of Alloys and Compunds, Electron and Neutron Sputtering, Surface Topography.." *Topics in Applied Physics,* Vol 52, 1983

[9] Biersack, J.P, Eckstein, W.: Appl. Phys. 34, 73 (1984).

[10] Biersack, J.P., Haggmark, L.G.: Nucl. Instrum. Methods 174, 257 (1980).

[11] Birdsall, C. K., and Langdon, A. B., "Plasma Physics Via Computer Simulation." Adam Hilger, Bristol, 1991.

[12] Birdsall, C. K., "Particle-in-Cell Charged Particle SImulations, Plus Monte-Carlo Collisions with Neutral Atoms, PIC-MCC." IEEE Transactions on Plasma Science, Vol. 19, No. 2, April 1991, pp. 65-85.

[13] Bishaev, A. M., and Kim, V., "Local Plasma Properties in a Hall-Current Accelerator with an Extended Acceleration Zone." *Soviet Physics Technical Physics,* 23(9) pp. 1055-1057, 1978.

[14] Bohdansky, J., and Roth, J., "An Analytical Formula and Important Parameters for Low-Energy ion Sputtering." J. Appl. Phys. 51(5), May 1980.

[15] Boyd, I. D., VanGilder, D. B., Liu, X., "Monte Carlo Simulation of Neutral Xenon Flows of Electric Propulsion Devices." IEPC-97-020, 1997.

[16] Chapman, B. "Glowing Discharge Processes: Sputtering and Plasma Etching." Wiley and Sons, New York, 1980.

[17] Chou, P.S., Ghoniem, N.M.: J. Nucl. Mater. 117, 55 (1983).

[18] Chou, P.S., Ghoniem, N.M.: J. Nucl. Mater. 141-143, 216 (1986).

[19] Cui, F.-Z., Li, H.-D.: Nucl. Instrum. Methods 7/8 650 (1985).

[20] Davisson, C.M.: Nucl. Instrum. Methods B15, 421 (1986).

[21] de Grys, K. H., Tilley, D. L., Aadland, R. S., "BPT Hall Thruster Plume Characteristics." AIAA-99-2283, 35th AIAA/ASME/SAE/ASEE Joint Propulsion Conference and Exhibit, Los Angeles, CA, 20-24th June, 1999.

[22] Desalvo, A. Rosa, R.: Radiat. Eff. Lett. 67, 119 (1982).

[23] Doughty, C., Gorbatkin, S. M., and Berry, L. A., "Spatial Distribution of Cu Sputter Ejected by Very Low Energy Ion Bombardment." J. Appl. Phys. 82 (4), 15th August, 1997.

[24] Duchemin, O.B., J.R. Brophy, C.E. Garner, P.K. Ray, V. Shutthanandan, and M.A. Mantenieks. "Review of Low Energy Sputtering Theory and Experiments.", IEPC 97-068, 25th International Electric Propulsion Conference, Cleveland, OH, August 24-28, 1997.

[25] Duchemin, O.B., Polk, J. E., "Low Energy Sputtering Experiments for Ion Engine Lifetime Assessment: Preliminary Results.", AIAA-99-2858, 35th AIAA/ASME/ SAE/ASEE Joint Propulsion Conference & Exhibit. Los ANgeles, CA, June 20-24th, 1998.

[26] Eckstein, W., "Computer Simulation of Ion-Solid Interactions." Springer-Verlag, Berlin, 1991.

[27] Fife, J. M., Martinez-Sanchez, M. "Characterization of the SPT-70 Plume Using Electrostatic Probes." AIAA-98-3795, 34th AIAA/ASME/SAE/ASEE Joint Propulsion Conference & Exhibit. Cleveland, OH, July 13-15, 1998.

[28] Fife, J. M., Martinez-Sanchez, M., Szabo, J., "A Numerical Study of Low-Frequency Discharge Oscillations in Hall Thrusters."

[29] Fife, J. M., personal communication, 1999.

144

[30] Fife, J.M. Two Dimensional Hybrid Particle-in-Cell Modeling of Hall Thrusters. Doctoral Thesis, Massachusetts Institute of Technology, Department of Aeronautics and Astronautics, 1998.

[31] Fustoss, L., Laszlo, J., Giber, J.: Vacuum 33, 121 (1983).

[32] Gavryushin, V.M., and Kim, V., "Effect of the Characteristics of Magnetic Field on the Parameters of an Ion Current at the Output of an Accelerator with Closed Electron Drift." Soviet Physics, 26(4):505-507,April 1981.

[33] Gilchrist, B. E., Ohler, S. G., and Gallimore, A. D., "Flexible Microwave System to Measure the Electron Number Density and Quantify the Communications Impact of Electric Thruster Plasma Plumes," Review of Scientific Instruments, Vol. 68, No. 2, Feb., 1997, 1189-1194.

[34] Gulczinski III, F. S., Gallimore, A. D., Carlson, D. O., Gilchrist, B. E., "Impact of Anode Layer Thruster Plumes on Satellite Communications." AIAA-97-3067, 33rd Joint Propulsion Conference, Seattle, WA, July 6-9, 1997.

[35] Haas, J. M., Gulczinski, F. S., Gallimore, A. D., Spanjers, G. G., Spores, R.A., "Performance Characteristics of a 5 kW Laboratory Hall Thruster." AIAA-98-3503", 34th Joint Propulsion, Cleveland, OH, July 12-15, 1998.

[36] Haas, J.M., et. al., "An Investigation of Electrostatic Probe Perturbations on the Operational Characteristics of a Hall Thruster and on the Measurement of Local Plasma Parameters," AIAA 98-3656, July 1998.

[37] Hassanein, A.M., Smith, D.L.: Nucl. Instrum. Methods B13, 225 (1986).

[38] Hautala, M.: Phys. Rev. B30, 5010 (1984).

[39] Hirakawa, M., and Arakawa, Y., AIAA Paper 96-3195, July 1996."Numerical Simulation of Plasma Particle Behavior in a Hall Thruster."

[40] Jackson, D. P.: J. Nucl. Mater. 93, 94, 507 (1980).

[41] Jackson, D.P., Heiland, W. Taglauer, E. :Phys. Rev. B24, 4198 (1981).

[42] Jackson, D.P.: Radiat. Eff. 49, 233 (1980).

[43] Jackson, J.P, Buck, T.M., Wheatley, G.H.: Nucl. Instrum. Methods B2, 440 (1984).

[44] Kannenberg, K. C., Boyd, I. D., and Dietrich, S., "Development of an Object-Oriented Parallel DSMC Code for Plume Impingement Studies." AIAA-95-2052, 30th AIAA Thermophysics Conference, June 19-22, 1995, San Diego, CA.

[45]   Kannenberg, K. C., Boyd, I. D., "Development of 3D Parallel DSMC Code for Plume Impingement Studies." AIAA-96-1848,31st AIAA Thermophysics Conference, June 17-20, 1995, New Orleans, LA.

[46]   Kaufman, H. R., "Technology of Closed-Drift Thrusters." Paper 83-1398, 19th AIAA/SAE/ASME Joint Propulsion Conference, Seattle, WA, June 27-29, 1983

[47]   Khyams, V., "Design of a Minitiarized Hall Thruster for Microsatellites." M.Sc. Thesis, Massachusetts Institute of Technology, Department of Aeronautics and Astronautics, May 1997.

[48]   Kim, S. W., Gallimore, A. D., "Plume Study of a 1.35 kW Spt-100 Using an ExB Probe." AIAA-99-2423, 35th Joint Propulsion Conference, Los Angeles, CA, June 1999.

[49]   King, L. B., "Transport-Property and Mass Spectral Measurements in the Plasma Exhaust Plume of a Hall-Effect Space Propulsion System," Ph.D. Thesis, University of Michigan, 1998.

[50]   King, L. B., and Galimore, A. D., "Ion Energy Diagnostics in the Plume of an SPT-100 from Thrust Axis to Backflow Region." AIAA-98-3641, 34th AIAA/ASME/SAE/ASEE Joint Propulsion Conference and Exhibit, Cleveland, OH, 13-15th July, 1998.

[51]   King, L. B., and Galimore, A. D., "Ionic and Neutral Particle Transport Property Measurements in the Plume of an SPT-100." AIAA-96-2712, July 1996.

[52]   King, L. B., and Galimore, A. D., "Propellant Ionization and Mass Spectral Measurements in the Plume of an SPT-100." AIAA-98-3657, 34th AIAA/ASME/SAE/ASEE Joint Propulsion Conference and Exhibit, Cleveland, OH, 13-15th July, 1998.

[53]   King, L. B., Gallimore, A. D., and Marrese, C. M., "Transport Property Measurements in the Plume of an SPT-100 Hall Thruster, "Journal of Propulsion and Power (AIAA), Vol. 14, No. 3, May-June 1998, 327- 335.

[54]   Lubachevsky, B. D., "How to simulate Billiards and Similar Systems." *Journal of Computational Physics*, Vol. 94 1991. pp. 255-283.

[55]   Manzella, D. H, "Stationary Plasma Thruster Plume Emissions." AIAA-93-097,23rd International Electric Propulsion Conference, Seattle, WA, September 13-16, 1993.

[56]   Manzella, D.H., "Stationary Plasma Thruster Ion Velocity Distribution." IEPC-94-3141, June 1994.

[57]   Marrese, C. M., Gallimore, A. D. et al., "An Investigation of Stationary Plasma Thruster Performance with Krypton Propellant."AIAA-95-2932, July 1995.

[58]   Melker, A. I., Romanov, S. N.: Fiz. Khim. Obrab. Mater 6, 12 (1979).

[59]   Mitchner, M., Kruger Jr., C. H., "Partially Ionized Gases." Wiley & Sons, 1992.

[60]   Miyagawa, Y., Miyagawa, S.: J. Appl. Phys. 54, 7124 (1983).

[61]   Moller, W. Eckstein, W., Biersack, J.P.: Comput. Phys. Commun. 51, 355 (1988).

[62]   Moller, W. Eckstein, W.: Nucl. Instrum. Methods B2, 814 (1984).

[63]   Oh, D. Y., Hastings, D. E., "Computational Modeling of Expanding Plasma Plumes in Space Using a PIC-DSMC Algorithm.", IEPC-97-179,

[64]   Oh, D. Y., "Computational Modeling of Expanding Plasma Plumes in Space Using a PIC-DSMC Algorithm." Sc.D. Thesis, Massachusetts Institute of Technology, Department of Aeronautics and Astronautics, February 1997.

[65]   Ohler, S., Gilchrist, B., and Gallimore, A. D., "Microwave Plume Measurements of an SPT-100 Using Xenon and a Laboratory Model SPT Using Krypton." AIAA-95-2931, July 1995,

[66]   Ohler, S., Shawn, G., Ruffin, A. B., Gilchrist, B. E., and Gallimore, A. D., "RF Signal Impact Study of an SPT." AIAA-96-2706, July 1996.

[67]   Pencil, E. J., Randolph, T., and Manzella, D., "End-of-Life Stationary Plasma Thruster Far Field Plume Characterization." AIAA-94-2855, 32nd AIAA/ASME/ SAE/ASEE Joing Propulsion Conference, 1996

[68]   Pencil, E. J., Randolph, T., and Manzella, D., "Far-Field Plume Contamination and Sputtering of the Stationary Plasma Thruster." AIAA-96-2709.

[69]   Pencil, E. J., "Far-Field Plume Contamination and Sputtering of the Stationary Plasma Thruster (SPT-100)." IEPC-93-098, September 1993.

[70]   Pollard, J. E., "Plume measurement with the T5 Xenon Ion Thruster." Aerospace Corporation report No. TR-94(4507) - 2, 1994.

[71]   Preuss, E.: Radiat. Eff. 38, 151 (1978).

[72]   Pugacheva, T.S.: Radiat. Eff. 102, 143 (1987).

[73] Qarnain, S. "Issues Regarding a Complete Computational Model of a Hall Thruster from the Acceleration Channel through the Plume." S.M. Thesis, Massachusetts Institute of Technology, Department of Aeronautics and Astronautics, May 1998.

[74] Qarnain, S., and Martinez-Sanchez, M. "Issues Regarding a Complete Computational Model of a Hall Thruster from the Acceleration Channel through the Plume." AIAA-98-3796, 34th AIAA/ASME/SAE/ASEE Joint Propulsion Conference and Exhibit, Cleveland, OH, July 13-15, 1998.

[75] Rhee, M. S., and Lewis, M. J., "Numerical Simulation of Stationary Plasma Thruster Exhaust Plume." AIAA-95-2928, July 1995

[76] Robinson, M. T., Torrens, I. M.: Phys. Rev. B9, 5008 (1974).

[77] Rosenberg, D., and Wehner, G. K., "Sputtering yields for Low Energy He+-, Kr+-, and Xe+- Ion Bombardment." J. Appl. Phys. vol. 33, No. 5, May 1962, pp. 1842-1845.

[78] Roush, M. L., Andreadis, T.D., Goktepe, O.F.: Radiat. Eff. 55, 119 (1981).

[79] Roussel, J. F., Bernard, J., and Garnier, Y., "Numerical Simulation of Induced Environment, Sputtering and Contamination of Satellite Due to Electric Propulsion." 2nd European Spacecraft Propulsion Conference, 27-29 May, (ESA SP-398, Aug. 1997).

[80] Ryssel, H., Glawisching, H., "Ion Implantation Techniques." *Springer Series in Electrophysics*, Vol. 10, 1982.

[81] Samanta Roy, R. I., Hasting, D. E., and Gatsonis, N. A., "A Review of Contamination from Electric propulsion Thrusters." AIAA-94-2469, June 1994.

[82] Samanta Roy, R. I., "Numerical Simulation of Ion Thruster Backflow for Spacecraft Contamination Assessment." Ph. D. Thesis, Massachusetts Institute of Technology, Department of Aeronautics and Astronautics, June 1995.

[83] Sankovic, J., Cavney, L., and Lynn, P., "The BMDO Russian Hall Thruster Technology (RHETT) Program: From Laboratory to Orbit." AIAA-97-2917, 33rd AIAA/ASME/SAE/ASEE Joint Propulsion Conference and Exhibit, Seattle, WA, 6-9th July, 1997.

[84] Shul'ga, V.I.: Radiat. Eff. 70, 65 (1983).

[85] Sigmund, P., "Theory of Sputtering, I. Sputtering Yield of Amorphous Solids and Polycrystalline Targets." Physics Review, 1842:383, 1969.

[86] Smulders, P.J.M., Boerma, D.O.: Nucl. Instrum. Methods B29, 471 (1987).

[87] Taglauer, E., Beitat, U., Marin, G., Heiland, W.: J. Nucl. Mater. 63, 193 (1976).

[88] Takeuchi, W., Yamamura, Y.: Radiat. Eff. 71, 53 (1983).

[89] Tatarkiewicz, J,. Nucl. Instrum. Methods 146, 447 (1977).

[90] Teplov, S.V., Chang, C.S., Kajarekar, P.P., Porter, T.L., Tsong, I.S.T.: Nucl. Instrum. Methods B35, 151 (1988).

[91] Thompson, D. A., Johar, S. S., "Influence of the Bombarding Angle on the Sputtering Yield of Heavy Atomic and Molecular Ion Bombardment of Ag and Au." Radiation Effects, 1981, Vol. 55. pp. 91-98.

[92] Tolk, N. H., Tully, J. C., Heiland, W., White, C. W., "Inelastic Ion-Surface Collisions."

[93] VanGilder, D. B., Font, G. I., Boyd, I. D., "Hybrid Monte Carlo - Particle-in-Cell Simulation of an Ion Thruster Plume." IEPC-97-182, 1997.

[94] VanGilder, D. B., Keidar, M.., Boyd, I. D., "Modeling Hall Thruster Plumes Using Particle Methods." AIAA-99-2294, 35th AIAA/ASME/SAE/ASEE Joint Propulsion Conference and Exhibit, Los Angeles, CA, 20-24th June, 1999.

[95] Vicanek, M., Urbassek, H.M.: nucl. Instrum. Methods B30, 507 (1988).

[96] Wang. J., Brophy, J., Brinza, D., "3-D Monte-Carlo Partcle-in-Cell Simulations of Ion Thruster Plasma Interaction." AIAA-95-2826, 1995.

[97] Wehner, G. K., and Rosenberg, D., J. Appl. Phys., 31, 177 (1960).

[98] Williams Jr., G. J., et al, "Laser Induced Fluorescence Measurement of Ion Velocities in the Plume of a Hall Effect Thruster." AIAA-99-2424, 35th AIAA/ASME/SAE/ASEE Joint Propulsion Conference and Exhibit, Los Angeles, CA, 20-23 June, 1999.

[99] Yamagiwa, Y., and Kuriki, K., "Performance of Double-Stage-Discharge Hall Ion Thruster," Journal of Propulsion, Vol. 7, No. 1, Jan-Feb 1991, pp. 65-70.

[100] Yamamura, Y., Itikawa, Y., and Itoh, N., "Angular Dependence fo Sputtering Yields of Monoatomic Solids." IPPJ-AM-26, Institute of Plasma Physics, Nagoya University, June 1983.

[101] Yamamura, Y., Matsunami, N., and Itoh, N., "Theoretical Studies on an Empirical Formula for Sputtering Yield at Normal Incidence." Radiation Effects, Vol. 71, pp. 65-86 (1983).

[102] Yamamura, Y., Takeuchi, W.: Nucl. Instrum. Methods B29 461 (1987).

[103] Yamamura, Y., "Contribution of Anisotropic Velocity Distribution of Recoil Atoms to Sputtering Yields and Angular Distributions of Sputtered Atoms." Radiation Effects, Vol. 55, pp. 49-56, 1981.

[104] Yamamura, Y.: Nucl. Instrum. Methods B33 493 (1988).

[105] Yamamura. Y., Takeuchi, W., "Computer Studies of The Energy Spectra and Reflection Coefficients of Light Ions." Radiation Effects, 1983, Vol. 71., pp. 53-64.

[106] Yamamura. Y., Takeuchi, W., "Monocrystal Sputtering by the Computer Simulation Code ACOCT." Nucl. Inst. and Meth. in Phys. B29 (1987) 461-470.

[107] Ziegler, J.F., Biersack, J.P., Littmark, U.: In *The Stopping and Range of Ions in Solids*, The Stopping and Range of Ions in Matter, Vol. 1, ed. by J.F. Ziegler (Pergamon, New York 1985).